

Spring 2022

Epitaxial 4H-SiC Radiation Detectors for Harsh Environment Applications

Joshua W. Kleppinger

Follow this and additional works at: <https://scholarcommons.sc.edu/etd>



Part of the [Electrical and Computer Engineering Commons](#)

Recommended Citation

Kleppinger, J. W.(2022). *Epitaxial 4H-SiC Radiation Detectors for Harsh Environment Applications*. (Doctoral dissertation). Retrieved from <https://scholarcommons.sc.edu/etd/6735>

This Open Access Dissertation is brought to you by Scholar Commons. It has been accepted for inclusion in Theses and Dissertations by an authorized administrator of Scholar Commons. For more information, please contact digres@mailbox.sc.edu.

EPI TAXIAL 4H-SiC RADIATION DETECTORS FOR HARSH ENVIRONMENT
APPLICATIONS

by

Joshua W. Kleppinger

Bachelor of Science in Engineering
University of South Carolina, 2017

Bachelor of Science
University of South Carolina, 2017

Submitted in Partial Fulfillment of the Requirements

For the Degree of Doctor of Philosophy in

Electrical Engineering

College of Engineering and Computing

University of South Carolina

2022

Accepted by:

Krishna C. Mandal, Major Professor

Roger Dougal, Committee Member

Grigory Simin, Committee Member

Fanglin (Frank) Chen, Committee Member

Tracey L. Weldon, Interim Vice Provost and Dean of the Graduate School

© Copyright by Joshua W. Kleppinger, 2022
All Rights Reserved.

DEDICATION

I would like to dedicate this work to my parents who have been nothing but supportive of me throughout my life. We may disagree on many things, but I will always love and respect you. I would also like to dedicate this work to my twin sister who has been my best friend and confidant for as long as I can remember.

ACKNOWLEDGEMENTS

First and foremost, I would like to express my utmost gratitude towards my advisor Dr. Krishna C. Mandal for his support and opportunities that have been granted to me over the course of my graduate studies. Under his tutelage, my knowledge in science and engineering and skills in research have expanded far beyond where I ever expected them to be five years ago. I would also like to show my appreciation towards my doctoral committee members—Drs. Roger Dougal, Grigory Simin, and Fanglin (Frank) Chen—for their valuable time and input for improving my dissertation research.

Over the last five years, I am delighted to have worked with my current and former colleagues Dr. Sandeep Chaudhuri, Dr. Cihan Oner, Dr. Towhid Chaudhuri, Dr. Mohsin Sajjad, Mr. OmerFaruk Karadavut, and Mr. Ritwik Nag. They have been unparalleled sources of knowledge, motivation, assistance, and friendship.

I would like to thank the National Science Foundation (NSF) Integrated Graduate Education and Research Traineeship (IGERT), DOE Nuclear Engineering University Program (NEUP), Grant no. No. DE-AC07-051D14517 & DE-NE0008662, Los Alamos National Lab/DOE (ISR), Grant No.# 143479, UofSC VP Research Office SPARC, Grant No. 15530- E422, and UofSC VP Research Office ASPIRE-I &II Grants for funding this research.

Within the University of South Carolina community, I would like to acknowledge Dr. Yuriy Pershin of Physics for serving as my co-advisor for NSF IGERT the first two years of my graduate studies and for granting me access to the VASP computational

resources. I would also like to thank on the behalf of our group Prof. Frank Avignone III of the Department of Physics for providing access to various X-ray sources; Dr. Forest Agostinelli and Prof. Amit Sheth of AI Institute for our on-going artificial intelligence/machine learning collaboration; and Profs. Frank (Fanglin) Chen, Kevin Huang, and Gongkyu Lee of Mechanical Engineering for depositing yttrium oxide on several of our silicon carbide epilayers for surface passivation. Additionally, I would like to thank the Electron Microscopy Center for providing access to their scanning electron microscopy and energy dispersive X-ray analysis equipment.

Outside the University of South Carolina community, I would like to thank Prof. Douglas McGregor and Daniel Watson of Kansas State University for their accelerator irradiation facilities; Lawrence Livermore National Laboratory for low-energy X- and γ -ray measurements; Brookhaven Nation Laboratory for their synchrotron light source, and Savannah River National Laboratory for nuclear waste characterization measurements using our silicon carbide detectors. Finally, I would like to thank NASA Glenn Research Center and NASA Marshall Space Flight Center for consulting with us on lunar and Venus missions.

ABSTRACT

Epitaxial 4H-silicon carbide (4H-SiC) is an essential semiconductor material for the development of harsh environment radiation detectors due to its excellent electrical and thermal properties and resistance to radiation damage, opening the door for a wide variety of applications in NASA space missions, nuclear safeguards, and nuclear energy. However, the low atomic numbers of its constituent atoms Si ($Z = 14$) and C ($Z = 6$) make 4H-SiC nearly transparent to most neutrally charged radiation which can only be compensated using thicker active volumes.

In this dissertation, Ni/n-4H-SiC Schottky barrier diode (SBD) radiation detectors are fabricated for the first time on 250 μm thick 4H-SiC epitaxial layers—the thickest epilayers used for radiation detection to date. The detectors were found to have low leakage current densities $<3 \text{ nA cm}^{-2}$ at -800 V and benchmark 5486 keV alpha particle energy resolutions of $<0.5\%$ full width half maximum (FWHM). Despite this, evaluation of the barrier lowering determined the leakage current was predominantly trap-assisted through the Poole-Frenkel effect and the detector energy resolution limited by trapping in the epilayer. In addition to increasing the detector leakage current, defects can trap radiation induced charge carriers in intraband states preventing them from being collected. In n-type 4H-SiC, the most significant trapping center is $Z_{1/2}$ which along with $\text{EH}_{6/7}$ corresponds to different charge states of the carbon vacancy which is theoretically predicted to appear in all as-grown epilayers based on ab initio calculations. Deep level transient spectroscopy

(DLTS) studies show that the energy resolution of 4H-SiC radiation detectors is correlated with the trapping rate of $Z_{1/2}$.

Further studies were conducted to characterize the effects of harsh environment conditions on the properties of the detectors. First, temperature variation of the leakage current at elevated temperature was studied by temperature-dependent current voltage (I-V-T) measurements on 150 μm epitaxial layers which revealed that traps such as $Z_{1/2}$ and $\text{EH}_{6/7}$ and low barrier patches in spatial geometry of the metal-semiconductor (M-S) interface can produce excess leakage current compared to thermionic emission-diffusion (TED) theory. Next, the effect of neutron irradiation up to fluences of 10^{13} cm^{-2} was studied using 250 μm epilayers. Detector energy resolution was shown to degrade with increasing fluences which was correlated with the formation of three new deep levels at 0.8, 1.2, and 1.8 eV below the conduction band. These levels were found to correspond to—based on density functional theory calculations with hybrid pseudopotentials—silicon displacement-related defects formed from the collision of fast neutrons ($> 1 \text{ MeV}$) with the silicon nucleus.

TABLE OF CONTENTS

Dedication	iii
Acknowledgements	iv
Abstract	iv
List of Tables	x
List of Figures	xi
List of Symbols	xvii
List of Abbreviations	xxii
Chapter 1: Introduction	1
1.1 4H-SiC Detectors for Harsh Environments	1
1.2 Importance of Detector Thickness	4
1.3 Dissertation Overview	7
Chapter 2: 4H-SiC Schottky Radiation Detectors Fabricated on 250 μm Epitaxial Layers	9
2.1 Physics of Schottky Barrier Diodes	9
2.2 Fabrication of Ni/n-4H-SiC SBDs	14
2.3 Electrical Characterization Measurements	17
2.4 Alpha Pulse Height Spectroscopy with ^{241}Am	24
2.5 Conclusion	30
Chapter 3: Correlation of Defects with Radiation Detection	31
3.1 Charge Trapping in Semiconductor Radiation Detectors	31

3.2 Point Defects in 4H-SiC.....	36
3.3 Minority Carrier Diffusion Length Measurements	44
3.4 Deep Level Transient Spectroscopy Background.....	52
3.5 DLTS on 4H-SiC Radiation Detectors	57
3.6 Conclusion	62
Chapter 4: Current Flow Analysis by I-V-T	63
4.1 Introduction.....	63
4.2 Device Characterization from C-V-T	64
4.3 Surface Barrier Evaluation from Forward Bias Measurements	66
4.4 Leakage Current Analysis from Reverse Bias Measurements.....	71
4.5 Conclusion	78
Chapter 5: Neutron Irradiated 4H-SiC Epitaxial Layers.....	80
5.1 Introduction.....	80
5.2 Irradiation Procedure	81
5.3 Detector Characterization	82
5.4 Alternative Defect Characterization Methods: CTS and PICTS	89
5.5 Deep Levels in Neutron Irradiated Epilayers.....	94
5.6 Conclusion	104
Chapter 6: Conclusion, Dissemination of Work, and Future Work.....	106
6.1 Final Conclusions.....	106
6.2 Dissemination of Work.....	109
6.3 Future Work	113
References.....	115

LIST OF TABLES

Table 1.1 Comparison of 4H-SiC properties with other materials at 300K.....	2
Table 2.1 Detector parameter obtained for detectors fabricated on 250 μm epilayers	28
Table 3.1 Vacancy transition levels computed with HSE06 pseudopotentials. The energy levels are measured from the valence band maximum and given in eV.	43
Table 3.2 Detector parameters obtained for detectors fabricated on 50, 150, and 250 μm epitaxial layers	48
Table 3.3 Comparison of defect parameters obtained from DLTS results on 50, 150, and 250 μm epilayers	60
Table 4.1 Defect parameters obtained from DLTS spectrum of the 150 μm detector.....	78
Table 5.1 Accumulated neutron dose of 250 μm 4H-SiC epitaxial layer samples.....	82
Table 5.2 Summary of electrical and radiation detection properties of detectors fabricated on neutron irradiated 4H-SiC epitaxial layers.	86
Table 5.3 Trap parameters obtained from the DLTS measurements of detector N1.....	96
Table 5.4 Trap parameters obtained from the DLTS measurements of detector N2.....	98
Table 5.5 Trap parameters obtained from the CTS measurements of detector N3.....	100
Table 5.6 Trap parameters obtained from the PICTS measurements of detector N4.....	102
Table 5.7 Transition levels of silicon displacement-related defects in 4H-SiC measured from the valence band maximum.	104

LIST OF FIGURES

Figure 1.1 Linear attenuation coefficients of 4H-SiC for high energy photons ranging from 1 keV to 1 MeV simulated using NIST's XCOM program.	5
Figure 1.2 Probability of photoelectric adsorption occurring within the detector as a function of the depletion width for ⁵⁵ Fe X-rays (5.19 keV) and ²⁴¹ Am (59.5 keV) gamma rays.	6
Figure 2.1 Energy band diagram for a Schottky junction between a metal and an n-type semiconductor (a) before contact and (b) at equilibrium.	10
Figure 2.2 Energy band diagram of Schottky contact under (a) forward bias and (b) reverse bias. The current transport mechanisms are (1) thermionic emission, (2) diffusion (drift under reverse bias), or (3) tunneling.	12
Figure 2.3 Schematic of the device structure of a Ni/n-4H-SiC radiation detector fabricated on 250 μm epitaxial layers.	16
Figure 2.4 Forward bias I-V characteristics for detectors S1, S2, and S3 fabricated on 250 μm 4H-SiC epitaxial layers. The solid lines represent the straight line fit of the linear region.	18
Figure 2.5 Reverse bias I-V characteristics for detectors S1, S2, and S3 fabricated on 250 μm 4H-SiC epitaxial layers.	19
Figure 2.6 Capacitance per unit area as a function of applied bias for the 250 μm Ni/n-4H-SiC epitaxial layer radiation detectors.	19
Figure 2.7 Mott-Schottky plots of the detectors S1, S2, and S3. The solid lines are straight-line fits for calculating the effective doping concentration at two different bias regimes.	21
Figure 2.8 Variation of current density under reverse bias as a function of mean electric field across the space charge region. The mean field can be converted to maximum field at the M-S interface by multiplying by 2.	22

Figure 2.9 Interfacial electric field dependence of the current density J normalized to the interfacial electric field E_m . Dashed lines are the linear fit of experimental data. S2 has a second linear fit in red corresponding to interfacial electric fields greater than 0.2 MV/cm.	23
Figure 2.10 Block diagram of the radiation detection system at UofSC (a), a photograph of the electronic box used for radiation detection (b), and a photograph of the radiation detection system (c), used in this work.	26
Figure 2.11 ^{241}Am Pulse height spectra obtained for S1 (a), S2 (b), and S3 (c). The solid red lines are the triple Gaussian model fitted overtop the PHS.	27
Figure 2.12 Pulser PHS obtained with and without detector S3 at -200 V and a shaping time of 1 μs	29
Figure 3.1 Demonstration of charge collection in both an ideal detector and a detector with trapping from defects.	32
Figure 3.2 Band diagram displaying how a captured electron with capture rate c_n can either recombine with a captured hole c_p or emit back to the conduction band.	34
Figure 3.3 Band diagram displaying the steady-state occupation of trap levels (a) and the emission of traps in the space-charge region of SBDs under reverse bias (b). n_T is the concentration of occupied defect levels.	35
Figure 3.4 Crystal structure of a generic zinc blende lattice illustrating the various types of point defects that can occur in semiconductor crystals.	37
Figure 3.5 Stacking structure of 4H-SiC showing the various lattice sites which defects can occupy.	38
Figure 3.6 Band structure of 4H-SiC calculated using HSE06 pseudopotentials. The x-axis is the k- or reciprocal space projection of periodic lattice structure. The labels refer to the high symmetry points of the first Brillouin zone of a simply hexagonal lattice [73].	40
Figure 3.7 Formation energies as a function of the fermi-level for carbon and silicon vacancies in 4H-SiC calculated using HSE06 pseudopotentials.	41

Figure 3.8 Forward bias current-voltage characteristics for the detectors fabricated on the 50, 150, and 250 μm epitaxial layers. The solid lines represent the fit to the linear region.	45
Figure 3.9 Reverse bias current-voltage characteristics for the detectors fabricated on the 50, 150, and 250 μm epitaxial layers.	46
Figure 3.10 Mott-Schottky plot of detectors fabricated on the 50, 150, and 250 μm epitaxial layers. The solid lines are the linear fits.	47
Figure 3.11 Pulse height spectra at the bias which gave the best resolution for the detectors fabricated on 50 (a), 150 (b), and 250(c) μm 4H-SiC epitaxial layers.	48
Figure 3.12 Illustration of the drift-diffusion model for charge collection.....	49
Figure 3.13 Charge collected as a function of the applied reverse bias given in channel number to clearly distinguish among the three curves. The dashed lines are the fit to the drift-diffusion model.	51
Figure 3.14 Bragg curve for 5486 keV alpha particles interacting with 4H-SiC.....	52
Figure 3.15 Band diagrams of a Schottky detector with a trap level E_T demonstrating trapping and de-trapping with periodic biasing.	53
Figure 3.16 Demonstration of the capacitance transient and the formation of the DLTS signal.	56
Figure 3.17 DLTS spectrum of a typical high quality as-grown 4H-SiC epitaxial layer.	58
Figure 3.18 Arrhenius plot of the spectrum shown in Figure 3.17.	59
Figure 3.19 DLTS spectra obtained using 0.5 ms initial delays and zoomed in on $Z_{1/2}$ (a) and the spectra obtained using 10 ms initial delays zoomed in on $E_{H_{6/7}}$ (b) for each of the detectors fabricated on 50, 150, and 250 μm epilayers.	61
Figure 4.1 Mott-Schottky plots extracted from the C-V-T characteristics for a Ni/n-4H-SiC Schottky barrier detector fabricated on 150 μm epitaxial layers recorded at temperatures between 300 and 600 K in steps of 50 K.	65

Figure 4.2 Net donor concentration and average barrier height acquired from the C-V-T results.....	66
Figure 4.3 Forward bias I-V characteristics for a Ni/n-4H-SiC SBD fabricated on 150 μm epitaxial layers from 300 to 600 K measured in steps of 50 K. The plot is divided by the arrow into two linear regions, the low voltage region (LVR) and high voltage region (HVR).	67
Figure 4.4 Arrhenius plot of the saturation current density I_0 normalized by $N_c v_{eff}$. The effective carrier velocity v_{eff} is defined as $v_R v_D / (v_R + v_D)$	69
Figure 4.5 Barrier height plotted against the corresponding ideality factor in the HVR. The high temperature region (≥ 500 K) is included as part of the HVR and the solid line is the linear fit used to acquire the average barrier height Φ_{B0}	70
Figure 4.6 Reverse bias I-V characteristics for the Ni/n-4H-SiC SBD fabricated on 150 μm epitaxial layers measured at temperatures ranging from 300 to 600 K in steps of 50 K.	72
Figure 4.7 Reverse bias leakage current as a function of the electric field at the metal-semiconductor interface for the I-V-T characterized 150 μm epitaxial layer detector. The solid lines are the linear fit to the data points.....	73
Figure 4.8 Arrhenius plots of the slopes of each I-V trace from 20 to 80 kV/cm. The solid line is the overall linear fit, whereas the dashed and dotted lines correspond to the fits over a reduced temperature range.....	74
Figure 4.9 Natural logarithm of the reverse bias leakage current normalized to the interfacial electric field plotted against the square root of the interfacial electric field for the I-V-T characterized 150 μm epilayer detector.....	75
Figure 4.10 DLTS spectra of the I-V-T characterized 150 μm epilayer detector using the initial delays 0.5, 1, 2, and 5 ms.	76
Figure 4.11 Arrhenius plot of the emission rates for the spectrum in Figure 4.10.....	77
Figure 5.1 The cadmium envelope (left) and the finished detector (right).	82
Figure 5.2 Forward and reverse bias I-V characteristics for detectors fabricated on neutron irradiated epilayers.....	83

Figure 5.3 Mott-Schottky plots for the detectors fabricated on neutron irradiated 4H-SiC epitaxial layers given in semi-log scale to show the difference in capacitance profiles between the lightly and heavily irradiated samples.	84
Figure 5.4 Optimal pulse height spectra obtained for the detectors (a) N1, (b) N2, (c) N3, and (d) N4, fabricated on neutron irradiated epilayers, when exposed to an ^{241}Am alpha particle source.	85
Figure 5.5 Detector resolution plotted against the applied reverse bias at the optimal shaping times on a log-log scale for better visibility.	87
Figure 5.6 Detector N1, N2, and N3 charge collected in channel number plotted against the applied reverse bias using optimal shaping times. The solid lines are the fit to the drift-diffusion model.	88
Figure 5.7 Charge collected in channel number plotted against the applied reverse bias for detector N4. The solid line is the fit to Eqn. 5.1. CN refers to the channel number.	89
Figure 5.8 Illustration of charge carrier trapping under illumination (a) and the emission of charge carriers once the light source is removed (b).	91
Figure 5.9 Photograph and diagram of the PICTS system designed and implemented at UofSC.	92
Figure 5.10 Typical function generator output (a) and preamplifier output (b) observed in the oscilloscope during the PICTS measurements.	93
Figure 5.11 DLTS spectrum of neutron irradiated detector N1 fabricated on epilayers irradiated at fluences $\sim 10^{10} \text{ cm}^{-2}$	95
Figure 5.12 Arrhenius plots for the DLTS spectrum of neutron irradiated detector N1 fabricated on epilayers irradiated at neutron fluences $\sim 10^{10} \text{ cm}^{-2}$	96
Figure 5.13 DLTS spectrum of neutron irradiated detector N2 fabricated on epilayers irradiated at fluences $\sim 10^{11} \text{ cm}^{-2}$	97
Figure 5.14 Arrhenius plots for the DLTS spectrum of neutron irradiated detector N2 fabricated on epilayers irradiated at neutron fluences $\sim 10^{11} \text{ cm}^{-2}$	98
Figure 5.15 CTS spectrum of neutron irradiated detector N3 fabricated on epilayers irradiated at fluences $\sim 10^{12} \text{ cm}^{-2}$	99

Figure 5.16 Arrhenius plots for the CTS spectra of neutron irradiated detector N3 fabricated on epilayers irradiated at neutron fluences $\sim 10^{12} \text{ cm}^{-2}$	99
Figure 5.17 PICTS spectrum of neutron irradiated detector N4 fabricated on epilayers irradiated at fluences $\sim 10^{13} \text{ cm}^{-2}$ using 0.3 and 9 ms initial delays.	101
Figure 5.18 Arrhenius plot for the PICTS spectrum of neutron irradiated detector N4 fabricated on epilayers irradiated at neutron fluences $\sim 10^{13} \text{ cm}^{-2}$	101
Figure 5.19 Formation energies of silicon displacement-related defects in 4H-SiC using HSE06 hybrid pseudopotentials in C-rich conditions.	103

LIST OF SYMBOLS

Z	Atomic number.
E_g	The semiconductor bandgap. The energy gap between the valence band maximum and conduction band minimum.
ϵ	Electron hole-pair creation energy. The ratio between the energy of the incident radioactive particle and number of charges collected.
κ	Thermal conductivity.
ρ	Density of the material.
μ_n	Semiconductor electron mobility.
μ_p	Semiconductor hole mobility
v_{sat}	Saturation drift velocity
E_{BD}	Breakdown electric field of the material.
α	Linear attenuation coefficient
Φ_m	Work function of the metal. The energy required for an electron in the metal to be fully ejected from the metal into a vacuum.
Φ_s	Work function of the semiconductor. Average energy required for an electron in the semiconductor to be ejected into a vacuum.
E_F	Fermi level. Refers to the energy level where the probability of occupation is 50% in Fermi-Dirac statistics. In semiconductors, this refers to a nonexistent energy level within the bandgap based on the concentration of occupied conduction band states and unoccupied valence band states.
E_{Fm}	The Fermi-level in the metal of an M-S junction.
ϕ_B	Schottky barrier height. Describes the energy barrier an electron in the metal must jump to pass into the semiconductor.

E_v	Valence band maximum. The top of valence band in the electronic band structure of a semiconductor.
E_c	Conduction band minimum. The bottom of conduction band in the electronic band structure of a semiconductor.
χ_s	Electron affinity of the semiconductor. The energy required to move an electron from the conduction band minimum to a vacuum.
ϕ	Position-dependent electrostatic potential within the space-charge region.
$p(x)$	The position dependent hole concentration in the space-charge region.
$n(x)$	The position dependent electron concentration in the space-charge region.
e	Elementary charge of an electron (1.601×10^{-19} C).
ε	Dielectric permittivity of the semiconductor (8.55×10^{-13} F/cm in 4H-SiC).
N_{eff}	Effective or net donor concentration.
V_{bi}	The built-in voltage or potential of a Schottky diode. Describes the energy gap between the conduction band minimum at the edge of the space-charge region and the top of the Schottky barrier at equilibrium.
k_B	Boltzmann's constant taken as 8.617×10^{-5} eV K ⁻¹ .
T	Absolute temperature measured in Kelvin.
x_d	The depletion width. The width of the space-charge or depletion region under the full depletion approximation of Poisson's equation.
E_x	Position-dependent electric field strength within the space-charge region.
E_m	Interfacial electric field. The electric field strength directly at the metal-semiconductor interface.
J	Leakage current density passing through the device.
A^*	Richardson coefficient for thermionic emission taken to be $146 \text{ A cm}^{-2} \text{ K}^{-2}$ in 4H-SiC.
V	The voltage bias applied to the device.
n	Diode ideality factor. Describes how ideal the Schottky barrier is with $n = 1$ being perfectly ideal.

N_c	Effective density of states of the conduction band.
C	Capacitance. The differential change in charge with respect to the applied bias.
A	Junction area. Taken to be the surface area of the top metal contact.
$\Delta\Phi$	Barrier lowering as a function of the interfacial electric field.
m	Barrier lowering parameter used for distinguishing between image force Schottky barrier lowering and Poole-Frenkel trap barrier lowering.
$N(t)$	Number of generated electrons in Shockley-Ramo's theorem.
v_d	Carrier drift velocity.
E_w	The weighting potential in Shockley-Ramo's theorem.
N_T	Trap concentration.
σ_n	Trap capture cross-section of electrons.
σ_p	Trap capture cross-section of holes.
$\langle v_{th,n} \rangle$	Mean thermal velocity of electrons.
$\langle v_{th,p} \rangle$	Mean thermal velocity of holes.
τ_n	Mean charge trapping time for electrons.
τ_p	Mean charge trapping time for holes.
N_0	The total number of generated electron-hole pairs
x_i	The interaction point of a photon in the active region
d	Thickness of the active region in a planar detector
t_r	Charge carrier transit time. How long it takes a charge carrier to travel from the interaction point to its respective electrode.
Q_n	Electron charge collected.
Q_p	Hole charge collected.
e_n	Emission rate of trapped electrons from a deep level.

c_n	Capture rate of electrons by a deep level.
c_p	Capture rate of holes by a deep level.
E_T	Trap energy level.
n_T	Concentration of occupied traps.
$E_{D,q}^f$	Formation energy of defect D at integer charge state q .
$E_{D,q}$	Energy of defective supercell D at charge state q calculated by density functional theory.
E_{ideal}	Energy of the ideal supercell calculated by density functional theory.
n_i	Number of atoms of species i added (+) or removed (-) from the ideal supercell to create the defective supercell.
μ_i	Chemical potential of atomic species i .
E_i	Energy per atom of atomic species i in the elemental state.
q	Integer charge state.
E_{corr}	Correction energy for periodic imaging by density functional theory in formation energy calculations.
N_s	Concentration of unique sites where defects of a specific type can form.
Q	The total charge collected from an incident radioactive particle.
$\frac{dQ}{dx}$	The differential charge generated per unit length by an alpha particle.
x_r	The stopping range of an incident radioactive particle.
L_d	The minority carrier diffusion length which is proportional to the square root of the minority carrier trapping time.
C_{SS}	Steady-state capacitance of a Schottky barrier diode at an applied bias.
C_T	The capacitance of a Schottky barrier diode if N_{eff} was replaced with n_T .
ΔC	Maximum change in capacitance due to charge trapping at the steady-state bias in capacitance mode DLTS.

t_1	Initial measuring time in deep level transient spectroscopy.
t_2	Second measuring time in deep level transient spectroscopy.
Φ_{B0}	The average barrier over the entire surface of the Schottky barrier.
v_R	Richardson velocity. The average velocity at which carriers are ejected past the Schottky barrier by thermionic emission.
v_D	Drift-diffusion velocity. The average velocity at which charge carrier can diffuse through the space-charge region. Roughly equivalent to the drift velocity.
v_{eff}	Effective carrier velocity between thermionic emission and diffusion at which carrier move through Schottky diode.
I_0	Reverse saturation current density
I_{p0}	Reverse saturation current density of a low barrier patch.
A_p	Area of a low Schottky barrier patch at the metal-semiconductor interface.
Φ_p	Barrier height of the low barrier patch.
$\mu_{PF}n_0$	Trap-assisted mobility-carrier density product.
E_a	Activation energy.

LIST OF ABBREVIATIONS

BNL.....	Brookhaven Nation Lab
BPD.....	Basel Plane Dislocation
CAV	Carbon Antisite-Vacancy
CTS	Current Transient Spectroscopy
C-V.....	Capacitance-Voltage
CVD	Chemical Vapor Deposition
C-V-T.....	Temperature-Dependent Capacitance-Voltage
CZT.....	Cadmium Zinc Telluride
DFT.....	Density Functional Theory
DLTS.....	Deep Level Transient Spectroscopy
EMI.....	Electromagnetic Interference
ENDF	Evaluated Nuclear Data File
FNV.....	Freysoldt-Neugebauer-Van de Walle
FWHM	Full Width Half Maximum
GaAs	Gallium Arsenide
GaN.....	Gallium Nitride
GGA.....	Generalized Gradient Approximation
HPGe.....	High Purity Germanium
HSE.....	Heyd-Scuseria-Ernzerhof
HVR	High Voltage Region
I-V	Current-Voltage

I-V-T	Temperature-Dependent Current-Voltage
LVR.....	Low Voltage Region
MCA	Multichannel Analyzer
MP.....	Micropipe
M-S	Metal-Semiconductor
NASA.....	National Aeronautics and Space Administration
NIST.....	National Institute of Standards and Technology
PAW.....	Projected Augmented Wave
PBE	Perdew-Burke-Ernzerhof
PCB.....	Printed Circuit Board
PHS	Pulse Height Spectroscopy
PICTS.....	Photoinduced Current Transient Spectroscopy
RCA	Radio Corporation of America
SBD.....	Schottky Barrier Diode
Si	Silicon
SiC.....	Silicon Carbide
SNR.....	Signal-to-Noise Ratio
SRIM.....	Stopping and Range of Ions in Matter
TED.....	Thermionic Emission-Diffusion
TED.....	Threading Edge Dislocation
VASP	Vienna Ab initio Software Package

CHAPTER 1

INTRODUCTION

1.1 4H-SiC DETECTORS FOR HARSH ENVIRONMENT

Radiation detectors which can withstand harsh environments—extreme temperatures and high background radiation fields—are essential for a variety of applications in NASA space missions, nuclear safeguards, nuclear reactor core monitoring, and high energy physics experiments. For example, within the last few years, there has been considerable interest among the international community to return to the Earth’s moon for future surface chemistry characterization experiments [1]. Cosmic rays from the sun and beyond predominantly consist of fast protons and other heavy ions which collide with and penetrate the lunar surface [2]. This activates the nuclei of atoms on the lunar surface producing alpha particles with specific energies related to the activated materials [3]. Direct charge conversion radiation detectors or simple ‘radiation detectors’ can accurately determine the exact energy of these particles allowing them to be correlated with the surface and subsurface chemistry. However, the cosmic ray interactions additionally produce uncharged fast neutrons and heavy gamma rays which along with the charged radiation from cosmic rays can damage the detectors and spectrometric equipment. In 2020, it was determined by China’s Chang’E lander mission that the background radiation dose from uncharged and charged radiation was 3.1 and 10.2 $\mu\text{Gy}/\text{hour}$, respectively, which is roughly equivalent to a neutron fluence of 10^9 cm^{-2} (assuming $\sim 1 \text{ MeV}$ neutrons) [4]. Furthermore, the temperature of the lunar surface can vary rapidly from 80 K to 400 K

requiring materials with high thermal conductivity and which can withstand high temperatures [5]. Another harsh environment detector application is nuclear safeguards. One of the current challenges facing the United States Nuclear Regulatory Committee (NRC) is *in-situ* monitoring of nuclear waste caskets to minimize the health risks faced by waste storage site employees due to radiation exposure [6]. A typical dry waste casket used to store spent fuel can exceed 300 °C making most radiation detectors completely inoperable [7].

Table 1.1 Comparison of 4H-SiC properties with other materials at 300 K.

	HPGe	Si	GaAs	CdTe	4H-SiC	GaN	CVD Diamond
Z	32	14	31,33	48,52	14,6	31,7	6
E_g (eV)	0.66	1.11	1.42	1.44	3.27	3.39	5.47
ϵ (eV)	2.95	3.62	4.3	4.43	7.28	8.9	12
κ (W/cm K)	0.58	1.5	0.55	0.06	4.9	1.3	24
ρ (g/cm ³)	5.33	2.33	5.33	5.65	3.24	6.15	3.51
μ_n (cm ² /Vs)	3900	1400	8500	1100	1020	2000	4500
μ_p (cm ² /Vs)	1900	480	400	100	120	200	3800
v_{sat} (10 ⁷ cm/s)	0.6	1	1	1.3	2	2	2
E_{BD} (MV/cm)	0.1	0.3	0.4	-	3	5	10

Radiation detectors require a wide variety of material properties for high resolution radiation detection [8, 9]. First and foremost, they must have good charge transport properties such as high saturation charge carrier velocities v_{sat} or high carrier mobilities

μ_n and μ_p . This maximizes the rate at which particles can be detected and minimizes the amount of charge trapping from defects. Additionally, the material should have a low electron-hole pair creation energy ϵ to achieve a high signal-to-noise ratio (SNR). For harsh environment applications, detector materials additionally need a wide bandgap E_g to minimize the thermal noise at high temperatures and should have a high thermal conductivity to stabilize quickly in environments with rapid thermal fluctuation. Finally, it should have high atomic displacement energies and low atomic numbers to minimize radiation damage. Table 1.1 show a comparison of the essential properties of radiation detectors between various semiconductor materials [8, 10-17]. From this list, the only materials with bandgaps wide enough to withstand temperatures well above room-temperature are 4H-SiC, GaN, and diamond. While GaN certainly shows promise for high temperature applications, the high atomic number of Ga ($Z = 31$) makes it more susceptible to radiation damage from uncharged radiation than either diamond ($Z = 6$) or 4H-SiC ($Z = 6$ and 14), and the poor thermal conductivity makes it unsuitable for thermally unstable environments. The only radiation detector materials which can operate effectively in environments with both high temperatures and high radiation backgrounds are 4H-SiC and chemical vapor deposition (CVD) diamond. However, detector grade CVD diamond is a less mature material and much more costly to produce than 4H-SiC. Additionally, 4H-SiC integrated circuits are proven continuously operable up to 1000 °C [18] and have high atomic displacement energies (19 eV for C and 42 eV for Si) making it resistance to low energy radiation [19]. As a result, 4H-SiC is the material of most interest for harsh environment applications [20-24]. Indeed, Schottky barrier detectors (SBDs) fabricated on epitaxial 4H-SiC are well established as high-resolution radiation detectors of charged

particles with a best resolution to date of 0.25% full width half maximum (FWHM) for ^{241}Am alpha particles [25, 26].

1.2 IMPORTANCE OF DETECTOR THICKNESS

The drawback of 4H-SiC is that the low atomic numbers of its constituent atoms Si ($Z = 14$) and C ($Z = 6$)—the source of 4H-SiC's radiation hardness—make it nearly transparent to uncharged radiation such as X-/gamma-rays. Charged radiations such as alpha particles deposit energy continuously over the full range of the incident particle and can be fully collected with a relatively small active area thickness ($\approx 18.22 \mu\text{m}$ for 5486 keV alpha particles). On the contrary, photons will normally generate electron-hole pairs at only a single point of interaction and can pass through materials without generating any charge. The key parameter for determining the likelihood of an interaction within the active region occurring is called the linear attenuation coefficient or its reciprocal, attenuation length, which describes the mean distance a photon can travel before scattering and causing ionizations. The total attenuation coefficient is the sum of the component attenuation coefficients for the different types of ionization events that can occur: photoelectric absorption, Compton scattering, and pair production [27]. Photoelectric absorption occurs at lower energies and results in all energy of the incident photon being converted into electron-hole pairs. At higher energies, Compton scattering becomes more likely and only a portion of the charge is collected depending on the scattering angle. Pair-production is a high energy physics phenomena that creates two oppositely charged real electrons. For radiation detection, photoelectric absorption is preferred because there is a one-to-one mapping between the energy of the charged particles and the charge collected.

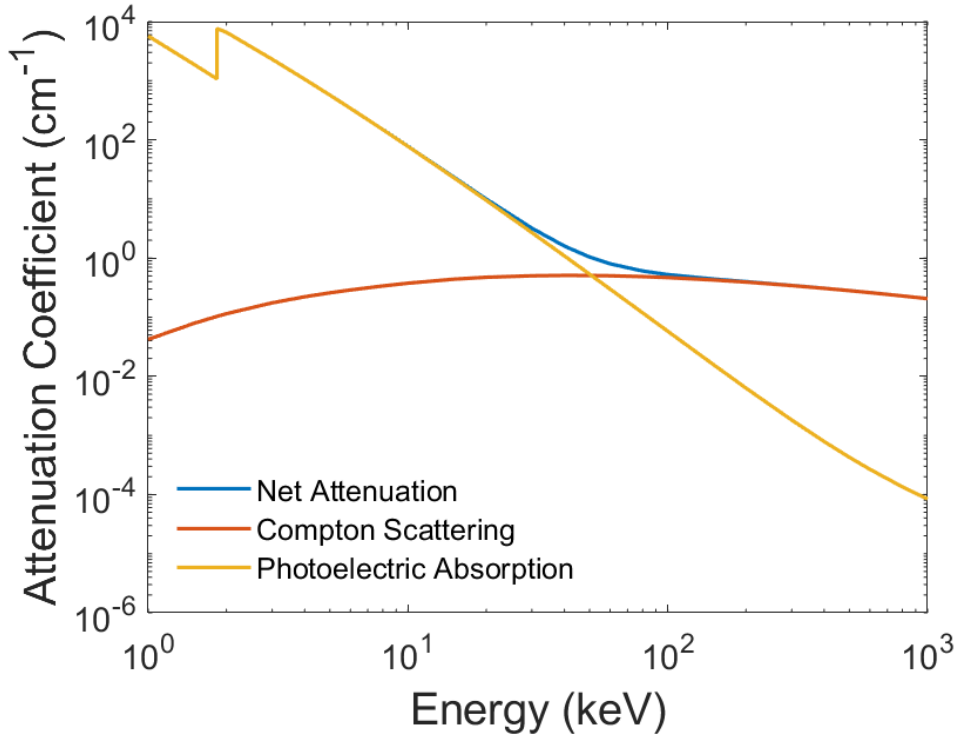


Figure 1.1 Linear Attenuation coefficients of 4H-SiC for high energy photons ranging from 1 keV to 1 MeV simulated using NIST’s XCOM program.

Figure 1.1 shows the linear attenuation coefficients for 4H-SiC obtained from NIST’s XCOM photon cross-section database [28]. From the graph, the photoelectric absorption attenuation length of 4H-SiC for a 5 keV photon would be $\approx 10 \mu\text{m}$ making it relatively easy to capture with most 4H-SiC devices. However, a 50 keV low energy gamma ray would have an attenuation length greater than 1 cm making the probability of collection extremely low. Per Beer-Lamberts laws, the collection probability is related to the linear attenuation coefficient by,

$$Pr(x) = 1 - \exp(-\alpha x) \tag{1.1}$$

where, x is the thickness of the active region and α is the linear attenuation coefficient.

Figure 1.2 displays the collection probability of a typical low energy X-ray Fe-55 (5.19

keV) and low energy gamma ray Am-241 (59.5 keV) as a function of the active region thickness in 4H-SiC. At 10 μm , Fe-55 has $\approx 50\%$ chance of being collected and improves to 99% at 100 μm . Over the same range, the probability of Am-241 being detected improves from less than one thousandth to less than one hundredth. The probability is still low, but there is a clear linear improvement in detection probability with thickness, and as long as the particle count rate is higher than the background noise count rate, the particle will be detectable.

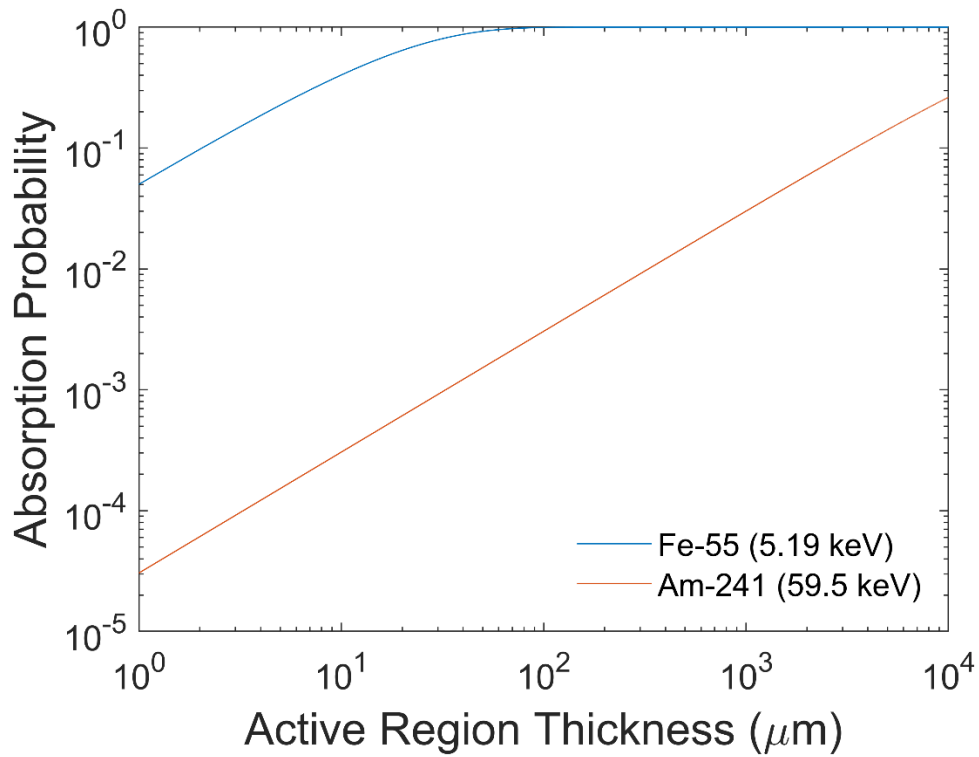


Figure 1.2 Probability of photoelectric adsorption occurring within the detector as a function of the depletion width for ^{55}Fe X-rays (5.19 keV) and ^{241}Am (59.5 keV) gamma rays.

Large thicknesses are readily available for bulk semi-insulating 4H-SiC; however, semi-insulating 4H-SiC is usually vanadium doped [29] which introduces a large concentration of trapping centers making high resolution radiation detection impossible [30-32]. For this reason, most high resolution 4H-SiC radiation detectors are Schottky barrier diodes (SBD) fabricated on high quality epitaxial 4H-SiC with a low concentration of intrinsic defects. ^{241}Am (59.6 keV) gamma rays have been detected in 4H-SiC SBDs with epilayer thicknesses as low as 16 μm , and it has been observed that both the responsivity and resolution of the detector improves as the thickness increases with a resolution of 2.1 % reported for 124 μm epilayers [33-36]. Hence, there is clear motivation for fabricating 4H-SiC SBDs on as thick epitaxial layers as possible.

1.3 DISSERTATION OVERVIEW

The main purpose of this dissertation is the study of Ni/4H-SiC Schottky barrier radiation detectors fabricated on 4H-SiC epilayers of thicknesses up to 250 μm for harsh environment radiation detection applications. Epilayers as thick as possible are necessary for detection of low energy X/gamma-rays. To date, 250 μm epilayers are the thickest epilayers in the world being applied for radiation detection and this is the first dissertation to report on radiation detectors with epilayers of such thickness.

Chapter 2 is a discussion on the physics, operation, and fabrication of 4H-SiC Schottky barrier detectors and an evaluation of the device performance of the detectors fabricated on 250 μm epitaxial layers. This chapter begins with a description of thermionic emission-diffusion (TED) theory before moving onto the fabrication process of the detectors. The fabricated 250 μm detectors are then characterized via current-voltage (I-V)

and capacitance-voltage (C-V) measurements in terms of TED theory. Finally, the detectors are characterized for their radiation detection performance through pulse height spectroscopy (PHS) measurements.

Chapter 3 is an introduction to defects in 4H-SiC and their influence on radiation detection. This chapter begins with a discussion of charge trapping by defects and its effect on radiation detection performance. Next, the primary performance limiting defects in 4H-SiC are discussed in terms of their physical meaning based on first principles calculations. To correlate radiation detection properties with these performance limiting defects, defect parameters of detectors fabricated on 50, 150, and 250 μm epitaxial layers are extracted using a drift-diffusion model for charge collection and capacitance mode deep level transient spectroscopy (DLTS) measurements.

Chapter 4 marks the start of harsh environment characterization of the detectors with a study on the leakage current variation with temperature on a 150 μm detector. Here, both surface barrier inhomogeneities and trapping centers in the device structure are correlated with increases in the detector reverse bias leakage current at elevated temperature.

Chapter 5 is a harsh environment study on the effect of super cadmium filtered fast neutrons on 250 μm epitaxial layers. The radiation detection performance is correlated with neutron dose and the creation of new deep levels in the detectors' DLTS spectra. These new defects are correlated with silicon displacement-related point defects calculated from first principles.

Finally, Chapter 6 is the conclusion to this dissertation and provides suggestions for future work in this area.

CHAPTER 2

4H-SIC SCHOTTKY RADIATION DETECTORS FABRICATED ON 250 μm EPITAXIAL LAYERS

2.1 PHYSICS OF SCHOTTKY BARRIER DIODES

When radioactive particles interact with a semiconductor material, this generates electron-hole pairs within the device. Applying an electric field then causes the charge pairs generated within the active region to drift towards their respective electrodes producing a radiation induced current pulse which can be processed and interpreted by a detection system so long as the current pulse is sufficiently greater than the DC dark current. Increasing the electric field strength across the active region can increase the induced current, but will also increase the DC dark current requiring the material to either be highly resistive or the device to be rectifying. The two main types of rectifiers are p-n junction diodes and SBDs. For radiation detectors, SBDs are preferred over p-n junctions for their faster timing resolution and direct access to the active volume through the detector window.

A Schottky barrier diode is a type of semiconductor device formed from the junction between a metal contact and the surface of a semiconductor. This type of junction is called a Schottky contact and occurs with n-type semiconductors when the work function of the metal Φ_m is greater than the work function of the semiconductor Φ_s . Figure 2.1 demonstrates this with a schematic of the band diagram for this category of junction both before and after Schottky contact formation. Initially, the fermi-level of the semiconductor

E_F is above the fermi-level of the metal E_{Fm} which will force electrons in the metal to build up at the surface inducing a negative potential. This potential pushes electrons in the semiconductor away from interface causing the conduction and valence bands edges, E_C and E_V , to bend until the fermi level in the semiconductor is equal to the metal. The potential barrier between the metal fermi-level and E_C immediately at the junction is called the barrier height ϕ_B and is ideally equal to the difference between Φ_m and the semiconductor electron affinity χ_s .

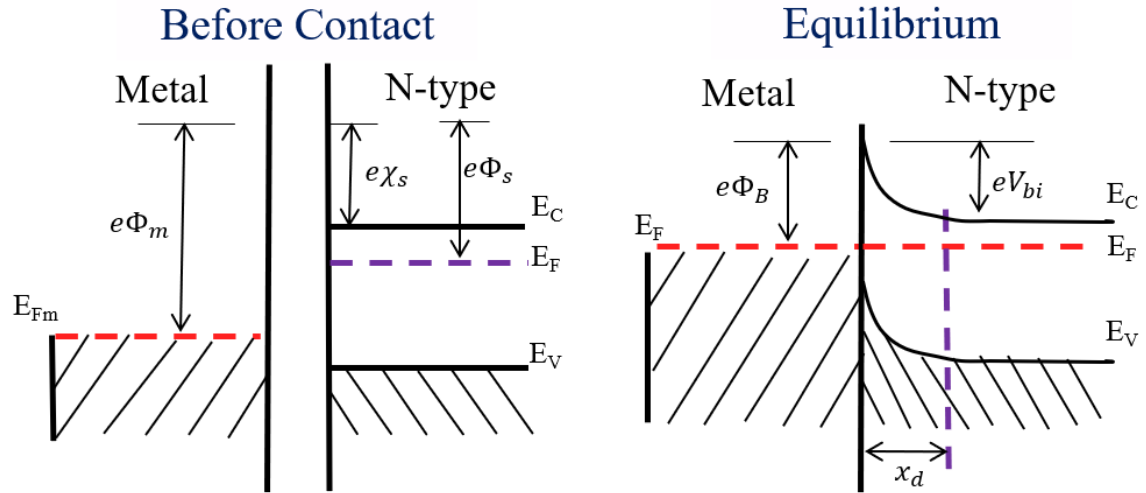


Figure 2.1 Energy band diagram for a Schottky junction between a metal and an n-type semiconductor (a) before contact and (b) at equilibrium.

In the semiconductor, the surface charge induces a potential gradient that can be described by the one-dimensional Poisson's equation given as [37],

$$\frac{d^2\phi}{dx^2} = -\frac{e}{\epsilon} [p(x) - n(x) + N_{eff}]. \quad 2.1$$

Here, $\phi(x)$ is the electrostatic potential in the semiconductor, e is the elementary charge of an electron, ϵ is the electric permittivity of the semiconductor (8.55×10^{-13} F/cm in 4H-

SiC), $p(x)$ and $n(x)$ are the free hole and electron concentrations, respectively, and N_{eff} is the net donor or effective carrier concentration. $\phi(x)$ has the boundary conditions of $\phi(0) = -V_{bi}$ and $\phi(\infty) = 0$ where V_{bi} is the built-in voltage across the semiconductor. In an n-type semiconductor, the free hole concentration is assumed to be negligible whereas the free electron concentration is a function of the electrostatic potential described by Eqn. 2.2.

$$n(x) = N_{eff} \exp\left(\frac{\phi(x)}{k_B T}\right). \quad 2.2$$

Here k_B is Boltzmann's constant and T is absolute temperature in Kelvin. Clearly, Eqn. 2.1 is impossible to solve analytically. However, Eqn. 2.2 falls off exponentially allowing the problem to be resolved by introducing a parameter called the depletion width x_d defined such that for $x < x_d$, $n(x) \ll N_{eff}$ and $\phi(x_d) \approx 0$. Thus, Eqn. 2.1 can now be solved analytically. Integrating Eqn. 2.1 once returns the position dependent electric field strength within the semiconductor as

$$E_x(x) = -\frac{d\phi}{dx} = \frac{eN_{eff}}{\epsilon}x + E_m, \quad 2.3$$

where E_m is the electric field strength at the M-S interface. Assuming the electric field is zero in the neutral region beyond x_d ,

$$E_m = -\frac{eN_{eff}}{\epsilon}x_d. \quad 2.4$$

Integrating Eqn. 2.1 once again and using Eqns. 2.3 and 2.4 gives the electrostatic potential between the surface and x_d , now referred to as the space-charge region or depletion region, as shown below,

$$\phi(x) = -\frac{eN_{eff}}{2\epsilon}x^2 + \frac{eN_{eff}}{\epsilon}x_dx + \phi(0). \quad 2.5$$

Using the boundary condition $\phi(x_d) = 0$, x_d is derived to Eqn. 2.6 below,

$$x_d = \sqrt{\frac{2\varepsilon(-\phi(0))}{eN_{eff}}}. \quad 2.6$$

In terms of radiation detectors, the implication is that both the electric field strength and active region thickness are a function of the square root of the surface potential. Under bias conditions, the surface potential changes to $\phi(0) = -(V_{bi} - V)$ where V is the applied bias allowing both the electric field strength and depletion width be controlled by the applied bias.

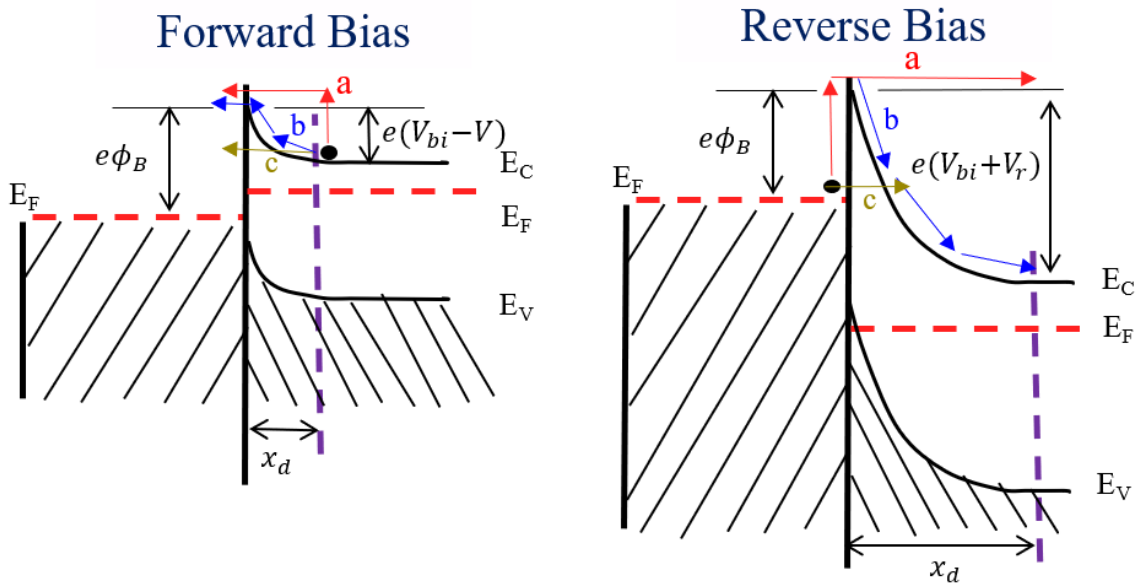


Figure 2.2 Energy band diagram of Schottky contact under forward bias and reverse bias. The current transport mechanisms are (a) thermionic emission, (b) diffusion (drift under reverse bias), and (c) tunneling.

At equilibrium, E_F is aligned in both the metal and semiconductor making electrons equally likely to move from one side of the junction to the other producing a net current of zero. Applying a forward bias voltage pushes E_F above E_{Fm} reducing the surface potential

barrier by the applied bias allowing electrons to move from the semiconductor to the metal more readily. Under reverse bias, E_F is pushed below E_{Fm} increasing the surface potential by the applied voltage, and thus electrons can only flow from the metal to the semiconductor if they can surmount Φ_B . Figure 2.2 illustrates the various current flow mechanisms that can occur under forward and reverse bias. The most common mechanism is thermionic emission which states that electrons can be thermally excited above the potential barrier at which point they will be swept up by the strong electric field. Assuming the drift velocity is sufficient high, the current density will be rate limited by how often charges jump the barrier and can be described by the Bethe thermionic emission model given in Eqn. 2.7 [38, 39],

$$J = A^*T^2 \exp\left(-\frac{\Phi_B}{k_B T}\right) \left[\exp\left(\frac{eV}{nk_B T}\right) - 1 \right]. \quad 2.7$$

Here, A^* is the effective Richardson coefficient of the material ($146 \text{ A cm}^{-2} \text{ T}^{-2}$) and n is an ideality factor introduced to describe nonidealities in the forward bias current. The second most common type of current flow is diffusion current of electrons along the electron concentration and is described by drift-diffusion theory as [39],

$$J = e\mu_n E_m N_C \exp\left(-\frac{\Phi_B}{k_B T}\right) \left[\exp\left(\frac{eV}{nk_B T}\right) - 1 \right]. \quad 2.8$$

In Eqn. 2.8, N_C is effective density of states of the conduction band ($1.6 \times 10^{19} \text{ cm}^{-3}$ in 4H-SiC at room temperature). This equation has a similar form to Eqn. 2.7 albeit with a linear dependence on the electric field. Combined Eqns. 2.7 and 2.8 are referred to as thermionic emission-diffusion (TED) theory which states that the slower of the two mechanisms will dominate. The last common transport mechanism is tunneling through the Schottky barrier

[39]. It has no temperature dependence and is usually negligible in low-doped Schottky barrier diodes.

2.2 FABRICATION OF Ni/N-4H-SiC SBDS

4H-SiC Schottky barrier diode radiation detectors were fabricated on epitaxial layers of thicknesses up to 250 μm . The epilayers were grown by hot wall chemical vapor deposition on the (0001) face of a 100 mm diameter, 350 μm thick bulk 4H-SiC substrate with a low n-type resistivity of 0.015-0.028 $\Omega\text{-cm}$. The two most damaging structural defects in 4H-SiC are basal plane dislocations (BPD) and micropipes (MP). Prolonged use of devices fabricated on BPDs will introduce stacking faults, degrading device performance over time. They can be eliminated through KOH etching or conversion into threading edge dislocations (TED). TEDs are benign and form more easily from BPDs when epilayers are grown slightly off axis or at higher C/Si ratios [40-43]. MPs are a type of threading screw dislocation which act as highly conductive channels completely killing device rectification and leading to premature breakdown. They originate from the substrate and are more likely to close at lower C/Si ratios [43-46]. The present epilayers were grown on a substrate with an ultralow areal MP density of $\sim 0.11 \text{ cm}^2$ at an 8° offcut towards the $\langle 11\bar{2}0 \rangle$ direction. The net donor concentrations of the epilayers were $(1-2) \times 10^{14} \text{ cm}^{-3}$ due to unintentionally nitrogen doping. Following growth, the parent wafer was diced into $8 \times 8 \text{ mm}^2$ samples to be used as substrates for device fabrication.

Next, the samples are cleaned and prepped for metal deposition using a 5-stage process based on the Radio Corporation of America (RCA) method [47]. The first stage is cleaning with inorganic solvents to remove organic contaminants introduced in the processing of the samples after growth. The sample is first wiped with a cotton swab soaked

with boiling trichloroethylene, and then in rapid succession, the samples are dipped into boiling trichloroethylene, acetone, and methanol for three minutes each.

The second stage uses a ‘base piranha’ solution of $\text{H}_2\text{O}/\text{H}_2\text{O}_2/\text{NH}_4\text{OH}$ (5:1:1) to remove any organic residue left over from the previous stage. $\text{H}_2\text{O}/\text{NH}_4\text{OH}$ (5:1) is first heated to 100°C to ensure that H_2O_2 reacts with NH_4OH . H_2O_2 is then slowly poured into the solution before dipping the sample for 5 minutes.

The third stage is an ionic cleaning with an ‘acidic piranha’ solution of $\text{H}_2\text{O}_2/\text{H}_2\text{SO}_4$ (2:5) for 30 seconds to remove any metal contaminants left over from the growth process. It additionally introduces a passivating silicon dioxide layer (a few angstrom) that protects the surface from further contamination. This is fine for conventional electronic devices, but SBDs require the metal to be directly deposited onto the silicon face of the epilayer.

To remove the silicon dioxide layer, the sample is dipped into diluted hydrofluoric acid (~1%) for one minute. Between each of the steps, the sample is rinsed in running deionized (DI) water before finally being dried with an N_2 gun. The dried detectors are immediately taken for metal deposition to avoid any native oxide formation.

The Schottky contacts were formed by DC sputtering Ni onto the Si-face of the square samples using a Quorum Q150T sputtering unit. Ni has a large metal work function of ($\Phi_M \approx 5 \text{ eV}$) resulting in large barrier heights. In SBD radiation detectors, the barrier height needs to be as high as possible to minimize the detector leakage current. Ni is chosen over other high work function metals such as Au or Pt due to its lower atomic number ($Z = 28$) which helps minimize charge loss in the metal. Metal rectangular ($6 \times 6 \text{ mm}^2$) masks with a 2.9-3.9 mm diameter circular opening were placed onto the Si-face of the samples and held in place using a tin foil wrapping. The sample was then placed onto the sample

stage of the sputtering chamber. A sputtering current of 60 A was set for a duration of 10 seconds resulting in the formation of the ~10 nm thick Ni/4H-SiC Schottky contact which is a sufficiently thin to prevent charge loss in the metal. This process was repeated to deposit a 100 nm thick, $6 \times 6 \text{ mm}^2$ Ni contact onto the bulk surface (C-face). Due to the high conductivity of the bulk, this contact was ohmic. Often, the sharp tungsten probes used in the measurement systems can damage the very thin Ni Schottky contacts creating some inaccuracies in electrical measurements. To remedy this, a 100 nm thick, 1 mm diameter gold contact—which is sufficiently small enough in area to not impact radiation detection—is deposited onto the Ni Schottky contact.

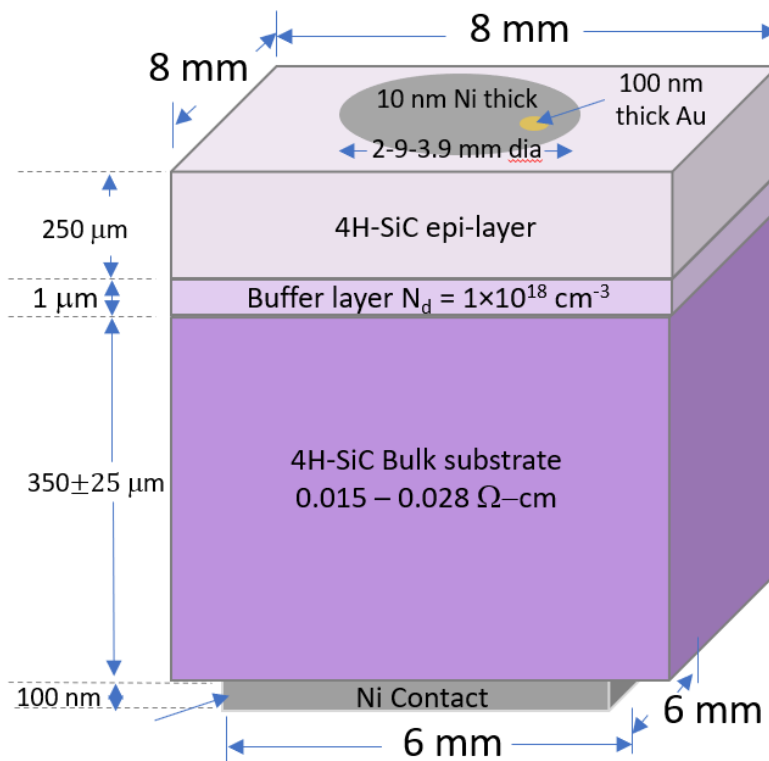


Figure 2.3 Schematic of the device structure of a Ni/n-4H-SiC radiation detector fabricated on 250 μm epitaxial layers.

2.3 ELECTRICAL CHARACTERIZATION MEASUREMENTS

In this study [48], the junction properties of three detectors fabricated on 250 μm epitaxial layers were characterized by current-voltage (I-V) and capacitance-voltage (C-V) measurements. The first two detectors, S1 and S2, had an active area diameter of 3.9 mm whereas the third had a diameter of 2.9 mm. For I-V measurements, the detectors were individually mounted onto a PCB and loaded into an electromagnetic interference (EMI) shielded electronic box connected via low noise triaxial cables to a Keithley 237 source-measure unit. The Keithley 237 can apply ± 1000 V to a device with an error of 10-100 fA in the measured current depending on the range. The source measure unit was then interfaced with a PC for data collection using a LabVIEW based data acquisition program. C-V measurements were taken with a pulse generator capable of outputting ± 12 V and a 1 MHz capacitance meter, both built-in to a SULA DDS-12 system. The samples were loaded into a Janis VPF800 cryostat configured for capacitance measurements and connected to the DDS-12 system via low noise BNC cables.

Figures 2.4 and 2.5 show the forward and reverse bias characteristics of the three detectors, respectively. All three detectors expressed rectifying characteristics under the correct polarities confirming that top contact is Schottky. Thermionic emission theory predicts that relationship between $\ln J$ and V is approximately linear for some voltage range and therefore both the barrier height and ideality factor can be extracted from the linear fit by Eqn. 7. For the present detectors, the barrier heights were calculated to be 1.35, 1.31, and 1.45 eV while the ideality factors were 1.06, 1.00, and 1.08 for S1, S2, and S3, respectively. S1 and S3 had ideality factors slightly greater than one indicating spatial inhomogeneity in the surface barrier height [49]. For all three detectors, the reverse bias

leakage current density remained under 3 nA cm^{-2} . After converting applied bias to the electric field strength at the M-S interface using Eqn. 2.4, it was found that detector S2 had the lowest relative leakage current of the three devices. When compared with other Ni/4H-SiC detectors, the leakage current was most comparable to edge terminated detectors fabricated on $20 \text{ }\mu\text{m}$ epitaxial layers [50].

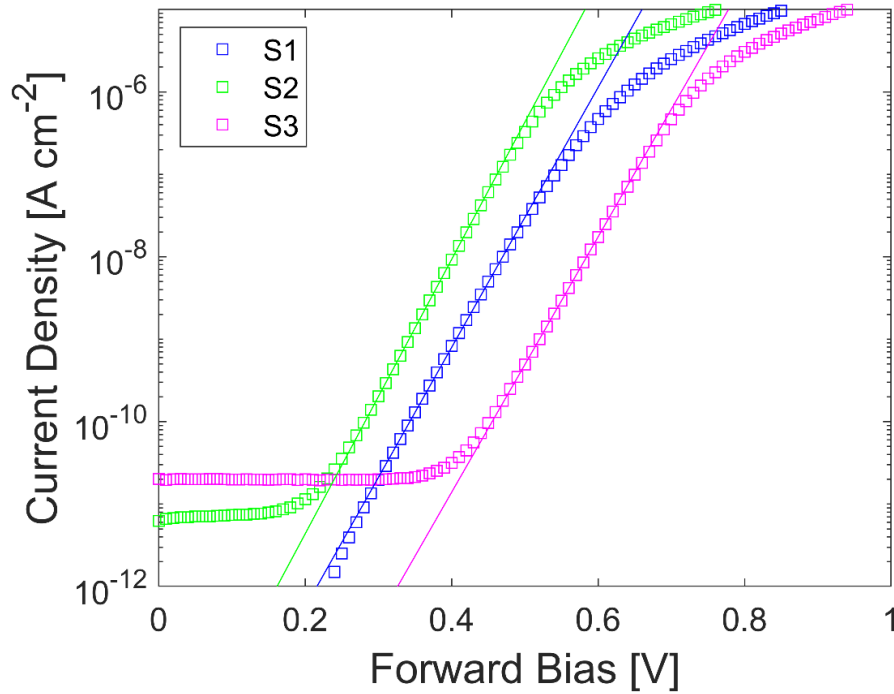


Figure 2.4 Forward bias I-V characteristics for detectors S1, S2, and S3 fabricated on $250 \text{ }\mu\text{m}$ 4H-SiC epitaxial layers. The solid lines represent the straight line fit of the linear region.

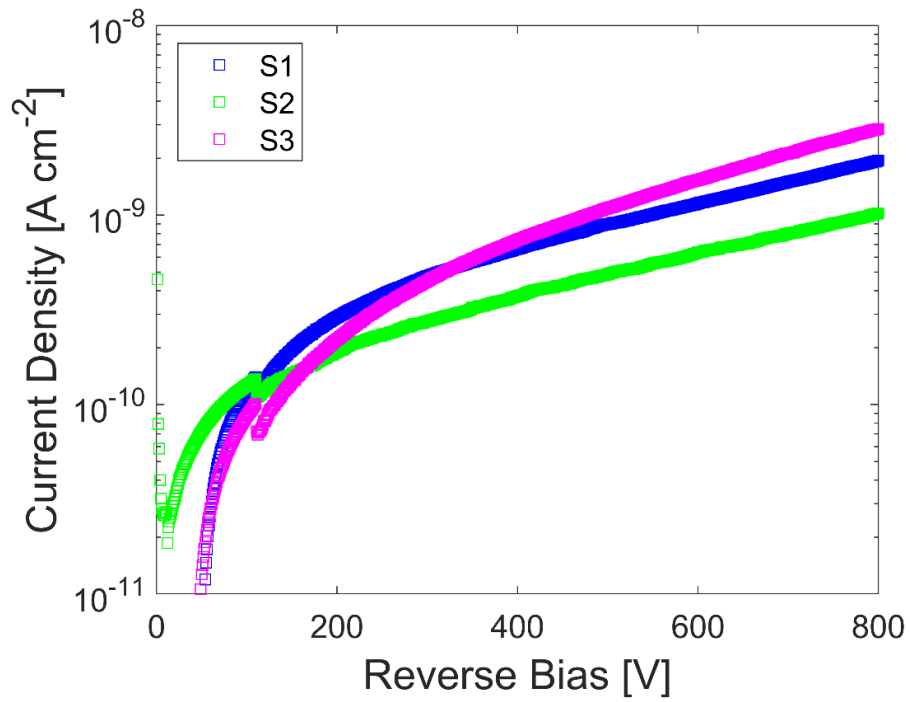


Figure 2.5 Reverse bias I-V characteristics for detectors S1, S2, and S3 fabricated on 250 μm 4H-SiC epitaxial layers.

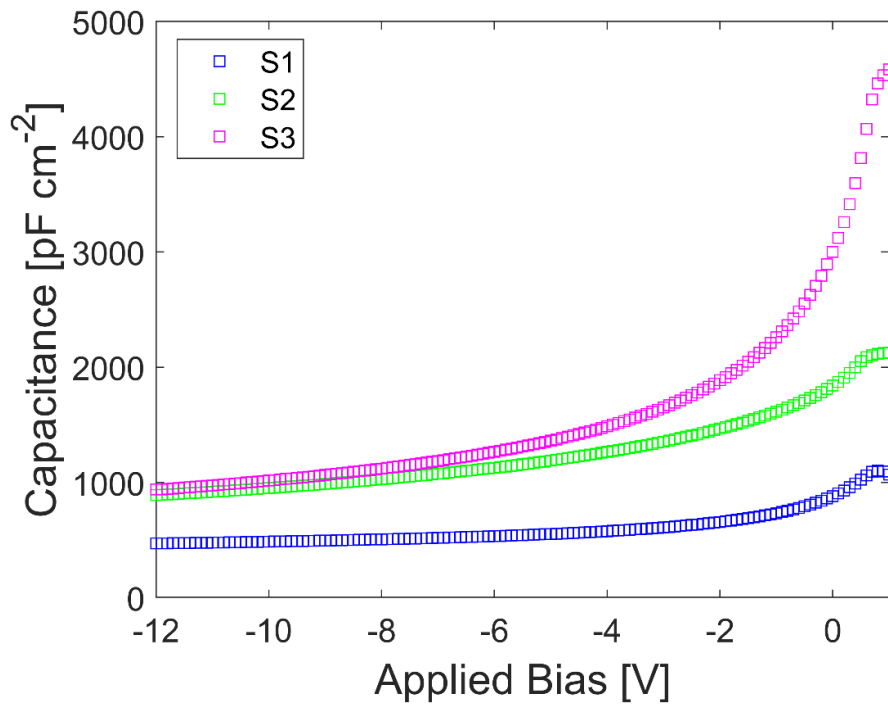


Figure 2.6 Capacitance per unit area as a function of applied bias for the 250 μm Ni/n-4H-SiC epitaxial layer radiation detectors.

Figure 2.6 shows the C-V characteristics of the detectors normalized to the active area of each device. The capacitance of a Schottky diode is proportional to the reciprocal of its depletion width and thus varies with $1/\sqrt{V_{bi} - V}$. Taking the reciprocal of the capacitance squared results in what is called the Mott-Schottky equation which can be used to extract V_{bi} and the net donor concentration N_{eff} .

$$\frac{1}{C^2} = \frac{2}{A^2 e \epsilon N_{eff}} (V_{bi} - V) \quad 2.9$$

Figure 2.7 displays the plot of $1/C^2$ versus the applied reverse bias. Using Eqn. 2.9, the net donor concentrations were calculated to be 9.8×10^{13} , 1.8×10^{14} , and $1.7 \times 10^{14} \text{ cm}^{-3}$ for S1, S2, and S3, respectively. S1 shows nonlinear behavior at low bias which is indicative of a gradient doping. From the linear fit of the forward bias region, it is estimated that the initial net donor concentration is close to $2 \times 10^{13} \text{ cm}^{-3}$ and then ramps up to 1×10^{14} . From the initial linear fit, the built-in voltages were calculated to be 18.4, 3.9, and 1.3 V, respectively. The forward bias linear fit of S1 gave a built-in voltage of 1.9 V. The Schottky barrier height is equal to the sum of the built-in voltage and the bulk Fermi-level measured relative to the conduction band minimum and is represented by

$$\Phi_B = V_{bi} + k_B T \ln \left(\frac{N_c}{N_{eff}} \right), \quad 2.10$$

where N_c is the effective density of states of the conduction band ($1.6 \times 10^{19} \text{ cm}^{-3}$ in 4H-SiC at 300 K). Using this equation, the barrier heights were calculated to be 2.2 and 1.6 eV for S1 and S3, respectively, which is higher than the values obtained from the I-V measurements. This is because the C-V barrier height corresponds to the average barrier over the entire contact area whereas the I-V barrier height is an effective value resulting from current preferring to pass through the low barrier regions of a spatially

inhomogeneous barrier [49, 51]. S2's built-in voltage was too high to reasonably be correlated with the barrier height. A high built-in potential usually indicates either minor gradient donor or the presence of some dielectric layer between the metal and semiconductor surface [52]. Since the ideality factor of S2 was almost exactly one, it can be assumed that the average and effective barrier height are the same.

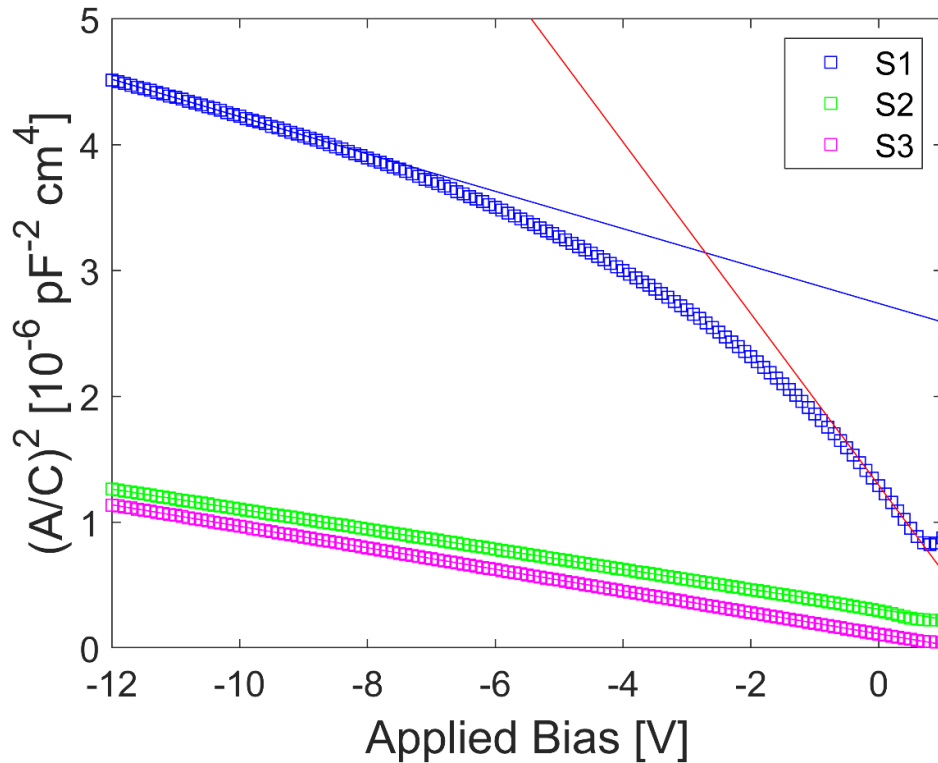


Figure 2.7 Mott-Schottky plots of the detectors S1, S2, and S3. The solid lines are straight-line fits for calculating the effective doping concentration at two different bias regimes.

One of the challenges of 250 μm epilayers is the extreme bias needed to fully deplete them. Solving Eqn. 2.6 for the full depletion bias shows that the bias needed to fully deplete a detector increases quadratically with the thickness of the epilayer. For example, a detector with a 20 μm epitaxial layer and carrier concentration of 10^{14} cm^{-3}

would only take about 30 V to be fully depleted, whereas 40 μm would require 120 V and 80 μm , 480 V. Using the net donor concentrations of each sample, it is estimated that it would take 5.7, 10.7, and 10.0 kV for S1, S2, and S3, respectively, to fully deplete. The extremely high bias poses two major risks to operating the devices at full depletion. One is that the detectors will undergo breakdown long before being fully depleted. However, as per Eqn. 2.4, the present detectors will have an interfacial electric field of 0.5, 0.9, and 0.8 MV/cm, respectively, which is less than the breakdown electric field of 4H-SiC (≈ 3 MV/cm) and theoretically should survive the high bias.

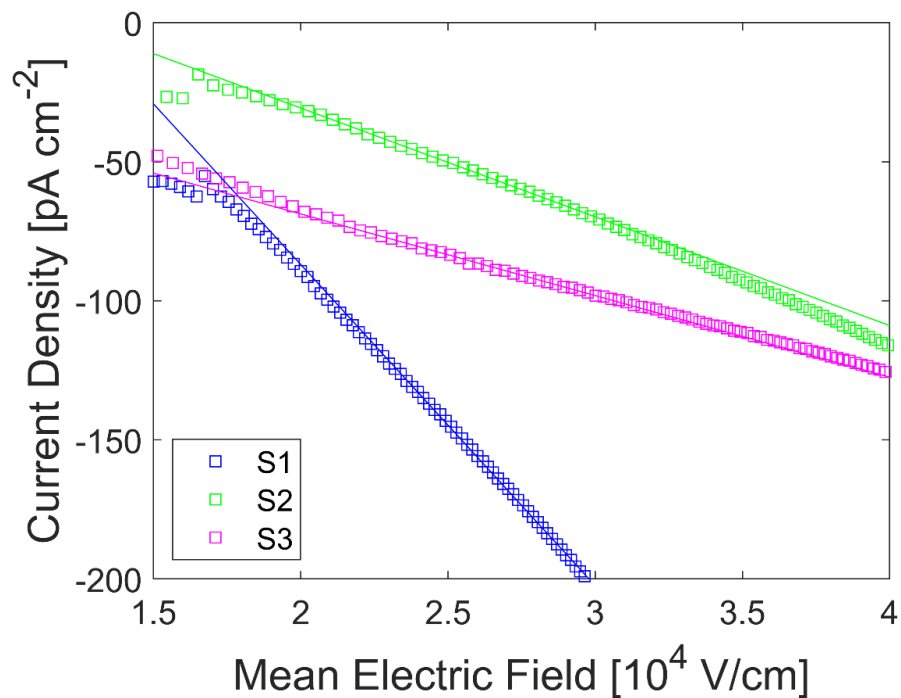


Figure 2.8 Variation of current density under reverse bias as a function of mean electric field across the space charge region. The mean field can be converted to maximum field at the M-S interface by multiplying by 2.

The other major risk is that the reverse bias leakage current will be too high for radiation detection, potentially degrading SNR or damaging the electronic equipment.

Figure 2.8 shows a linear relationship between the leakage current and mean electric field at low to moderate electric fields which indicates that the current could be better described by drift-diffusion theory rather than thermionic emission. Fitting the data to Eqn. 2.8, results in an estimated barrier height of ≈ 1.1 eV for all three samples which is much lower than that obtained using the thermionic emission model. A possible explanation is that thermionic emission was the wrong assumption for the forward bias analysis. Alternatively, the leakage current could be trap assisted through Poole-Frenkel emission which also has a linear electric field dependence making it indistinguishable from diffusion at low to moderate electric fields [53].

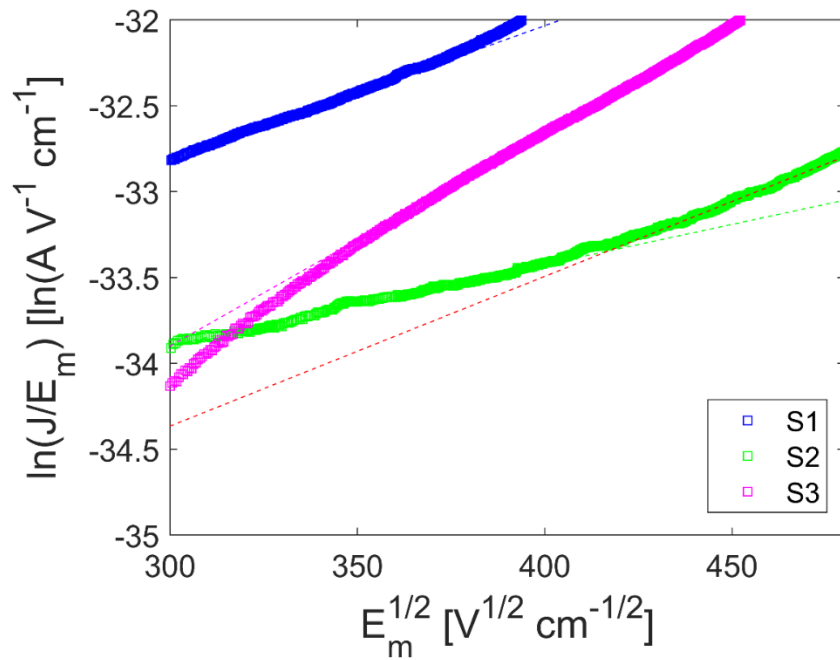


Figure 2.9 Interfacial electric field dependence of the current density J normalized to the interfacial electric field E_m . Dashed lines are the linear fit of experimental data. S2 has a second linear fit in red corresponding to interfacial electric fields greater than 0.2 MV/cm.

At high electric fields, the leakage current starts to increase more substantially due to barrier lowering described by the following equation [39, 53, 54],

$$\Delta\Phi = \frac{1}{m} \sqrt{\frac{eE_m}{\pi\epsilon}}. \quad 2.11$$

Here, m is a scaling factor describing how quickly the barrier is reduced. For Schottky barrier lowering by image charges, the scaling factor is 2, whereas for Poole-Frenkel emission, the scaling factor is 1. Thus, the relative contribution of each mechanism can be identified by the slope of a $\ln J/E_m$ versus $E_m^{1/2}$ plot which has been given for the three detectors in Figure 2.9. For S1 and S3, the scaling factor is 1.2 and 0.8 respectively indicating that current transport is trap assisted. In sample S2, the scaling factor is initially 2.0 before changing to 1.1 at 0.2 MV/cm. How big of an impact barrier lowering will have on the detector leakage current can be estimated by taking the ratio between the expected current at full depletion and the current at some point in the linear region of $\ln J/E_m$ versus $E_m^{1/2}$ as shown below,

$$\frac{J_1}{J_2} = \frac{E_{m1}}{E_{m2}} \exp\left(\frac{\Delta\Phi_1 - \Delta\Phi_2}{k_B T}\right). \quad 2.12$$

Using this relation, it is estimated that at full depletion the current could increase by more than 300 times its value at 800 V with Poole-Frenkel lowering or more than 40 times with Schottky lowering.

2.4 ALPHA PULSE HEIGHT SPECTROSCOPY WITH ^{241}Am

A typical analog spectrometric system consists of a radiation detector, a high voltage power supply, a charge-sensitive preamplifier, a wave shaping amplifier, and a multichannel analyzer. The power supply unit is connected to the detector anode and

cathode through a biasing circuit with a high series resistance ($> 100 \text{ M}\Omega$) to limit the maximum current. Charges generated in the detector are swept up by the electric field generating a current pulse which is then fed into the input of the preamplifier. The preamplifier is a current integrator which produces a voltage signal directly proportional to the charge injected by the detector. These devices are usually amplifier circuits that apply a negative feedback capacitor to produce a voltage signal much larger than the voltage stored on the input capacitor. To prevent saturation, they use a feedback resistor to continuously discharge the feedback capacitor. A shaping amplifier converts the integrated pulse from the preamplifier into a gaussian waveform with an amplitude proportional to the charge collected. The system consists of an input differentiator followed by a fourth order active integrator which together create a semi-gaussian waveform while attenuating high frequency electronic noise. The width of the gaussian waveform is determined by the RC time constant of the input differentiator. The last component is a multichannel analyzer (MCA) which interprets the gaussian waveforms and bins them into a histogram based on the amplitude of the gaussian. As a result, the bin number or 'channel number' is directly proportional to the charge generated in the detector.

The radiation detection performance of detectors S1, S2, and S3 were characterized by the pulse height spectrometer at UofSC (Figure 2.10) with a $0.9 \mu\text{Ci } ^{241}\text{Am}$ alpha source. The detectors were mounted onto PCBs and loaded into an EMI shielded electronic box with the source placed $\approx 1 \text{ cm}$ above the detector. The electronic box was connected to the remainder of the system via a single male-to-male BNC connector. During measurements, the electronic box was kept under continuous vacuum to minimize scattering of alpha particles in air. The spectrometer at UofSC consists of a CR110 preamplifier, a Canberra

3106D high voltage power supply, an ORTEC 572 shaping amplifier, and a Canberra Multiport II multichannel analyzer.

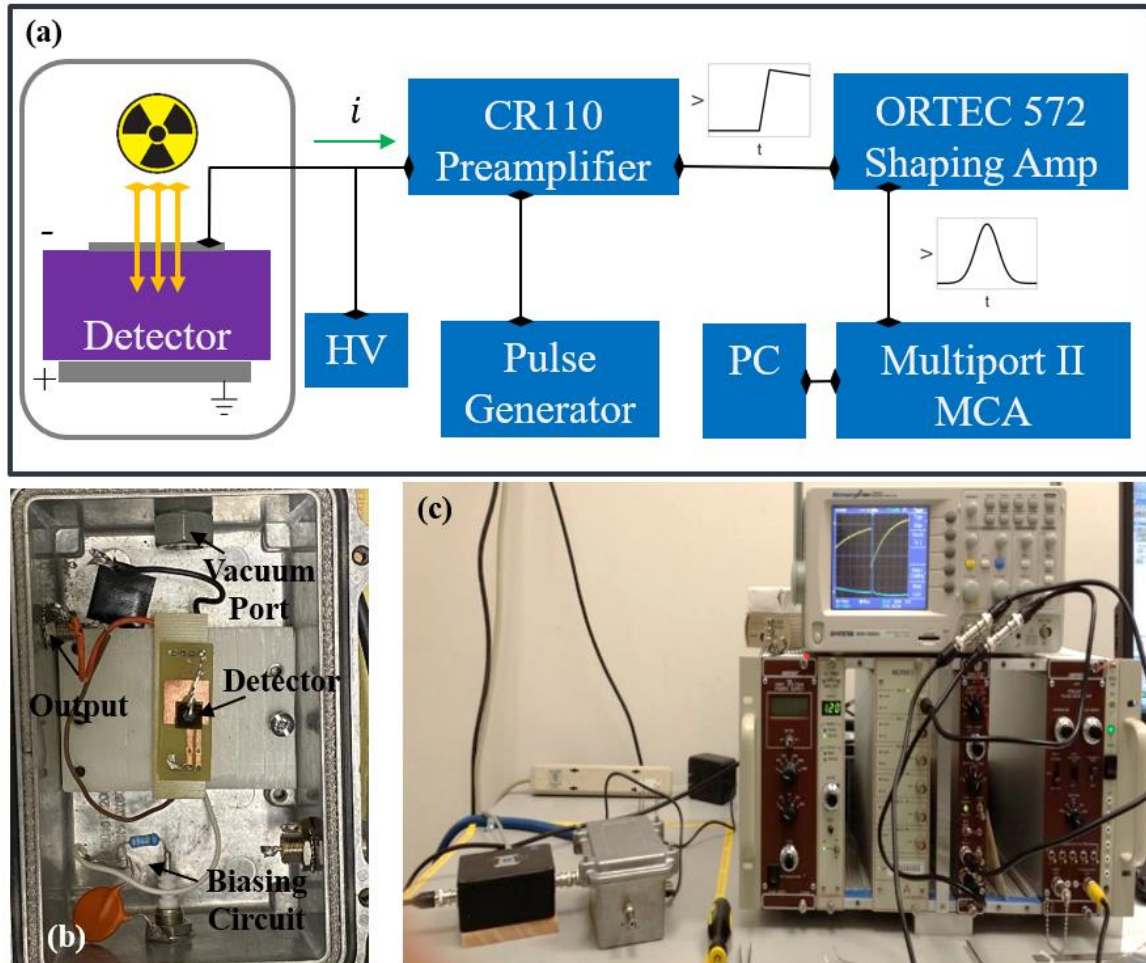


Figure 2.10 Block diagram of the radiation detection system at UofSC (a), a photograph of the electronic box used for radiation detection (b), and a photograph of the radiation detection system (c), used in this work.

The energies of the incident particles were calculated by calibrating the detector with an ORTEC 419 precision pulse generator to charge a calibrated feed-through test capacitor connected to the input of the preamplifier. Due to the low capacitance (2.466 pF),

the capacitor quickly discharges its stored charge into the preamplifier as a current pulse and is eventually binned by the MCA. By adjusting the amplitude of the pulser voltage, a one-to-one linear mapping can be constructed between charge injected and channel number. Multiplying the charge by the electron-hole pair generation energy ϵ (7.28 eV in 4H-SiC [55]) converts the mapping to be between energy injected and channel number. The detector performance was interpreted in terms of energy resolution defined as the full width half maximum (FWHM) of the of primary ^{241}Am alpha peak in keV as a percentage of the centroid energy.

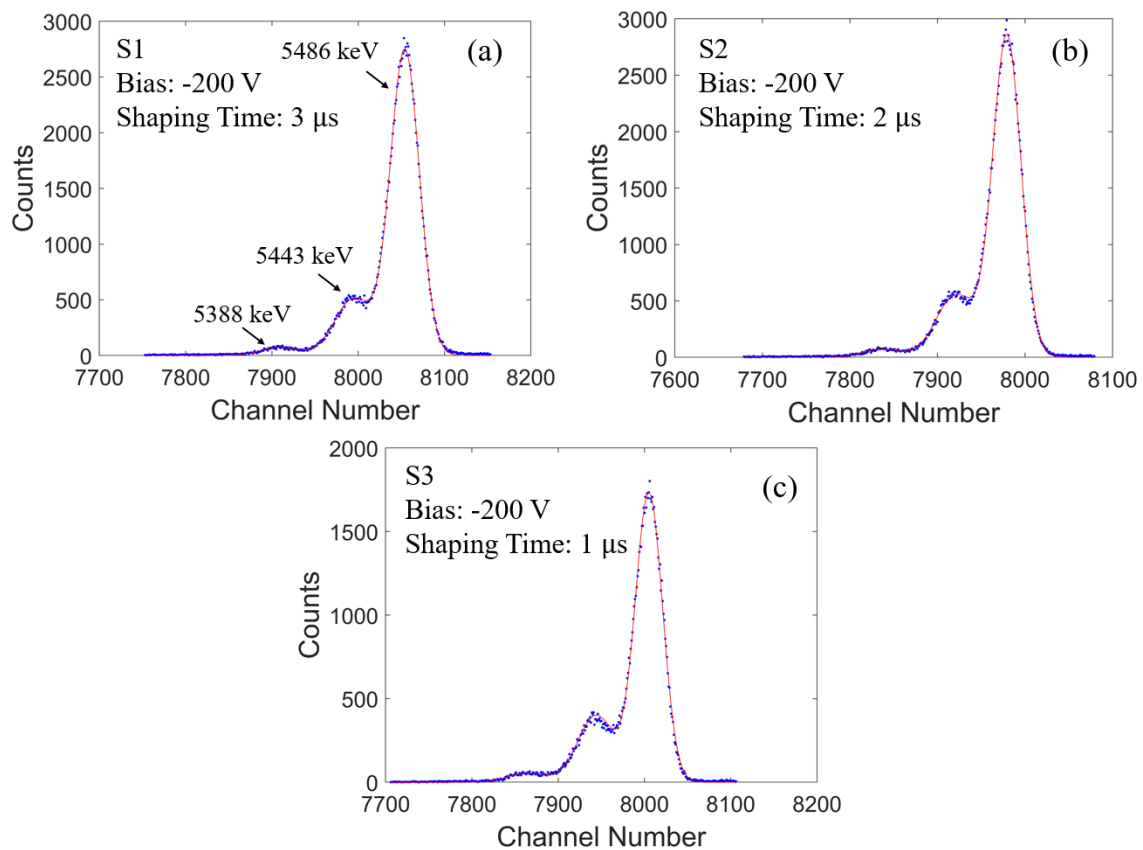


Figure 2.11 ^{241}Am Pulse height spectra obtained for S1 (a), S2 (b), and S3 (c). The solid red lines are the triple Gaussian model fitted overtop the PHS.

The primary alpha decay of ^{241}Am has an energy of 5486 keV which means that the range of the particle is 18.22 μm based on SRIM calculations [56]. To achieve this active region thickness, the detectors would need biases of approximately 30 V for S1 or 60 V for S2 and S3; however, usually the optimal bias is much higher. Figures 2.11 shows the best resolution spectra for each detector. The optimum bias was -200 V for all three detectors whereas the optimum shaping time was 3, 2, and 1 μs for S1, S2, and S3, respectively. ^{241}Am has three closely spaced primary alpha particle energies of 5486 (85%), 5443 (13%), and 5388 (2%) keV. In all three detectors, all three alpha peaks were clearly visible indicating that the detectors are of high resolution. The FWHMs of the 5486 keV peaks were 26.7, 25.6, and 25.1 keV corresponding to resolutions of 0.49%, 0.47%, and 0.46% for S1, S2, and S3 respectively. A summary of the electronic and radiation detection properties of each device is given in Table 2.1.

Table 2.1 Detector parameter obtained for detectors fabricated on 250 μm epilayers.

ID	n	Φ_B (eV)	J @ -800V (nA cm^{-2})	N_{eff} (10^{14} cm^{-3})	Shaping Time (μs)	Energy Resolution (%)
S1	1.06	1.35	1.9	0.97	3	0.49
S2	1.00	1.31	1.0	1.8	2	0.48
S3	1.08	1.45	2.9	1.7	1	0.47

Figure 2.12 shows the pulser peak obtained at the same conditions as detector S3 at the optimum conditions both with and without the detector connected which gives the overall electronic noise of the system. The electronic noise of the system was originally 4.7 keV FWHM (4H-SiC equivalent) without the detector and increases to 10.2 keV

FWHM when the detector is connected to the system. This is because the detector leakage current and the detector capacitance both contribute to the white parallel noise component of the system. The total broadening of the radiation peak is the quadratic sum of the peak broadening from the electronic system $FWHM_{elec}$ and the peak broadening from the detector $FWHM_{det}$ and can be described by Eqn. 2.13 [54].

$$FWHM_{total}^2 = FWHM_{elec}^2 + FWHM_{det}^2. \quad 2.13$$

Detector peak broadening originates from statistical fluctuations in the charge collected which is mostly related to trapping of charge carriers by defects in the crystalline structure. Using 25.1 keV as the total broadening and 10.2 keV as the system broadening, the peak broadening from the detector is calculated to be 22.9 keV indicating that the detector energy resolution is limited by charge carrier trapping.

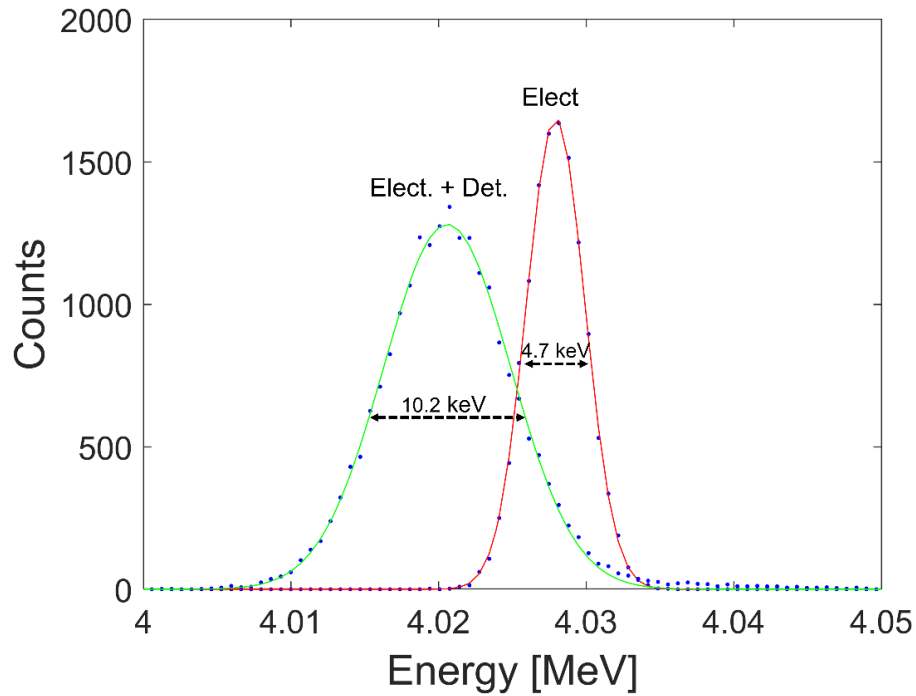


Figure 2.12 Pulsar PHS obtained with and without detector S3 at -200 V and a shaping time of 1 μ s.

2.5 CONCLUSION

Ni/n-type 4H-SiC Schottky barrier diode radiation detectors were fabricated on 250 μm epitaxial layers which are the thickest to date and essential for high resolution gamma spectroscopy with 4H-SiC. The detectors were evaluated for their junction properties in terms of Schottky barrier physics to determine their potential for operation at full depletion. Due to the net donor concentrations $<2 \times 10^{14} \text{ cm}^{-3}$, it was found that it would require up to 10 kV to fully deplete the detectors. This corresponded to an electric field strength at the M-S interface of up to 0.9 MV/cm, which is lower than the breakdown electric field of 4H-SiC, suggesting that the detectors should be able to survive at full depletion without breaking down. From a $\ln J/E_m$ versus $E_m^{1/2}$ model, it was determined that current growth is predominantly trap-assisted and could result in an increase in reverse bias leakage current from 800 V to 10 kV of up to 300 times. Radiation detection measurements showed high energy resolutions of $<0.5\%$ FWHM for all three detectors. Comparison with the peak broadening of a precision pulser fed into the spectrometer revealed that the resolution is predominantly limited by trapping of charge carriers in the detectors.

CHAPTER 3

CORRELATION OF DEFECTS WITH RADIATION DETECTION

3.1 CHARGE TRAPPING IN SEMICONDUCTOR RADIATION DETECTORS

When radiation interacts with a semiconductor detector, electron-hole pairs are produced at the point of interaction x_i which induces charges on the anode and cathode of the device by image charge induction. By superposition, the net charge induced is initially zero due to the electrons and holes occupying the same position. Applying an electric field across the material will cause the holes to drift towards the cathode and electrons towards the anode causing the induced image charge to change creating an electrical current. This current is defined by Shockley-Ramo theorem [57-60] as

$$i(t) = eN(t)v_d(x, t)E_w(x, t), \quad 3.1$$

where N is the number of mobile electrons or holes, $v_d(x, t)$ is the instantaneous drift velocity, and E_w is a weighting field related to the geometry of the anode and cathode. The total charge collected for each charge type is the integral of Eqn. 3.1 over the transit time t_r with the net charge collected being the sum of the individually collected electron and hole charges. Ideally, the amount of charge collected will equal the amount of charge generated and the relative contribution of electrons and holes equal to the ratio of the transit distance to the thickness of the active region of the device.

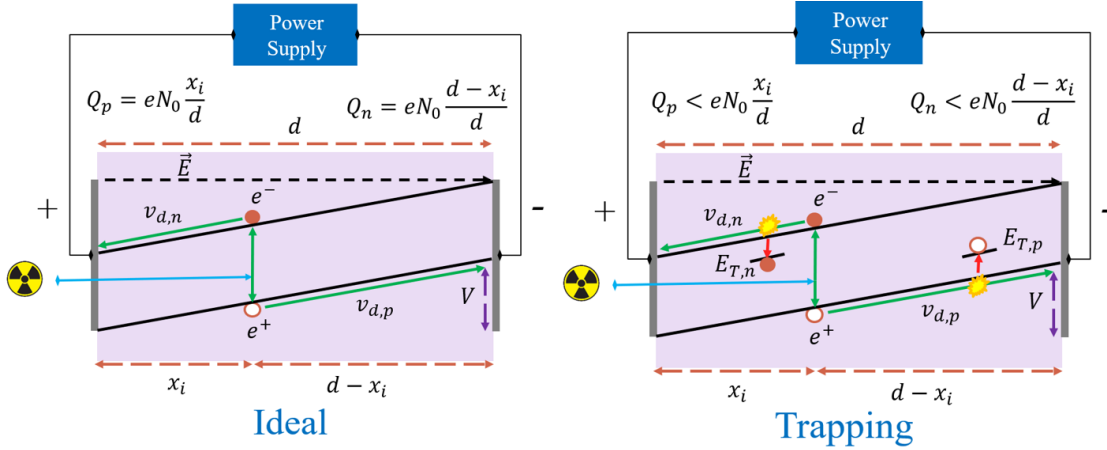


Figure 3.1 Demonstration of charge collection in both an ideal detector and a detector with trapping from defects.

Realistically, charge carriers vibrate statistically at high thermal velocity and have some probability of colliding with point defects in the crystalline structure. Upon collision with an unoccupied defect, charge carriers will stop directional motion, no longer inducing a current on the electrode. The probability of trapping obeys the principles of mean free path where the trapping rate is proportional to how big the traps are and how many traps there are to hit reflected in the traps' capture cross-sections σ_n for electrons and σ_p for holes and trap concentrations N_T . The mean free path of a single trap is defined as the reciprocal of the product between the two. Assuming quasi-random thermal motion is either much faster than or comparable to the drift velocities of the carriers, the mean trapping rate can be described as the reciprocal sum of the mean free paths for multiple traps multiplied by the mean thermal velocities $\langle v_{th,n} \rangle$ and $\langle v_{th,p} \rangle$ for electrons and holes, respectively. The mean trapping time τ_n or τ_p would then be defined as the reciprocal of the trapping rate as illustrated by the following [61],

$$\tau_n = \left[\langle v_{th,n} \rangle \sum_i \sigma_{n,i} N_{T,i} \right]^{-1}. \quad 3.2$$

Returning to Eqn. 3.1, with electron trapping, the differential change in $N(t)$ with time is equal to $N(t)$ divided by τ_n which is a simple homogeneous first order ordinary differential equation with an exponential solution as shown below

$$N(t) = N_0 \exp\left(-\frac{t}{\tau_{n,p}}\right), \quad 3.2$$

where N_0 is the number of charge carriers generated. If τ_n is short compared to the transit time of carriers, all charge will effectively be lost without being collected. If τ_n is long, the device behaves almost like an ideal device. For example, in a planar detector with thickness d and a constant drift velocity, $E_w = 1/d$ allowing Eqn. 3.1 to be rewritten as

$$i(t) = \frac{eN_0v_d}{d} \exp\left(-\frac{t}{\tau_{n,p}}\right). \quad 3.3$$

Assuming the interaction depth x_i is measured relative to the cathode, the distance the hole travels will be x_i whereas the electron will travel a distance $d - x_i$. Therefore, the transit times t_r will be $x_i/v_{d,p}$ for holes and $(d - x_i)/v_{d,n}$ for electrons. After integrating with respect to time over the range $[0, t_r]$, the charge collected will be,

$$Q_p = \frac{eN_0v_{d,p}\tau_n}{d} \left[1 - \exp\left(-\frac{x_i}{\tau_p v_{d,p}}\right) \right], \quad 3.4$$

for holes and,

$$Q_n = \frac{eN_0v_{d,n}\tau_p}{d} \left[1 - \exp\left(-\frac{d - x_i}{\tau_n v_{d,n}}\right) \right], \quad 3.5$$

for electrons. Eqns. 3.4 and 3.5 are referred to as the Hecht equation [62] and illustrate how charge trapping reduces the amount of charge collected. Additionally, it shows that the relative contribution of electrons or holes to the total charge collected is related to their

transit distances. Since trapping is a statistical process, shorter trapping times will have wider peaks in the detector pulse height spectra. A schematic illustrating the difference in charge collection between the ideal case and in the case of trapping is shown in Figure 3.1.

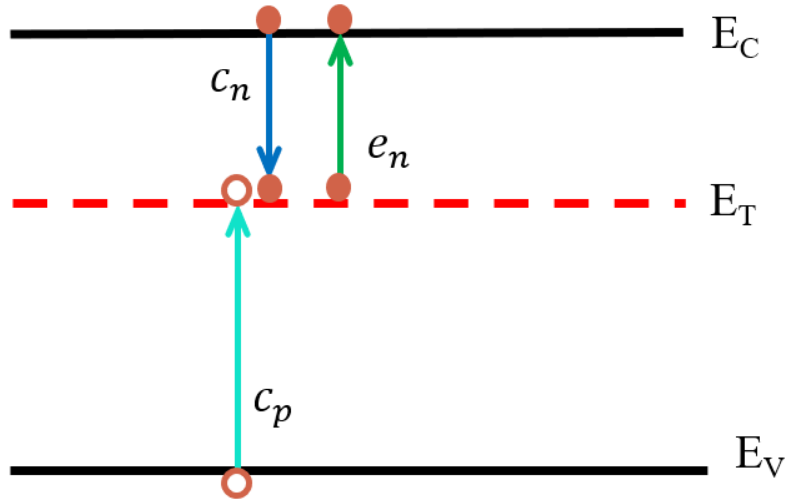


Figure 3.2 Band diagram displaying how a captured electron with capture rate c_n can either recombine with a captured hole c_p or emit back to the conduction band.

As illustrated in Figure 3.2, trapped charges are stuck in localized energy states within the bandgap where they will remain until they either recombine with free carriers of the opposite polarity or are able to thermally break free of the trap and return to their respective energy band. The former is extremely unlikely to occur for either carrier type in wide-bandgap SBDs because the recombination rate is proportional to the free carrier concentration of the opposite charge type [63, 64]. For example, in 4H-SiC the intrinsic carrier concentration is 10^{-9} cm^{-3} at room temperature. For n-type 4H-SiC doped at 10^{14} cm^{-3} , the hole concentration would be 10^{-32} cm^{-3} meaning that there is not a single hole in 10^{17} km^3 . If the entire earth was made of n-type 4H-SiC, there would not be a single free

hole to recombine with a trapped electron. For the other carrier, recombination is killed by the surface potential of the Schottky barrier effectively eliminating free majority carriers within the depletion width. Emission is related to the depth of trap level E_T from the respective band. For electrons, the emission rate e_n is described by the following

$$e_n = \sigma_n \langle v_{th,n} \rangle N_c \exp\left(-\frac{E_c - E_T}{k_B T}\right). \quad 3.6$$

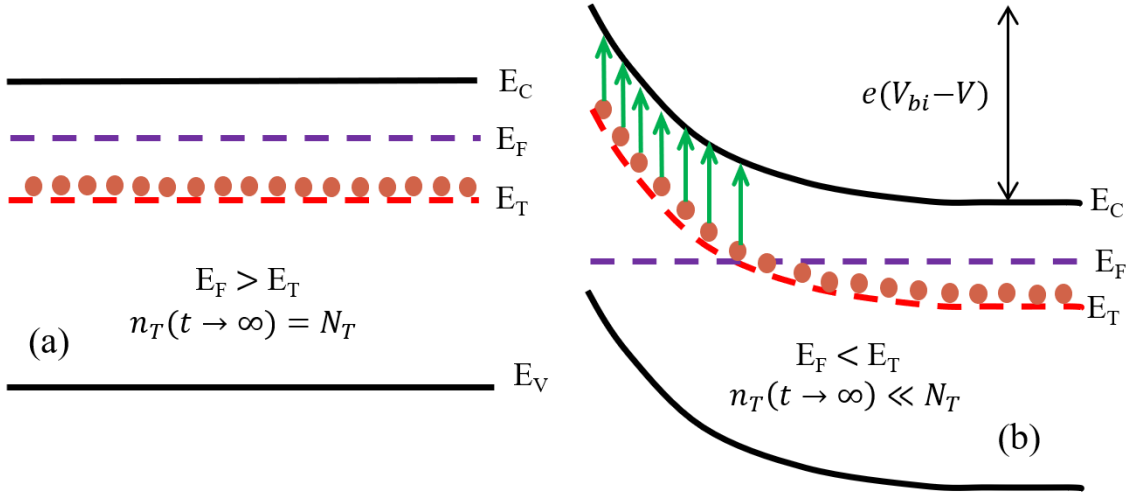


Figure 3.3 Band diagram displaying the steady-state occupation of trap levels (a) and the emission of traps in the space-charge region of SBDs under reverse bias (b). n_T is the concentration of occupied defect levels.

As demonstrated in Figure 3.3, before a bias is applied to an SBD, most of the device is in the neutral region and the fermi-energy level E_F will be greater than trap energy level E_T . Per Fermi-Dirac statistics [37, 65], the trap level will then essentially be fully occupied by electrons in most of the device and cannot trap new electrons (although it can trap holes). Upon applying a bias to the detector, the depletion width will expand and push the quasi-fermi level well below the trap level in most of the device's active region. At this

stage, the trap level will want to release its trapped electrons but is limited by the emission rate of the trap. If the emission time is very short (nanosecond or microsecond scale), then the carrier will quickly be returned to its respective band and be collected as if it was never trapped. If the emission time is on the scale of hours, days, or even years, then they will effectively be occupied forever and never contribute to trapping. The most significant trapping centers will be those with emission rates on the order of seconds or minutes which can fully emit before measurements start allowing them to act as trapping centers.

3.2 POINT DEFECTS IN 4H-SiC

Deep levels are derived from atomic level point defects in the crystal structure which can switch charge state—capture or lose electrons—depending on the position of the fermi-level relative to the trap level. The main types of point defects are vacancies, interstitials, antisites, and substitutions. Vacancies refer to the removal of an atom from its lattice site leaving behind an empty space. Vacancies are the most common defects in semiconductor materials due to their high chemical potential energy of atoms. Interstitials are atoms occupying in-between spaces in the crystal structure that are usually empty in the ideal crystal. They are unlikely to form by themselves in as-grown structures because the additional atom gives them a very low chemical potential. Both antisites and substitutions are the wrong atom occupying an atomic site. However, antisites involve native elements whereas substitutions are impurities. Impurities that only introduce shallow levels can be used to dope semiconductor crystals to be n-type or p-type. Defects can also form pairings such as vacancy-antisite complexes (adjacent atom moves into a vacancy), vacancy-interstitial complexes (vacant atoms moves to interstitial site),

divacancies (two adjacent atoms are removed), or diantisites (two atoms switch places). A schematic of the types of point defects in a simple zincblende lattice is given in Figure 3.4.

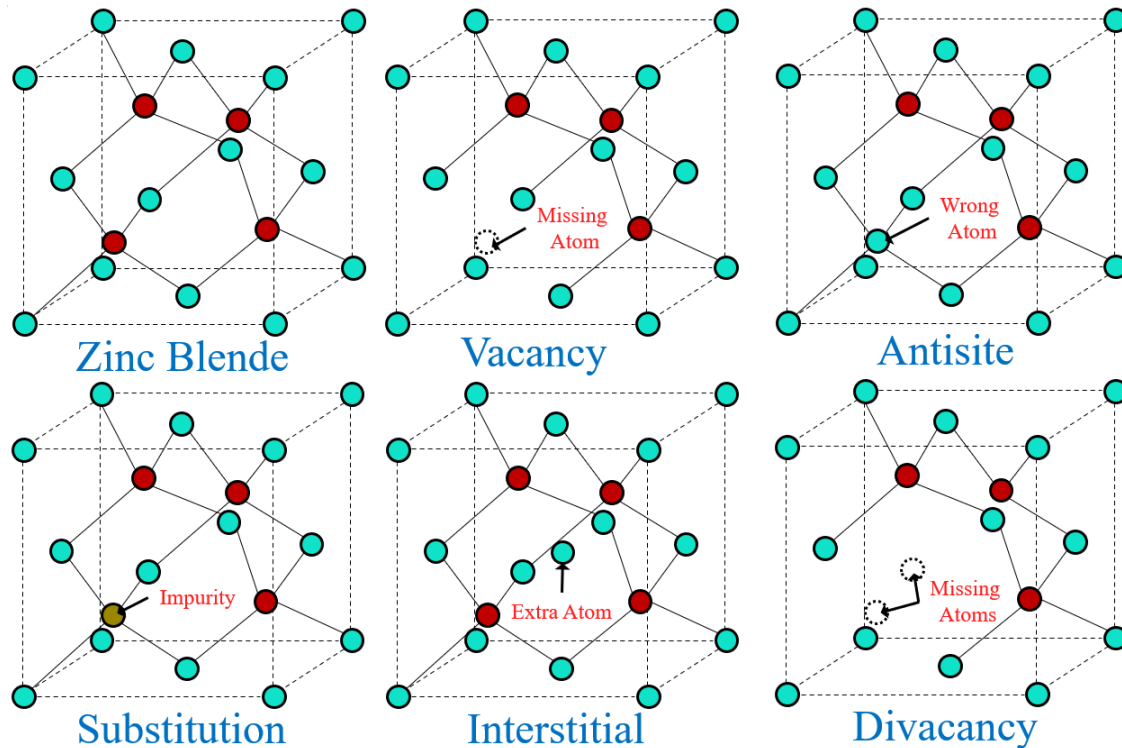


Figure 3.4 Crystal structure of a generic zinc blende lattice illustrating the various types of point defects that can occur in semiconductor crystals.

As shown in Figure 3.5, 4H-SiC has a hexagonal lattice with a four-part ABAC stacking structure [11]. By rotational symmetry, it has two nonequivalent carbon sites and two silicon sites which can be occupied by defects. The Si-C pairs repeated every A sequence are in the cubic or k-site because their repetition retains semi-cubic symmetry. The other Si-C pairs are in the hexagonal or h-site because they are repeated only once every sequence. Additionally, there are four nonequivalent interstitial sites positioned

above and below each stacked Si-C pair. The most important defect in 4H-SiC is the carbon vacancy which is known to form two deep levels in all as-grown epilayers [66-71].

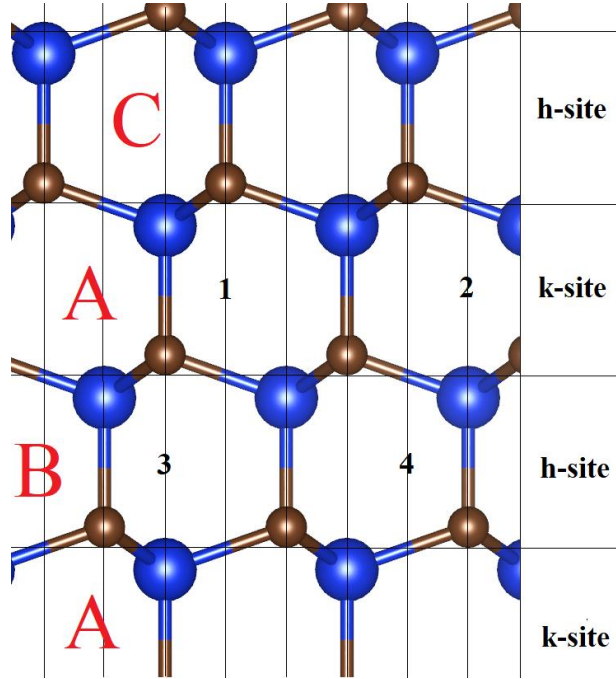


Figure 3.5 Stacking structure of 4H-SiC showing the various lattice sites which defects can occupy.

The probability of a defect forming is proportional to its formation energy defined as the additional energy needed to form a defective structure relative to the ideal structure and can be described locally by Eqn. 3.7 [72],

$$E_{D,q}^f = E_{D,q} - E_{ideal} - \sum_i n_i(\mu_i + E_i) + qE_F. \quad 3.7$$

Here, $E_{D,q}$ is the energy of the crystal with defect D at the integer charge state q , E_{ideal} is the energy of the perfect crystal structure, n_i is the number of atoms of species i removed (-) or added (+) from the crystal structure to make D , E_i is the energy per atom of the atomic species added or removed in its elemental state, μ_i is the atomic chemical potential which

largely depends on the chemical environment during growth, and E_F is the fermi energy level.

Energy calculations are usually conducted by first principles calculations based on density functional theory (DFT). The real multi-electron Schrodinger's equation cannot be solved using modern computational technology due to the sheer complexity the interactions between multiple electrons. DFT uses single electron pseudo-Schrödinger's equations called Kohn-Sham equations which give the same electron densities as the real Schrodinger's equation for a much lower computational cost [73, 74]. In general, Kohn-Sham equations are of the form,

$$\left[-\frac{\hbar^2}{2m} \nabla^2 + V(r) + V_H(r) + V_{XC}(r) \right] \phi_i(r) = \epsilon_i \phi_i \quad 3.8$$

where, \hbar is the reduced Planck's constant, $V(r)$ is the electron-nuclei interaction, $V_H(r)$ is the Hartree potential, $V_{XC}(r)$ is the exchange-correlation potential, ϕ_i is the wavefunction for noninteracting electron i , and ϵ_i is the eigenvalue or Kohn-Sham energy of the i^{th} electron. The only unknown parameter in this equation needed to solve for the eigenvalues is the exchange-correlation potential. DFT approximates it using density functionals which can result in highly accurate material properties, but usually inaccurate band structures and deep level positions. This can be amended using hybrid density functionals which use a portion of the real exchange-correlation potential to better correct for the self-interaction of electrons resulting in more accurate bandgaps. Another problem with DFT calculations is the projected augmented wave (PAW) method [75] used by most DFT simulation packages periodically images the input structure. As a result, defects will be spaced too close together compared to real materials and will coulombically interact with each other,

altering the total energy [76]. Accuracy can be improved by using larger supercells [77] or by introducing a correction factor E_{corr} to Eqn. 3.7—usually both.

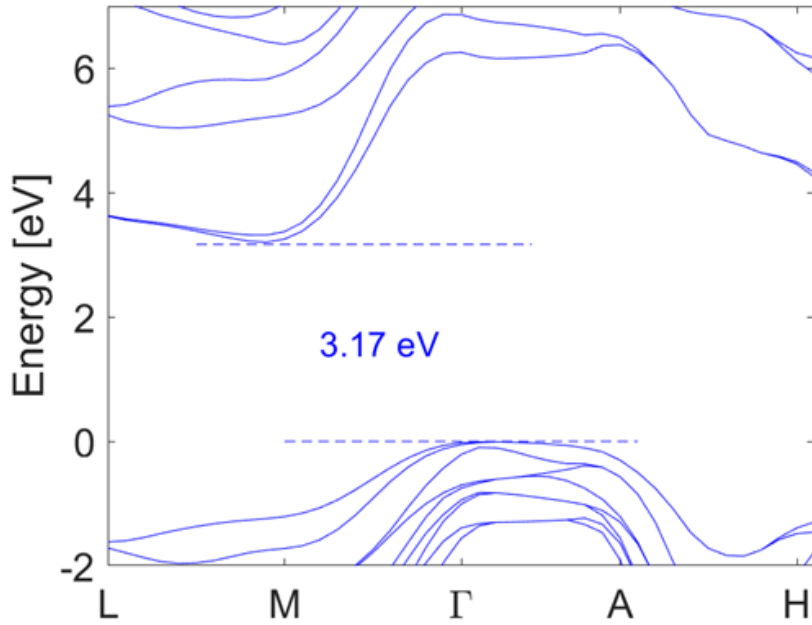


Figure 3.6 Band structure of 4H-SiC calculated using HSE06 pseudopotentials. The x-axis is the k- or reciprocal space projection of periodic lattice structure. The labels refer to the high symmetry points of the first Brillouin zone of a simply hexagonal lattice [73].

To study the major deep levels in as-grown 4H-SiC, the formation energies of silicon and carbon vacancies in 4H-SiC as a function of the fermi energy taken over bandgap of 4H-SiC were calculated by the PAW method implemented in the Vienna ab initio software package (VASP). These calculations were performed on a 3 x 3 x 1 supercell (72 atoms) using HSE06 pseudopotentials [78, 79] with a Γ -centered 2 x 2 x 2 Monkurst-Pack grid and an energy cutoff of 520 eV. The Heyd-Scuseria-Ernzerhof functional (HSE) is a hybrid density functional which mixes the short and long range components of the Perdew-Burke-Ernzerhof generalized (PBE) gradient approximation (GGA)

pseudopotential [80] with a portion of the short-range component of the full exchange-correlation potential [78]. HSE06 is the 2006 variation of the hybrid functional [79, 81] which provides accurate bandgaps and solves the generalized Koopman's theory for Group IV semiconductors and thus should produce transition levels which accurately match deep levels observed in real materials [82].

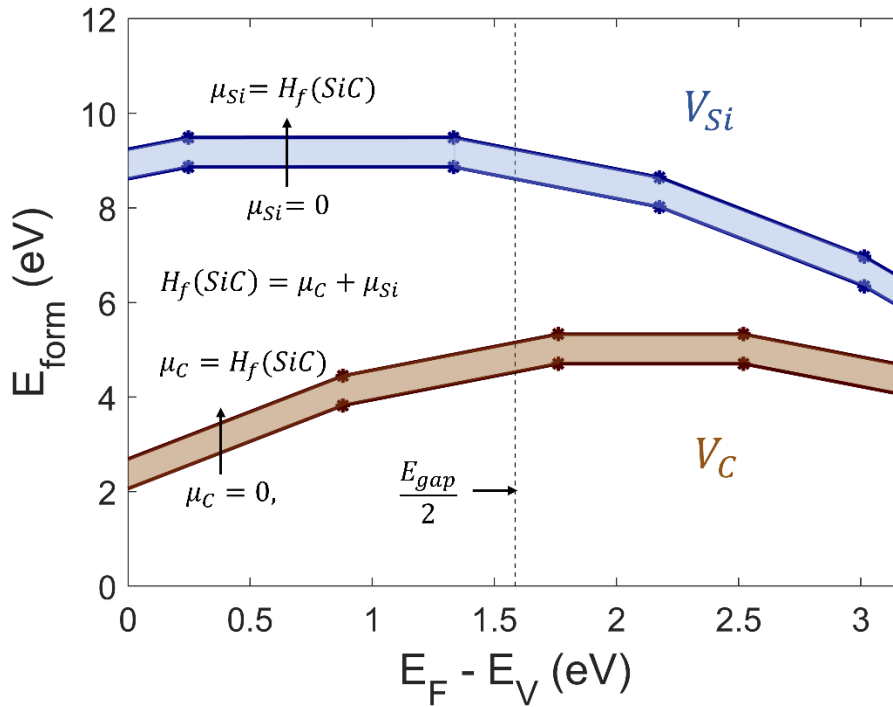


Figure 3.7 Formation energies as a function of the Fermi-level for carbon and silicon vacancies in 4H-SiC calculated using HSE06 pseudopotentials.

For 4H-SiC to exist in the 4H-SiC chemical phase, the chemical potentials of silicon μ_{Si} and carbon μ_C are required to sum to twice the heat of formation of 4H-SiC [83]. The heat of formation is defined as the energy difference/atom between 4H-SiC and its elemental constituents in the elemental state which was calculated to be -0.31 eV/atom. A

value of $\mu_C = 0$ refers to carbon rich conditions loosely corresponding to a high C/Si ratio whereas $\mu_{Si} = 0$ is roughly equivalent to a low C/Si ratio.

The Fermi-energy level is treated as an independent variable ranging over the bandgap of the material and is meant to reflect different doping conditions. At 0 K, the fermi-level would simply be equal to the valence band maximum. To find the bandgap, the energy levels of the eight-atom unit cell were computed over linearly spaced k-points along the high symmetry lines. As shown in Figure 3.6, 4H-SiC is an indirect bandgap semiconductor with the valence band maximum located at the Γ -point and the conduction band minimum at the M point in k-space. The energy gap between these two points was 3.17 eV which is close to the experimental bandgap and agrees with what has been reported elsewhere [84, 85]. The correction factors were calculated using the extended Freysoldt-Neugebauer-Van de Walle (FNV) correction by Kumagai *et al.* which gives better energy correction for hexagonal structures than the original FNV correction [76, 86].

For each charge state, the formation energy is plotted against the fermi energy level creating a series of formation energy lines. The intersections of these the lines are called transition levels and mark the energy level where a defect will prefer to switch charge state directly corresponding to deep levels in real materials. As defects will always prefer to occupy the lowest energetic state, only the minimum formation energies are needed to explain charge state switching in materials. The minimum formation energy as a function of fermi energy level is presented in Figure 3.7 which acts as the charge state phase diagram for the defects. The present calculation shows four defects derived from silicon vacancies (two electron and two hole) and three carbon vacancy related defects which are recorded in Table 3.1. It should be noted that silicon vacancies have high formation energies at the

midgap (> 8 eV) which makes them unlikely to appear in as-grown epilayers. The trap concentration is related to the formation energies at the midgap by the following Boltzmann relation [87],

$$N_T = N_s \exp\left(-\frac{E^f}{k_B T}\right) \quad 3.9$$

Carbon vacancies have formation energies between 4 and 5 eV depending on the growth conditions which can correspond to easily observable concentration $\sim 10^{11}$ - 10^{13} cm $^{-3}$.

Table 3.1 Vacancy transition levels computed with HSE06 pseudopotentials. The energy levels are measured from the valence band maximum and given in eV.

Defect	(+2 +1)	(+1 0)	(0 -1)	(-1 -2)	(-2 -3)
V _{Si}		0.25	1.33	2.18	3.01
V _C	0.88	1.76	2.52		
V _C ^a	1.7	2.0	2.5		
V _C (k) ^b	1.74	1.96	2.58	3.10	
V _C (h) ^b	1.65	2.03	2.47		

^aGorden *et al.* [88].

^bKobayashi *et al.* [84].

As mentioned, the phase diagram predicts the formation of three carbon vacancy deep levels in as-grown 4H-SiC. The (+2|+1) transition 0.88 eV above the valence band maximum will act as a hole trapping center and possibly correlates to the lifetime limiting HK2 defect in as-grown p-type 4H-SiC which has acceptor-like characteristics and is thermally stable up to 1550 °C [89, 90]. The other defects, 1.76 eV (+1|0) and 2.52 eV (0|-1) above the valence band, are electron trapping centers. The former likely corresponds to EH_{6/7} which is well established as carbon vacancy related and the later to Z_{1/2} which is considered the most important lifetime limiting defect in 4H-SiC radiation detectors [68-

70, 91-93]. In comparison with previous work, the (0|-1) transition approximately occupies the same position as the others have reported. Both Gordon *et al.* and Kobayashi *et al.* have reported the (+2|+1) transition as closer to 1.7 eV whereas the (+1|0) transition is positioned at 2.0 eV [86, 88]. A possible explanation for the discrepancies is possibly the energy cutoff used, the lattice constants, the supercell size, or the chosen k-mesh. This essentially predicts three electron traps originating from carbon vacancies which could be $Z_{1/2}$ and the split peaks of $EH_{6/7}$. However, Laplace DLTS studies on $EH_{6/7}$ suggest that only EH_7 corresponds to carbon vacancies and EPR studies show that its charge transition state is (+1|0) [70].

The capture cross-section is more difficult to exactly calculate with density functional theory. However, because trapping is in-part a coulombic effect, defects with a more positive charge state will be able to pull in electrons from a further distance increasing their capture cross-section relative to neutral defects. Likewise, more negatively charge defects will want to push electrons away, thus, shrinking the capture cross-section. In 4H-SiC, the capture cross-sections of neutrally charged $Z_{1/2}$ is $\sim 10^{-15}$ cm² whereas the positively charged $EH_{6/7}$ can be 10^{-15} - 10^{-14} cm².

3.3 MINORITY CARRIER DIFFUSION LENGTH MEASUREMENTS

To study the effect of both minority and majority carrier trapping on the radiation detection performance of Ni/4H-SiC SBD radiation detectors, detectors were fabricated on 4H-SiC epilayers of 50, 150, and 250 μ m thickness. In this section, the detectors are characterized electrically and via their radiation detection performance with an ²⁴¹Am alpha particles. The impact of minority carrier trapping, evaluated from the bias dependence of

the radiation detection response, will be discussed this section and that of majority carrier trapping will be discussed in Sec. 3.5. The device fabrication and experimental methods are the same as described in Chapter 2.

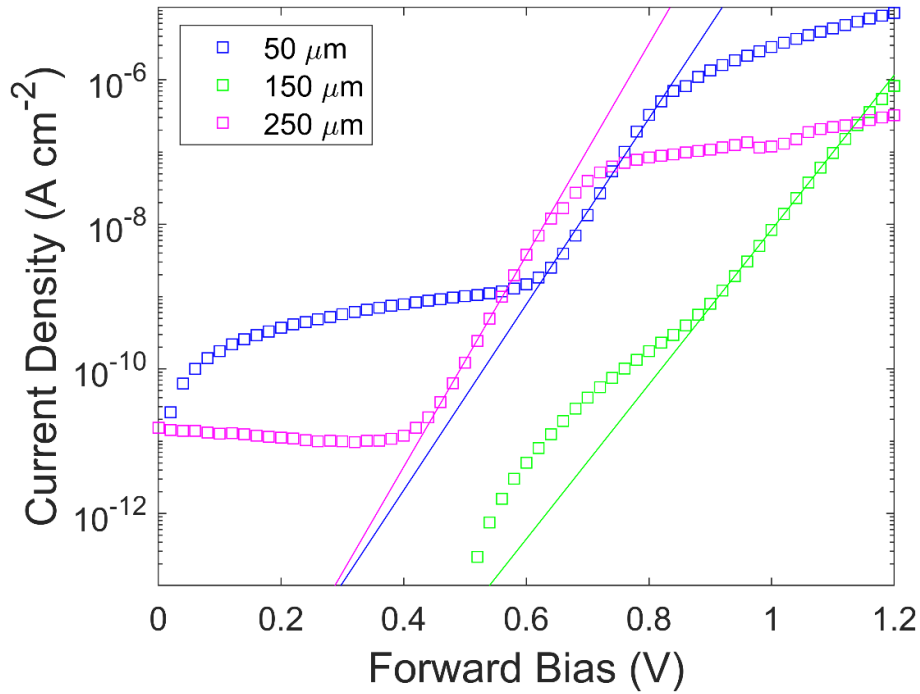


Figure 3.8 Forward bias current-voltage characteristics for the detectors fabricated on the 50, 150, and 250 μm epitaxial layers. The solid lines represent the fit to the linear region.

The forward and reverse bias I-V characteristics of the three detectors are given in Figures 3.8 and 3.9 showing that all three detectors are SBDs. From the thermionic emission model (Sec. 2.1), the barrier heights were calculated to be 1.43, 1.55, and 1.46 eV and the ideality factors, 1.30, 1.56, and 1.14 for the detectors fabricated on 50, 150, and 250 μm epilayers, respectively. Of the detectors, 150 μm had largest effective barrier height, but also the highest ideality factor indicating that it has the most substantial spatial variation in the barrier height. Because the Schottky contact serves as the window for

radiation detection, larger contacts can help increase the detection efficiency for a larger gap between the source and detector. However, as the contact area increases, so does the probability of spatial variation in the surface barrier resulting in high ideality factors and low barrier patches [49, 94]. The leakage current densities for the 50 and 150 μm detectors remained under 1 nA/cm^2 up to -100 V [78 kV/cm] whereas the 250 μm could retain this such low currents up until -800 V [280 kV/cm]. The higher current in the first two samples could be derived from a shunting pathway which is evident from the portion of the forward bias characteristics to the left of the linear region for the 50 and 150 μm detectors [95, 96].

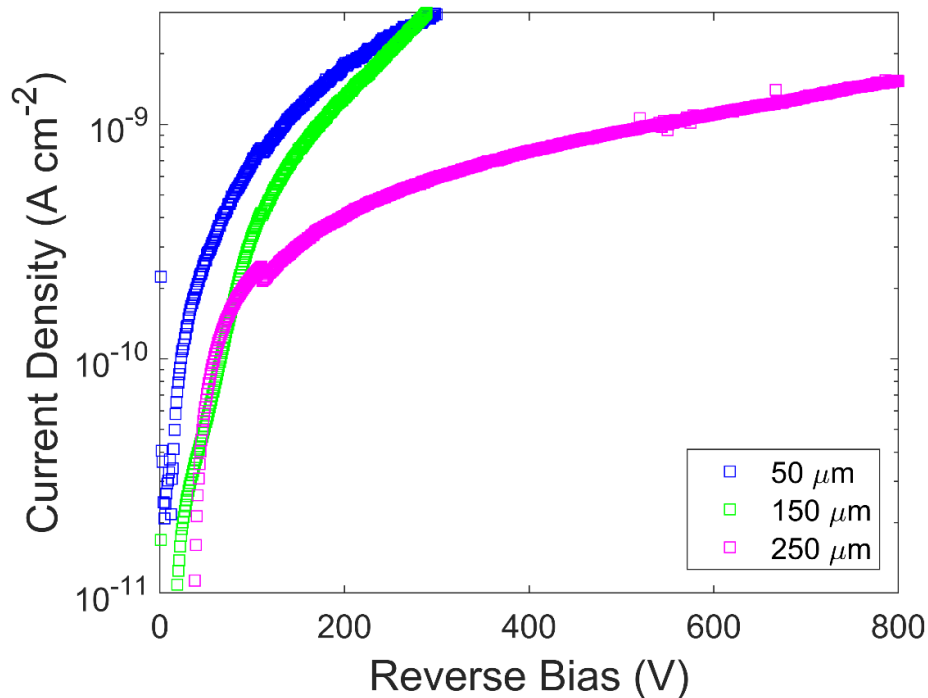


Figure 3.9 Reverse bias current-voltage characteristics for the detectors fabricated on the 50, 150, and 250 μm epitaxial layers.

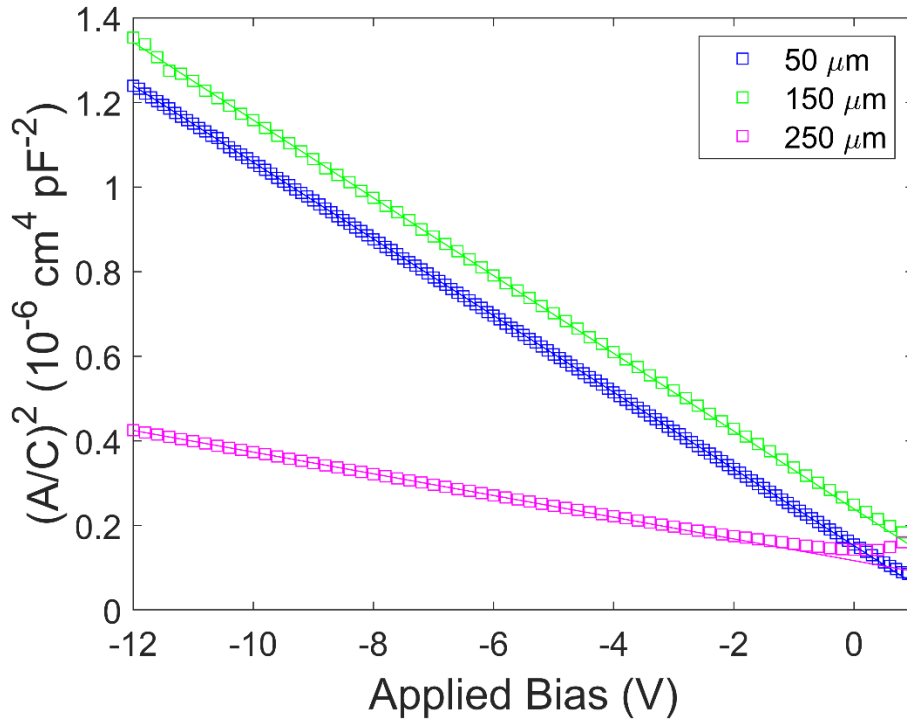


Figure 3.10 Mott-Schottky plot of detectors fabricated on the 50, 150, and 250 μm epitaxial layers. The solid lines are the linear fits.

The net donor concentrations were determined from the Mott-Schottky plots of the detectors (Figure 3.10) to be between 1.6 and $1.8 \times 10^{14} \text{ cm}^{-3}$ for all three detectors. The 50 μm detector had a built-in voltage of 1.68 V corresponding to an average barrier height of 1.98 eV. The 150 and 250 μm had high built-in voltages making the average barrier unable to be determined by C-V. Using Eqn. 2.6, it was estimated that the detectors will be fully depleted at 380 V [150 kV/cm], 3.3 kV [450 kV/cm], and 10 kV [810 kV/cm] for the detectors fabricated on 50, 150, and 250 μm epilayers, respectively.

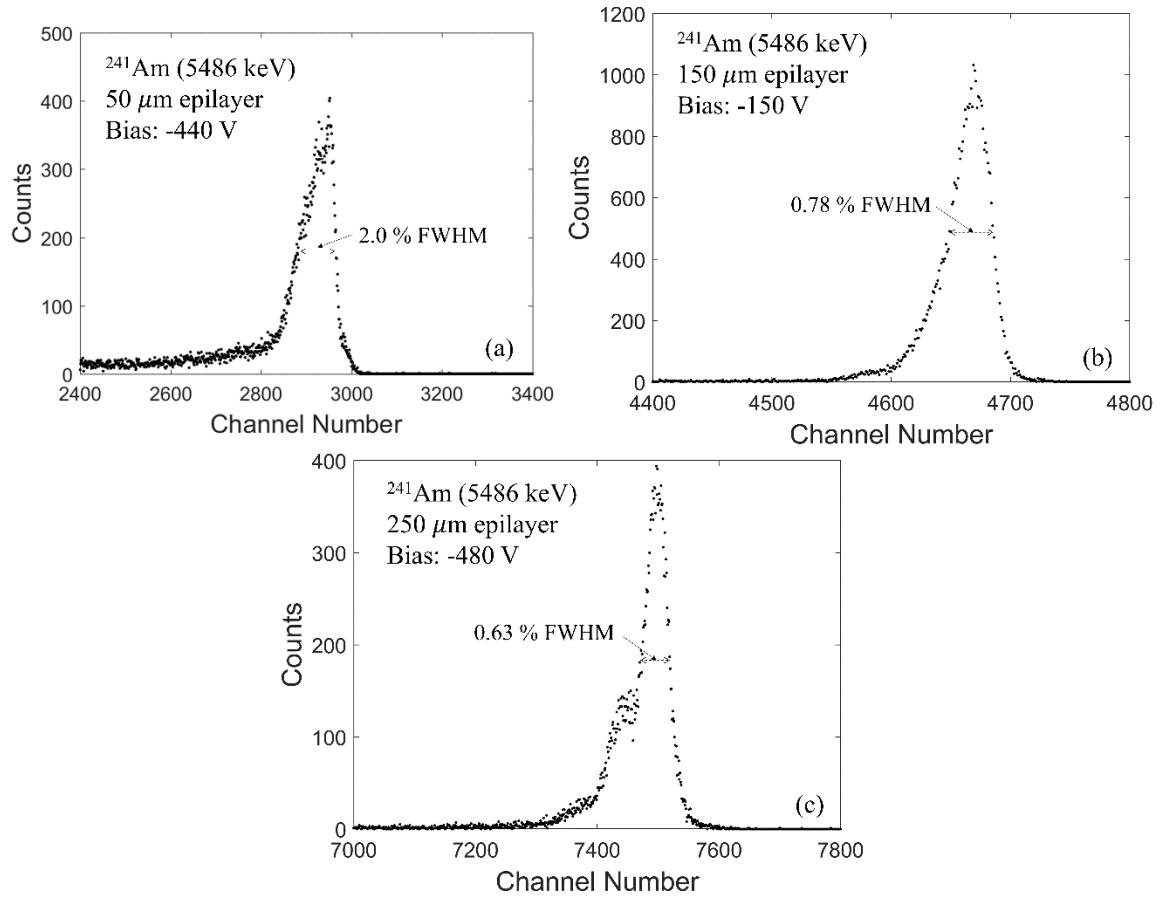


Figure 3.11 Pulse height spectra at the bias which gave the best resolution for the detectors fabricated on 50 (a), 150 (b), and 250(c) μm 4H-SiC epitaxial layers.

Table 3.2 Detector parameters obtained for detectors fabricated on 50, 150, and 250 μm epitaxial layers.

Epilayer Thickness (μm)	n	Φ_B (eV)	N_{eff} (10^{14} cm^{-3})	Energy Resolution (%)	L_d (μm)
50	1.30	1.43	1.61	2.0	16
150	1.56	1.55	1.59	0.78	10
250	1.14	1.46	1.74	0.63	9.2

Figures 3.11 give the best resolution spectrum for each of the detectors whereas Table 3.2 shows the detector parameters for each device. The detectors coincidentally had

resolutions of 2.0%, 0.78%, and 0.63% in increasing order of epilayer thickness. Because the detectors were not fully depleted, thickness cannot be considered a strong predictor of detector optimal resolution. Additionally, better ^{241}Am alpha spectra has been observed in unpassivated 20 μm detectors than in any of the three detectors present [20, 50]. The detectors have similar capacitances to the detectors discussed in Chapter 2 and therefore the electronic noise should be negligible. The most likely explanation for the observed peak broadening is trapping by deep levels within the epilayers.

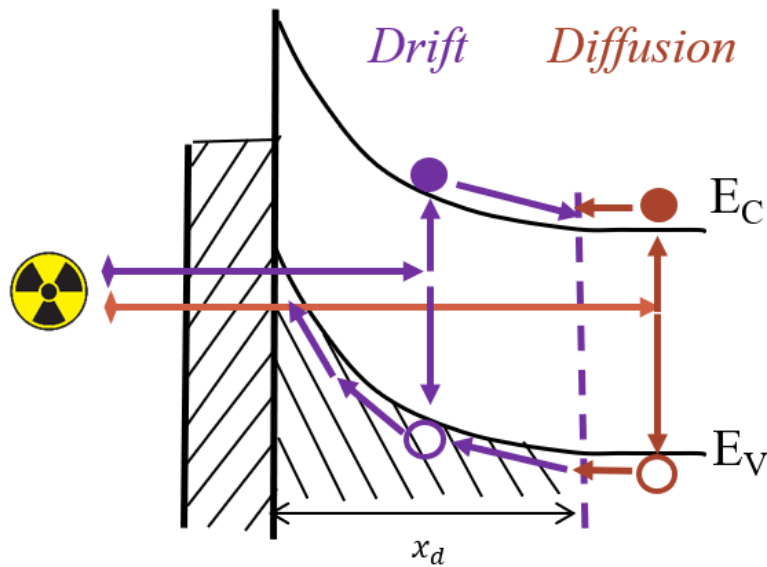


Figure 3.12 Illustration of the drift-diffusion model for charge collection.

For charged particles, the incident radiation generates a continuum of charges over the entire path of the particle which makes the Hecht equation inadequate for characterizing the trapping lifetimes of detectors. Furthermore, in 4H-SiC SBDs, the internal electric field is strong enough that most carriers would immediately be accelerated to saturation drift velocity making the charge collected nearly independent of the applied bias, assuming all

carriers are generated within the space-charge region. Another approach is to consider the collection of charge generated outside the active region. Per the drift diffusion model illustrated in Figure 3.12 [97], charges generated in the space-charge region will immediately drift towards their respective electrodes producing a current. Charge pairs generated in the neutral region can only be collected if they first diffuse into the space-charge region at which point holes will be swept up by the electric field. The total induced charge can then be described by,

$$Q = \int_0^{x_d} \left(\frac{dQ}{dx} \right) dx + \int_{x_d}^{x_r} \left(\frac{dQ}{dx} \right) \exp\left(-\frac{x - x_d}{L_d}\right) dx. \quad 3.9$$

Here, dQ/dx is the differential charge generated per unit length or Bragg curve, x_r is the range of the alpha particles (18.22 μm in 4H-SiC), and L_d is the ambipolar diffusion length. L_d is reciprocally the sum of both the majority and minority carrier diffusion length which are related to the square roots of their individual trapping times in the neutral region. However, because 4H-SiC has significantly worse hole transport properties than electron properties and most trapping centers should be filled with electrons, L_d is practically the minority carrier diffusion length and can be used to quantify the hole trapping properties of the detectors.

Figure 3.13 shows the charge collected as a function of the applied reverse bias for each detector and the simulated models with the numerical optimized values of L_d . Using an initial value of 20 μm for L_d , the normalized charge collected was computed numerically for $x \in [0, x_r]$ using a step size of 0.01 μm . The simulated charge collected was then compared to the experimental charge collected versus bias data via the mean absolute percent error. If the mean absolute error was above the convergence threshold of 0.1%, then the value of L_d was adjusted by $\pm 0.1 \mu\text{m}$ depending on the sign of the mean error. The

process was repeated procedurally until the convergence condition was reached or the number of iterations exceeded 1000 indicating that a local minimum had been reached.

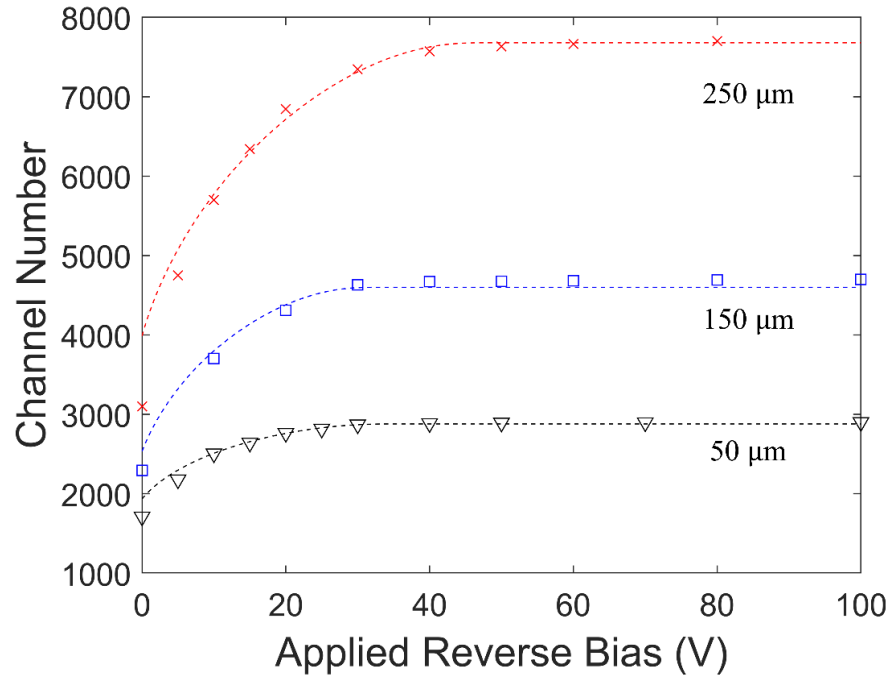


Figure 3.13 Charge collected as a function of the applied reverse bias given in channel number to clearly distinguish among the three curves. The dashed lines are the fit to the drift-diffusion model.

The minority carrier diffusion lengths were found to be 16, 10, and 9.2 μm for the 50, 150, and 250 μm detectors, respectively, implying that the resolution is not limited by hole trapping. As shown in Figure 3.14, the Bragg curve is a back-heavy function leading most electron-hole pairs to be generated towards the end of the particle's path. For this reason, the transit distance for holes initially is much longer on average than the transit distance for electrons, and therefore, holes contribute more to the total charge collected. As the depletion width expands, eventually the electron transit distance will exceed the

hole transit distance making the detector limited predominantly by majority carrier trapping.

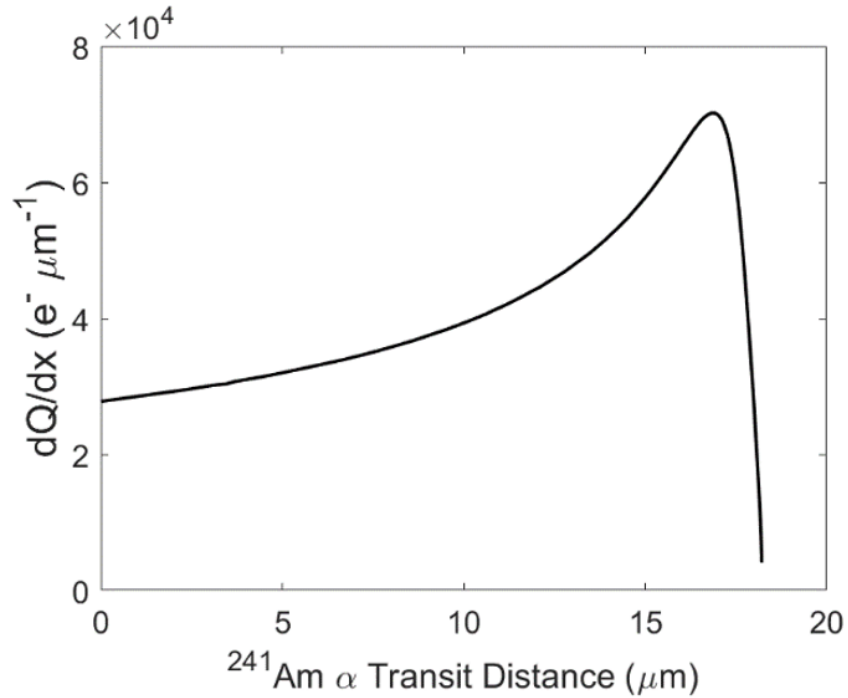


Figure 3.14 Bragg curve for 5486 keV alpha particles interacting with 4H-SiC.

3.4 DEEP LEVEL TRANSIENT SPECTROSCOPY BACKGROUND

The majority carrier trapping parameters of the detector were characterized by deep level transient spectroscopy (DLTS). DLTS is a powerful technique developed by D. V. Lang at Bell Laboratories that uses capacitance transients to characterize the concentrations, cross-sections, and energy levels of deep levels in rectifying diodes. More information on DLTS theory can be found in Ref. [98].

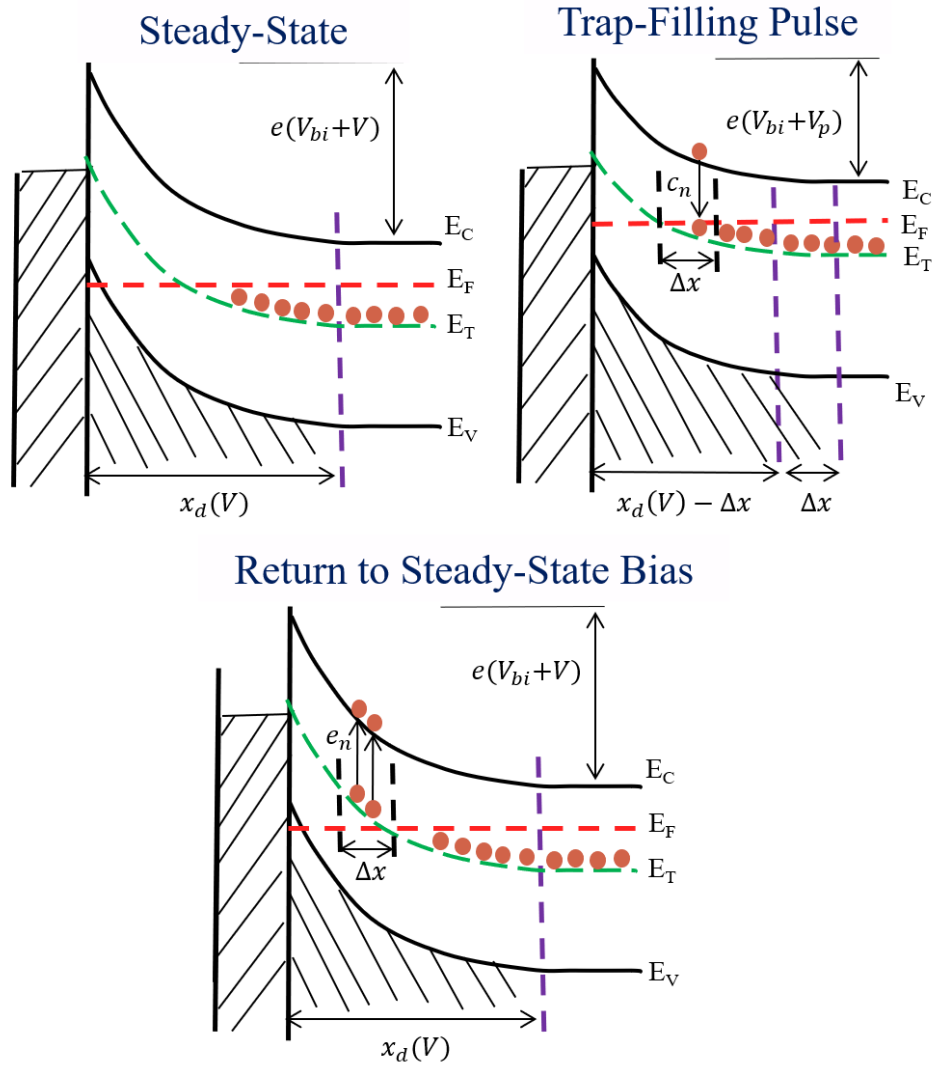


Figure 3.15 Band diagrams of a Schottky detector with a trap level E_T demonstrating the trapping and de-trapping with periodic biasing.

As illustrated in Sec. 3.2, deep levels prefer to be occupied by electrons when the fermi-energy level is above the trap level and prefer to be unoccupied when the fermi-energy level is below the trap level. In SBDs, energy bands are bent by the surface potential whereas the semiconductor quasi-fermi level is constant throughout the device. This leads to deep levels closer to the metal preferring to be unoccupied whereas defects closer to the neutral region will prefer to be empty. As demonstrated in Figure 3.15, reducing the reverse

bias will push the fermi level above the trap level allowing trap states within a region Δx to fill with electrons reducing the net charge of the depletion region. Upon returning to the steady-state bias, the traps within Δx will start to emit back to the conduction band creating a transient in the net charge. During this time, capacitance will be described by the difference between the net donor concentration and the occupied trap concentration as shown below,

$$C(V, t) = A \sqrt{\frac{e\epsilon(N_{eff} - n_T(t))}{2(V_{bi} - V)}}. \quad 3.10$$

Here, $n_T(t)$ is the concentration of occupied traps defined in terms of the electron emission rate as,

$$n_T = N_T \exp(-e_n t). \quad 3.11$$

As it is written, Eqn. 3.10 can be expressed as the square root of two capacitances squared,

$$C(V, t) = \sqrt{C_{ss}^2(V) - C_T^2(t)}, \quad 3.12$$

where the first term is the ideal steady-state capacitance,

$$C_{ss}(V) = A \sqrt{\frac{e\epsilon N_{eff}}{2(V_{bi} - V)}}, \quad 3.13$$

and the second term is what the capacitance would be if the trap concentration was the net donor concentration,

$$C_T = A \sqrt{\frac{e\epsilon_{eff} n_T(t)}{2(V_{bi} - V)}}. \quad 3.14$$

Taking the Taylor series expansion of \sqrt{x} evaluated at $C_{ss}^2(V) - C_T^2(t)$ about the point $x_0 = C_{ss}^2(V)$ allows Eqn. 3.12 to be written as the following series expression,

$$C(V, t) = C_{ss}(V) - \frac{1C_T^2(t)}{2C_{ss}(V)} + \frac{C_T^4}{8C_{ss}^3(V)} + \dots \quad 3.15$$

If $N_{eff} \gg N_T$, then all terms after the first two terms are approximately zero and can be neglected which leads to the classic equation for the capacitance transient

$$C(V, t) = C_{ss}(V) + \Delta C \exp(-e_n t), \quad 3.16$$

where ΔC is the maximum change in capacitance observed due to trapping. Knowing ΔC , the trap concentration can be calculated using the second term of the Taylor polynomial

$$\frac{\Delta C}{C_{ss}(V)} = \frac{N_T}{2N_{eff}}. \quad 3.17$$

Real materials have multiple trap levels which all contribute to the change in capacitance which transforms Eqn. 3.16 into a summation of multiple exponential terms corresponding to individual trap level making direct exponential fitting nearly impossible. To surmount this, D. V. Lang developed a method known as the double boxcar method which instead uses the capacitance difference spectrum with two measuring times t_1 and t_2 to characterize the trap levels such that for a single trap,

$$C(t_1) - C(t_2) = \Delta C [\exp(-e_n t_1) - \exp(-e_n t_2)]. \quad 3.18$$

For multiple traps, the DLTS signal would be the superposition of their individual DLTS signals.

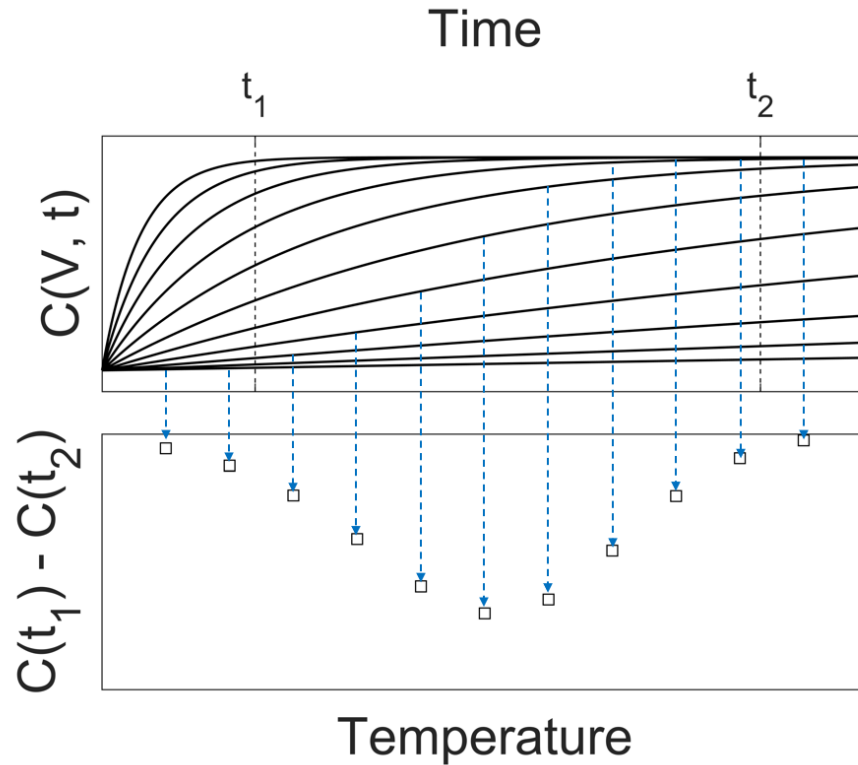


Figure 3.16 Demonstration of the capacitance transient and the formation of the DLTS signal.

As illustrated in Figure 3.16, at low temperatures, the emission rate is extremely slow (inactive) and the difference in capacitance will essentially be zero because the waveform does not decay. As temperature increases, the emission rate will speed up increasing the difference in capacitance between t_1 and t_2 until reaching some maximum value. At that point, the difference will fall off towards zero again as the waveform will essentially be fully decayed before t_1 is even reached (fully active). For sufficiently spaced-out deep levels (energy wise), there will be little overlap between the DLTS signals of multiple traps because when one is active, the others will be either fully inactive or fully active. The emission rate corresponding to the peaks in the DLTS spectrum can be acquired

by setting the derivative of $C(t_1) - C(t_2)$ to zero and solving for e_n leading to the result below,

$$e_{n,peak} = \frac{\ln\left(\frac{t_2}{t_1}\right)}{t_2 - t_1}, \quad 3.18$$

which is independent of temperature and only depends on the chosen values of t_1 and t_2 . Therefore, for any peak centered at any temperature, its corresponding emission rate will be known. Thus, using several measuring times will allow for the collection of multiple T - e_n pairs which will have the following linear relationship derived from Eqn. 3.6,

$$\ln\left(\frac{e_n}{T^2}\right) = \ln(\sigma_n \beta) - \frac{E_c - E_T}{k_B T}. \quad 3.18$$

Here, β is a constant equal to $\langle v_{th,n} \rangle N_C / T^2$ (approximately $3.4 \times 10^{21} \text{ cm}^{-2} \text{ s}^{-1}$ in 4H-SiC). From the linear fitting of the T - e_n pairs to Eqn. 3.18, both $E_c - E_T$ and σ_n can be acquired for an individual trap. Additionally, the value of $[C(t_1) - C(t_2)]/\Delta C$ will be constant at the peaks for select t_1 and t_2 allowing the trap concentration to be extracted from the magnitude of the peaks.

3.5 DLTS ON 4H-SiC RADIATION DETECTORS

DLTS studies were performed on the detectors fabricated on 50, 150, and 250 μm 4H-SiC epitaxial layers using a SULA DDS-12 DLTS system consisting of a 1 MHz capacitance meter, a pulse generator that can output up to ± 12 V with a pulse width as small as 2 μs , a preamplifier module with signal gains ranging from one to three hundred, a correlator module for selection of the initial measuring time t_1 , and an NI digitizing card for fast data acquisition interfaced with a LabVIEW based data acquisition software. The correlator module can collect up to four DLTS spectra simultaneously with initial delays

ranging from 0.02-100 ms predetermined by the DLTS system. The second measuring time t_2 is defined internally as $5.3 \times t_1$ which ensures that all spectra have the same normalization. The samples were mounted onto the sample stage of a Janis VPF 800 LN₂ cryostat consisting of a gold backing plate and sharp tungsten probes for connection to the top circular contacts. The pulse generator and capacitance meter were connected to the cryostat through BNC cables passed through to the sample stage through copper wires wrapped in thermal sleeves. The temperature within the cryostat was controlled using a Lakeshore LS335 temperature controller interfaced with the SULA DLTS's LabVIEW data acquisition software. A typical DLTS scan ranges from 80-790 K which allows for the extraction of a broad range of deep levels from 0.15-1.8 eV below E_c .

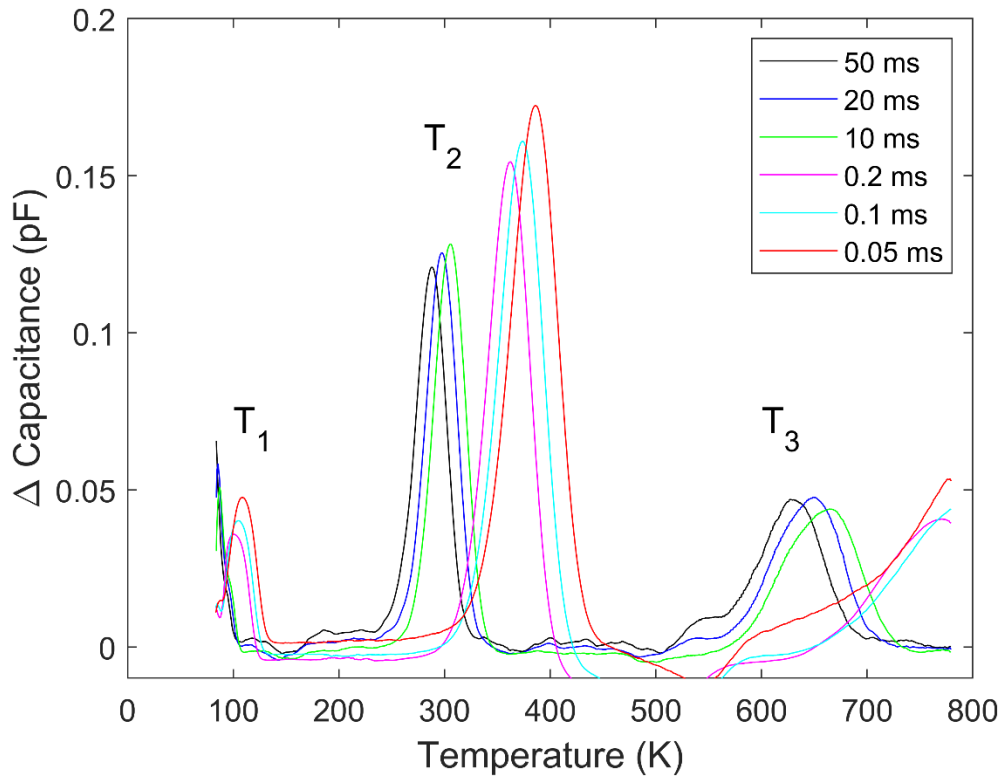


Figure 3.17 DLTS spectrum of a typical high quality as-grown 4H-SiC epitaxial layer radiation detector.

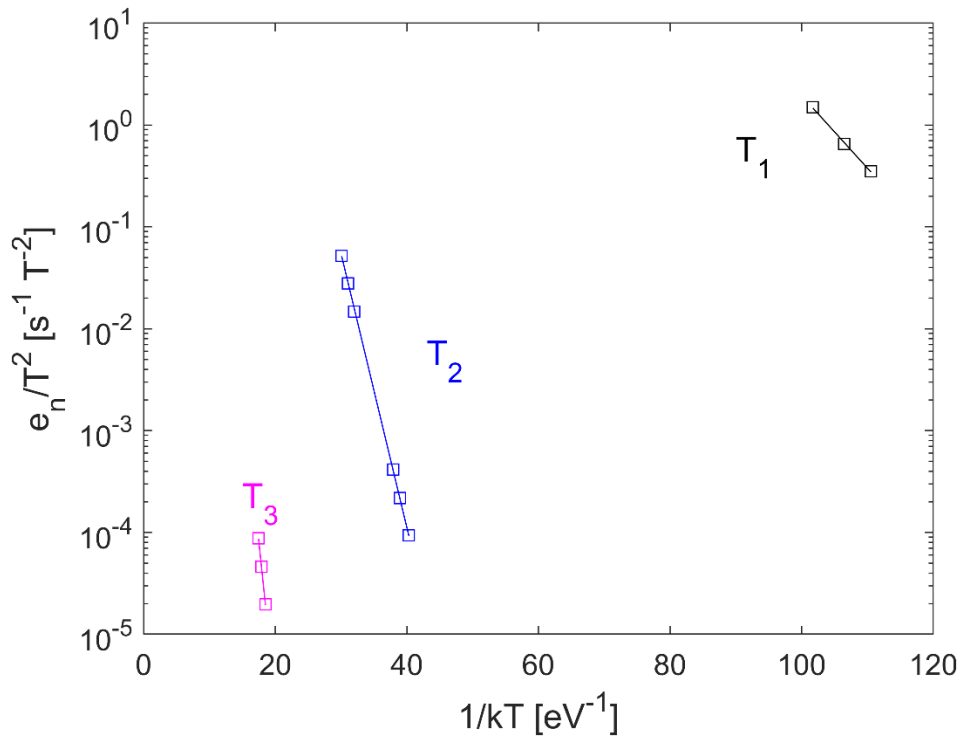


Figure 3.18 Arrhenius plot of the spectrum shown in Figure 3.17.

To demonstrate what typical DLTS spectrums of 4H-SiC SBD radiation detectors look like, Figure 3.17 shows the full DLTS spectrum of one of the UofSC’s 250 μm Ni/4H-SiC SBDs, displaying three peaks which appear in all as-grown samples. Figure 3.18 displays its corresponding Arrhenius plot. This specific spectrum was acquired using a -2 V steady-state bias and a 1 μs , 0 V filling pulse over the full temperature range. The first peak with an energy level 0.16 eV below the conduction band edge corresponds to titanium impurities from the wall of the growth chamber occupying cubic silicon sites [99]. At room temperature, the average emission time can vary from 1-100 ns depending on the cross-section and exact activation energy. This is fast enough to not significantly impact the detector resolution at room temperature but can affect the optimal shaping time. The second peak at 0.62 eV and third peak at 1.43 eV corresponds to the key lifetime limiting defects

$Z_{1/2}$ and $\text{EH}_{6/7}$, respectively, which have already been discussed thoroughly in Sec. 3.2. $Z_{1/2}$ operates on a timescale of second and millisecond making it the most substantial trapping center at room temperature. $\text{EH}_{6/7}$ has a time scale of years. Since measurements always start at zero bias, $\text{EH}_{6/7}$ will always be full even if the quasi-Fermi level is pushed below it by a reverse bias making it benign as an electron trap at room temperature.

Table 3.3 Comparison of defect parameters obtained from DLTS results on 50, 150, and 250 μm epilayers.

Thickness (μm)	$Z_{1/2}$			$\text{EH}_{6/7}$		
	N_t (10^{11} cm^{-3})	σ_n (10^{-15} cm^2)	$E_c - E_T$ (eV)	N_t (10^{11} cm^{-3})	σ_n (10^{-15} cm^2)	$E_c - E_T$ (eV)
50	23	130	0.73	1.8	19	1.59
150	8.6	1.4	0.60	2.6	38	1.63
250	5.3	0.26	0.56	5.3	3.2	1.49

DLTS spectra were acquired for the three detectors fabricated on 50, 150, and 250 μm epilayers at a steady-state bias of -5 V and a 0 V, 1 msec trap filling pulse. The temperature was varied from 200-790 K which is sufficient to capture the $Z_{1/2}$ peak for all initial delays and the $\text{EH}_{6/7}$ peak using the highest set. Figure 3.19 shows the zoomed in $Z_{1/2}$ and $\text{EH}_{6/7}$ peaks for the detectors, and their extracted trapping properties are recorded in Table 3.2. Per Eqn. 3.2, the mean trapping time is related to the reciprocal of the sum of products between N_T and σ_n implying that detectors with larger products should have more significant peak broadening. The individual trapping time for $Z_{1/2}$ was calculated to be 180 ns for the 50 μm detector compared to 44 and 380 μs for the 150 and 250 μm detector, clearly demonstrating why the 50 μm detector had the worst resolution of the three. For $\text{EH}_{6/7}$ the trapping times were 15, 5, and 3 μs for 50, 150, and 250 μm , respectively. Overall,

the increasing trend for the lifetimes of both $Z_{1/2}$ and $EH_{6/7}$ agreed with the improvement observed in the detector resolution.

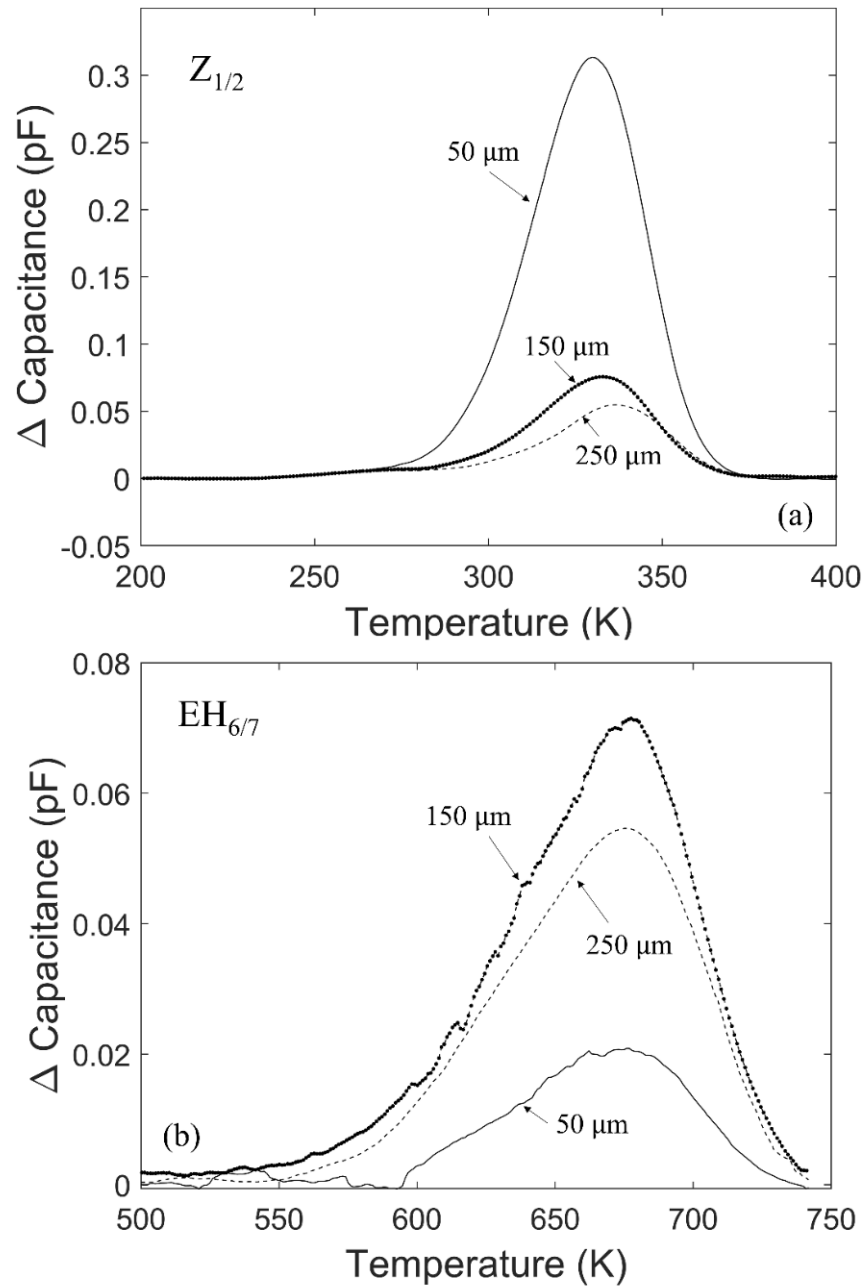


Figure 3.19 DLTS spectra obtained using 0.5 ms initial delays and zoomed in on $Z_{1/2}$ (a) and the spectra obtained using 10 ms initial delays zoomed in on $EH_{6/7}$ (b) for each of the detectors fabricated on 50, 150, and 250 μm epilayers.

3.6 CONCLUSION

The trapping properties of Ni/4H-SiC SBD radiation detectors were investigated for detectors of varying epilayer thicknesses ranging from 50 μm to 250 μm . ^{241}Am pulse height measurements on the detectors showed worsening resolution with increasing detector epilayer thickness. Numerical optimization of the minority carrier diffusion length in a drift-diffusion model for charge collected in SBDs showed decreasing hole diffusion lengths with detector thickness despite increasing resolution suggesting the worst detectors had less hole trapping and therefore were not limited by minority carriers. Careful consideration of the Bragg curve of 5486 keV alpha particles in 4H-SiC along with charge collection theory suggested that at the optimum bias, the signal from the three detectors would predominantly be derived from electron transport. DLTS measurements on the three detectors showed two lifetime limiting peaks, $Z_{1/2}$ and $\text{EH}_{6/7}$, which are both correlated to carbon vacancies by density functional theory. The mean trapping time of $Z_{1/2}$ was significantly lower in the worst performing detector and the results overall showed correlation between the trapping times of both $Z_{1/2}$ and $\text{EH}_{6/7}$ and detector performance.

CHAPTER 4

CURRENT FLOW ANALYSIS BY I-V-T

4.1 INTRODUCTION

One of the major challenges in developing 4H-SiC radiation detectors for harsh environment applications—especially on thicker epilayers—is maintaining sufficiently low leakage currents to avoid degradation of the detection signal. At the radiation detector lab at UofSC, the CR110 preamplifiers used for detector evaluation can typically withstand a detector leakage current of 10 nA before the signal-to-noise ratio (SNR) starts to decline. To avoid reaching this threshold, SBD detectors require as high Schottky barrier heights as possible. Unfortunately, as demonstrated in Sec. 2.3, 4H-SiC SBDs fabricated on as-grown epilayers almost always have leakage currents which exceed those predicted by TED theory because of non-ideal current transport mechanisms such as Poole-Frenkel emission [48]. Furthermore, SBD radiation detectors are fabricated with larger metal contacts than conventional electronics to maximize the detection efficiency leading to a higher probability of spatial variation in the surface barrier height which reduces the effective barrier height while increasing the ideality factor [100]. Additionally, the wider surface area increases the probability of dislocation defects propagated from the bulk being integrated into the M-S junction forming low barrier patches that electrons can use to bypass the main Schottky barrier [101, 102].

Temperature dependent current-voltage (I-V-T) measurements are useful for characterizing the behavior of electronic devices at elevated temperatures and can be employed to separate the nonideal vs. the ideal. For example, I-V-T measurements have been used to characterize barrier inhomogeneities and identify low barrier patches in a variety of materials including 4H-SiC [94, 103, 104]. Under reverse bias, I-V-T can be used to differentiate among various types of current transport mechanisms [105].

In this chapter, I-V-T is employed on a Ni/4H-SiC SBD radiation detector fabricated on 150 μm epitaxial layers to characterize and identify the various current transport models which may result in excess current at elevated temperatures that could impact the SNR in harsh environments. Information on the preparation of the detector discussed in this chapter can be found in Sec. 2.2.

4.2 DEVICE CHARACTERIZATION FROM C-V-T

Before I-V-T measurements could be conducted, the detector was first characterized for temperature variation in its average barrier height and net donor concentration by temperature dependent capacitance-voltage (C-V-T) measurements using the C-V setup described in Sec. 2.3 and the Lakeshore LS335 temperature controller. Measurements were taken from -12 to 0 V for temperatures ranging from 300-600 K at 50 K increments. The parameters were then extracted from their individual Mott-Schottky plots.

Figure 4.1 shows the $1/C^2$ vs. V plots for the detector showing full linearity over the entire voltage range for all temperatures. This indicates that doping profile is uniform, and the M-S junction is nearly ideal with no dielectric layers between the metal and

semiconductor. There is a slight uptick in the slope with temperature indicating that the donor concentration increases.

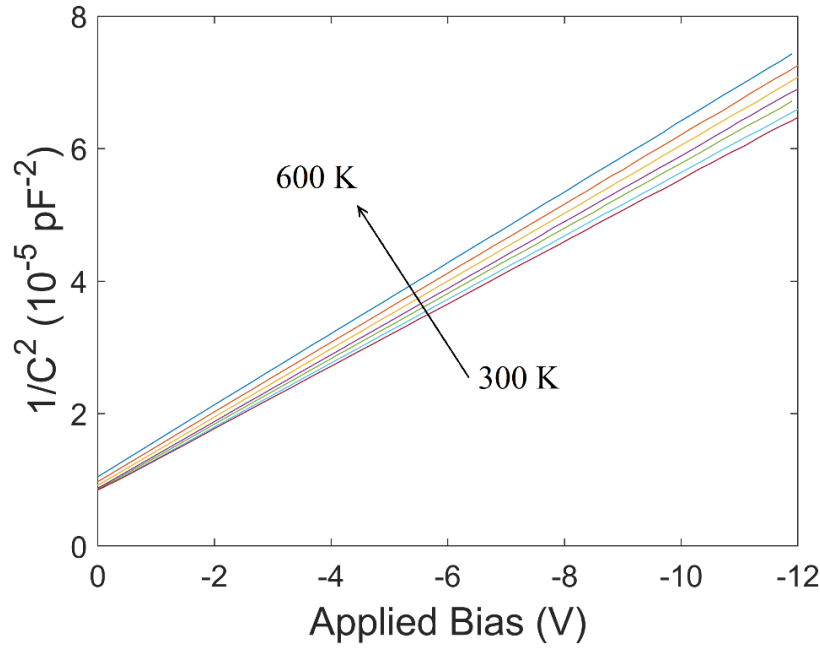


Figure 4.1 Mott-Schottky plots extracted from the C-V-T characteristics for a Ni/n-4H-SiC Schottky barrier detector fabricated on 150 μm epitaxial layers recorded at temperatures between 300 and 600 K in steps of 50 K.

Figure 4.2 shows the extracted values for the net donor concentration N_{eff} and average barrier height Φ_{B0} using Eqns. 2.9 and 2.10. The donor concentration was shown to increase linearly at a rate of $9.6 \times 10^{10} \text{ cm}^{-3} \text{ K}^{-1}$ from 2.12×10^{14} at 300 K to 2.41×10^{14} at 600 K. Impurities have specific ionization energies which relate what percentage of implanted atoms become ionized donors or acceptors to the thermal energy $k_B T$. The net carrier concentration is defined as the difference between the number of ionized donors and acceptors. Since the effective carrier concentration increases slightly with temperature, the donor ionization energies must be slightly lower than the acceptor ionization energies.

The barrier height was found to vary between 2.09 and 2.23 eV in an almost parabolic fashion with the mean situated at 2.16 eV which is approximately the theoretical maximum barrier height for Ni/4H-SiC Schottky contacts. In Schottky diodes, fermi-level pinning by defect states at or near the interface can reduce the average barrier height to the charge neutrality level ($\Phi_{B0} \approx 1.5-1.6$ eV) [106, 107]. The near ideal high average barrier is a strong indication that the surface quality of this diode is very high.

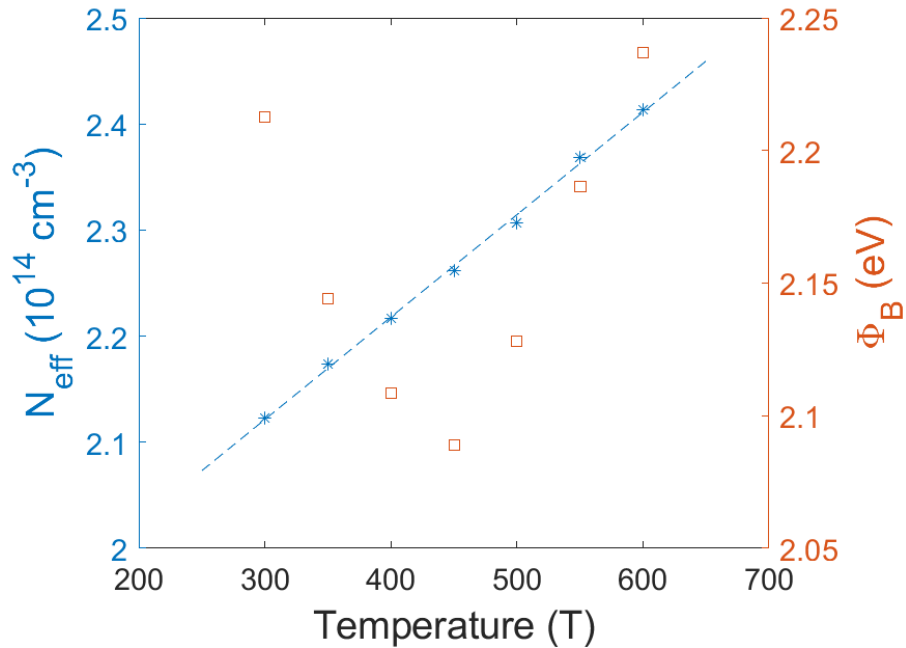


Figure 4.2 Net donor concentration and average barrier height acquired from the C-V-T results on the 150 μm detector.

4.3 SURFACE BARRIER EVALUATION FROM FORWARD BIAS MEASUREMENTS

The surface barrier properties of the detector were characterized by forward bias I-V-T using the Keithley 237 source measure unit and Lakeshore LS335 temperature controller mentioned in the preceding chapters. The detector was mounted in the Janis

VPF800 cryostat as described in Sec. 3.4. The Keithley 237 was connected to the pulse input of the cryostat via low noise BNC cables while the capacitance meter input was grounded out. I-V curves were acquired at 0.01 V steps by sweeping the forward bias voltage between 0 and 1 V in the temperatures range 300-600 K at 50 K intervals.

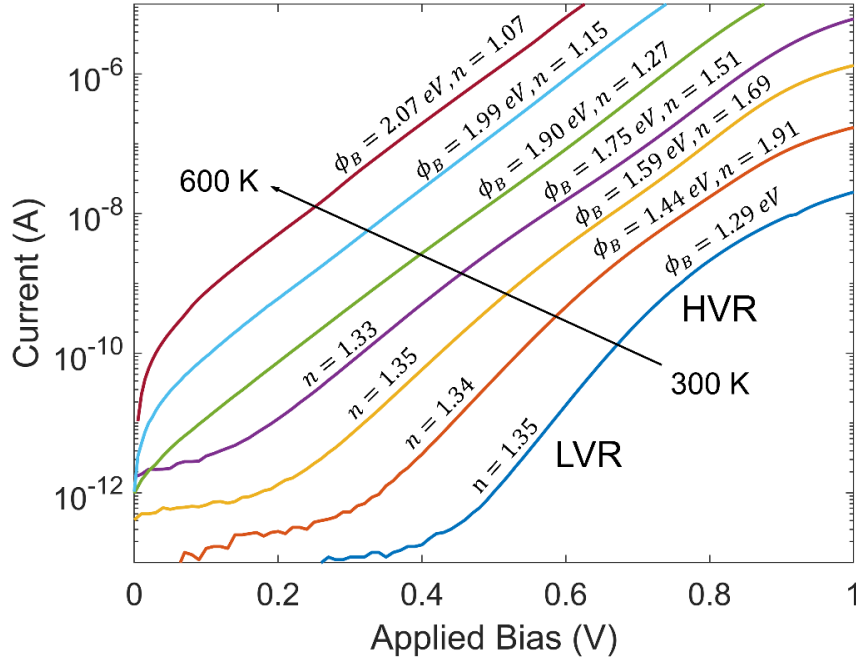


Figure 4.3 Forward bias I-V characteristics for a Ni/n-4H-SiC SBD fabricated on 150 μm epitaxial layers from 300 to 600 K measured in steps of 50 K. The plot is divided by the arrow into two linear regions, the low voltage region (LVR) and high voltage region (HVR).

Figure 4.3 shows the forward bias I-V-T characteristics of the detector. As discussed in Sec. 2.1, the two main types of currents in Ni/4H-SiC SBD radiation detectors are thermionic emission and diffusion, and whichever process is slower will dominate. At a net donor concentration of 10^{14} cm^{-3} diffusion will be slightly slower than thermionic emission under forward bias making neither model exactly accurate for characterizing the effective barrier height and ideality factor. This necessitates the use of the combined TED

model proposed by Sze [39] where the effective carrier velocity is the reciprocal sum of the drift-diffusion velocity $v_D \approx \mu E_m$ and Richardson velocity $v_R = A^*T^2/eN_c$ as shown by the following equation

$$J_{TED} = \frac{eN_c v_R v_D}{v_R + v_D} \exp\left(-\frac{\Phi_B - \Delta\Phi}{k_B T}\right) \left[\exp\left(\frac{eV}{nk_B T}\right) - 1 \right], \quad 4.1$$

which includes the barrier lowering term $\Delta\Phi$. From 300-450 K, the I-V traces clearly show the linear regions with separate ideality factors. This can be caused by impurity or dislocation defects creating a separate localized barrier height distribution independent of the main Schottky barrier [49, 96] and is more likely to occur in 4H-SiC devices with larger contact areas [108, 109].

From the fit to the linear regions, it was found that the low voltage region (LVR) had a constant ideality factor of 1.34 ± 1.01 while the high voltage region (HVR) decreased with rising temperature. The range of the LVR was observed to shrink with increasing temperature starting with a maximum of 0.6 V at 300 K and dropping to 0.4 at 450 K which suggests that the single linear region at 500 K and above corresponded to the HVR. This is further supported by the drop in ideality factor in this region. The effective barrier height was approximately the same for both the LVR and HVR and increased from 1.29 eV at 300 K to 2.07 eV at 600 K.

As presented in Figure 4.4, the reverse saturation current I_0 , defined as the term outside the bracket of Eqn. 4.1, has a linear relationship with $1/k_B T$ when normalized to the effective carrier velocity $v_{eff} = v_R v_D / (v_R + v_D)$ and N_c . Based on Tung's Schottky barrier models, this is indicative of a single low Schottky barrier patch with a barrier height Φ_p and effective area A_p . From the linear fit, Φ_p was calculated to be 0.93 eV which corresponds to a built-in voltage V_{bi} of 0.63 V at 300 K or 0.47 V at 450 K. In SBDs, when

the applied forward bias equals the built-in voltage, the space-charge region will be eliminated. Therefore above V_{bi} of the patch, the patch will be closed off allowing the main Schottky barrier to dominate leading to the double linear region phenomena observed in Figure 4.3. The area of the patch was calculated to be approximately $3 \times 10^{-10} \text{ cm}^2$ corresponding to a diameter of $\approx 200 \text{ nm}$.

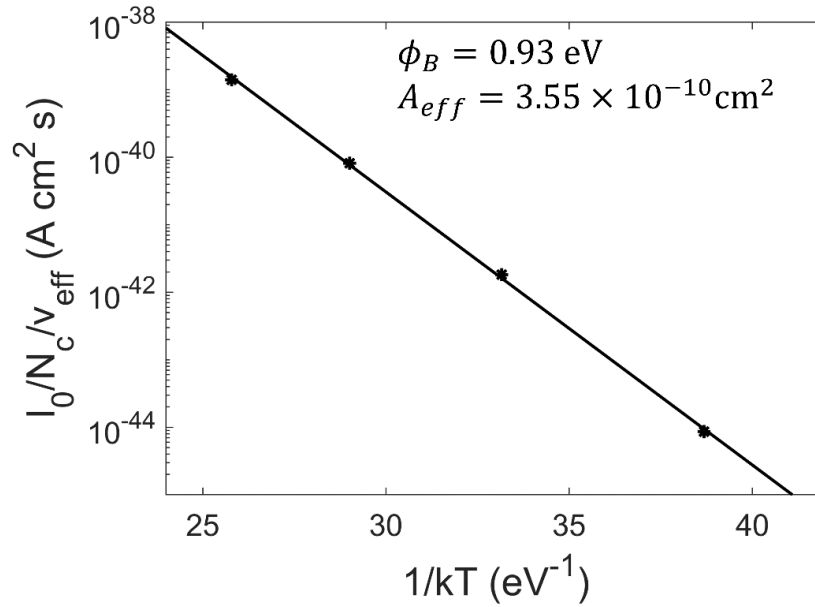


Figure 4.4 Arrhenius plot of the saturation current density I_0 normalized by $N_c v_{\text{eff}}$. The effective carrier velocity v_{eff} is defined as $v_R v_D / (v_R + v_D)$.

As demonstrated by Figure 4.5, the relationship between the ideality factor and effective barrier height of the HVR is linear which implies an inhomogeneous barrier height distribution with an average barrier height Φ_{B0} equivalent to the C-V barrier height [49, 103]. For a spatially distributed barrier height, the net saturation current will be the integral sum of all saturation currents over the entire surface area of the M-S junction and can be described by,

$$I_0 = A^*T^2 \iint \exp\left(-\frac{\Phi_B(x,y)}{k_B T}\right) dx dy. \quad 4.2$$

At low temperatures, most current will prefer to pass through the low barrier regions resulting in an effective barrier height less than the average barrier height Φ_{B0} and an ideality factor greater than one. As temperature increases, more current will pass through the high barrier regions whereas the low barrier regions will saturate causing the effective barrier height to increase towards the average barrier height and the ideality factor to approach one as $T \rightarrow \infty$. Simulation of Tung's original model by Schmitsdorf *et al.* revealed that this relationship is linear and thus the average barrier height can be extracted from intersection of the linear fit of Φ_B vs. n and $n = 1$ [103]. For the present detector, this was calculated to be 2.11 eV which is around what was extracted from the C-V-T results.

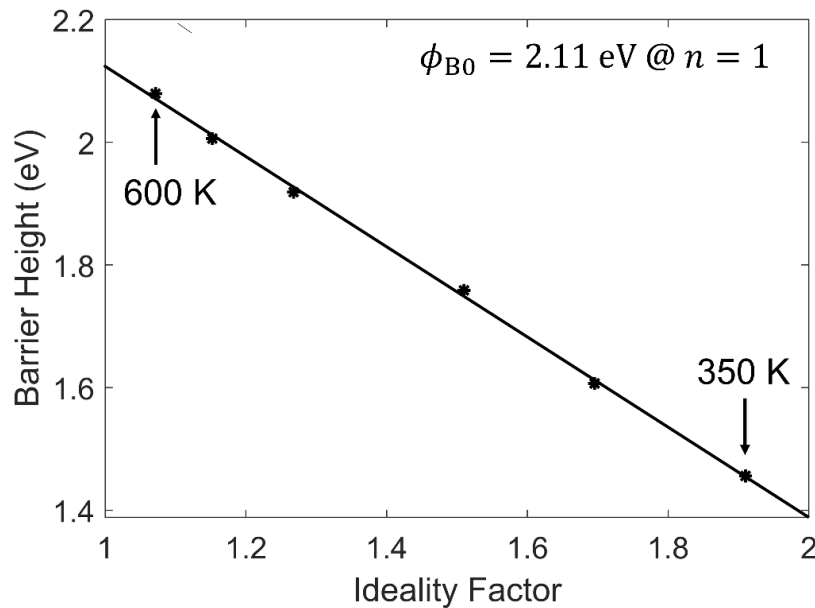


Figure 4.5 Barrier height plotted against the corresponding ideality factor in the HVR. The high temperature region (≥ 500 K) is included as part of the HVR, and the solid line is the linear fit used to acquire the average barrier height Φ_{B0} .

Both the effective barrier height and the dominant low barrier patch will contribute to the total reverse bias leakage current. The potential impact of one versus the other can be estimated by taking the ratio of saturation currents of the low barrier patch I_{p0} to the saturation current of the full Schottky barrier I_0 as shown below,

$$\frac{I_{p0}}{I_0} = \left(\frac{A_p}{A}\right) \exp\left(-\frac{\Phi_p - \Phi_B(T)}{k_B T}\right). \quad 4.3$$

At 300 K, this ratio is approximately 10^{-3} implying that the patch will have a negligible effect on the leakage current. However, the ratio quickly grows with temperature up to 0.5 at 400 K and then peaks at 14 at 500 K, implying that more current will eventually pass through the patch than the main Schottky barrier.

4.4 LEAKAGE CURRENT ANALYSIS FROM REVERSE BIAS MEASUREMENTS

Following evaluation of the surface barrier from the forward bias, the leakage current was analyzed from the detector's reverse bias characteristics. Using the same I-V setup described in the previous section, the leakage current was recorded between reverse biases ranging from 0 to -300 V over the same temperature range. The Janis VPF800 cryostat uses sapphire washers with a room temperature resistivity of 10^{16} Ω -cm to isolate the stands holding the tungsten probes. This is sufficient at room temperature to keep the shunting current below the measuring limit of the Keithley 237. However, the resistivity grows exponentially with temperature and can reach up to 10^{11} Ω -cm at 500 °C. To correct for the shunting current at elevated temperatures, I-V-T data was collected for the cryostat without the detector and then subtracted from the data collected with the detector.

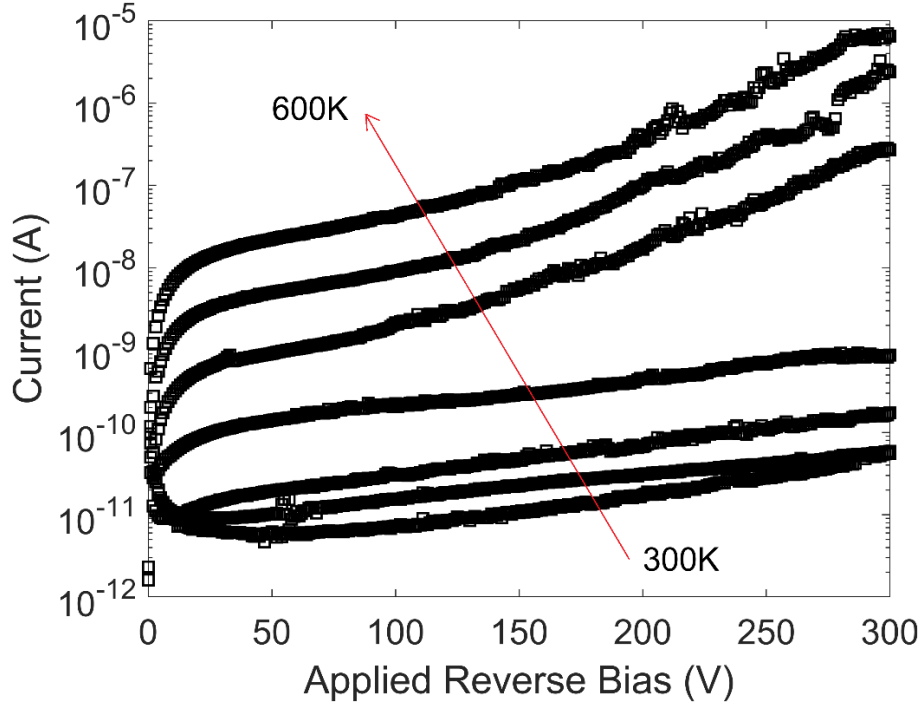


Figure 4.6 Reverse bias I-V characteristics for the Ni/n-4H-SiC SBD fabricated on 150 μm epitaxial layers measured at temperatures ranging from 300 to 600 K in steps of 50 K.

Figure 4.6 shows the detector leakage current as a function of the applied reverse bias which expressed low currents under 100 nA up to 300 V even at 400 K [127 °C]. Above 400 K, the log scale growth in leakage current with temperature becomes substantial, and from 500 K up the leakage current has a much sharper increase in current at higher biases.

As expressed in Figure 4.7, when the leakage current is plotted against the interfacial electric field at low to moderate bias voltages, the relationship is approximately linear at 400 K and above. As discussed in Sec. 2.3, this indicates drift-diffusion current or trap-assisted current by Poole-Frenkel emission. The full expression for the Poole-Frenkel emission current density is given below [53],

$$J_{PF} = e\mu_{PF}n_0E_m \exp\left(-\frac{(E_c - E_T) - \Delta\Phi}{k_B T}\right). \quad 4.4$$

Clearly, under reverse bias, Eqn. 4.4 is effectively identical to the drift-diffusion current given in Eqn. 2.8. The only major changes are that the barrier height is replaced by the activation energy of the trap and $\mu_n N_c$ is replaced by the trap-assisted mobility carrier product $\mu_{pF} n_0$. In both models, the natural log of the slope of J vs. E_m is linear with $1/k_B T$ which allows some activation energy term E_a to be extracted from the following Arrhenius relationship,

$$\ln\left(\frac{dJ}{dE_m}\right) = K - \frac{E_a}{k_B T}, \quad 4.5$$

where, K is a constant related to the factor outside the exponential in Eqns. 2.8 and 4.4.

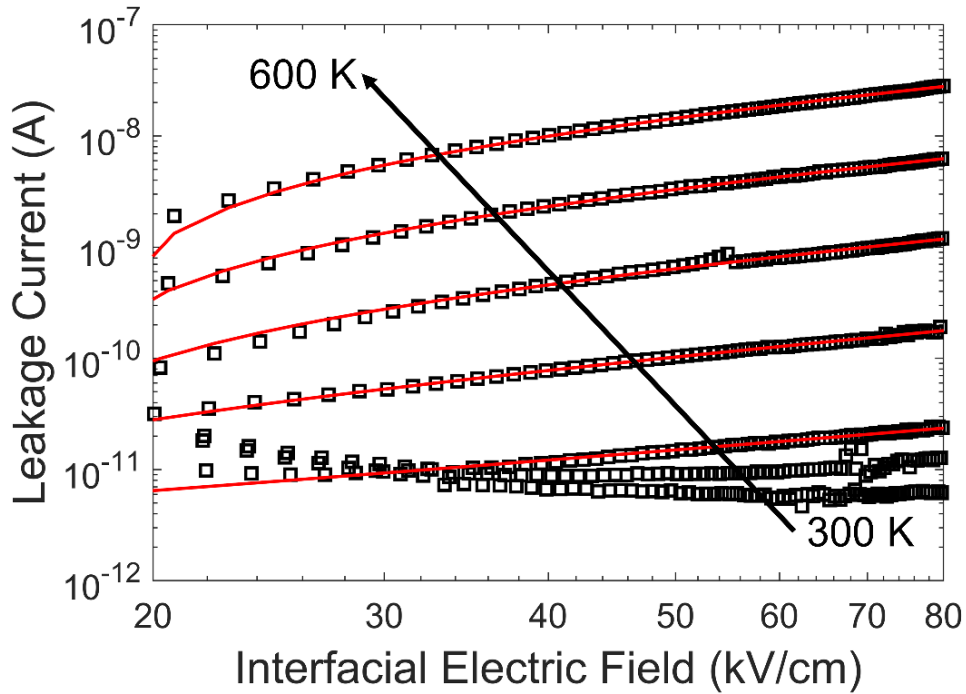


Figure 4.7 Reverse bias leakage current as a function of the electric field at the metal-semiconductor interface for the I-V-T characterized 150 μm epitaxial layer detector. The solid lines are the linear fit to the data points.

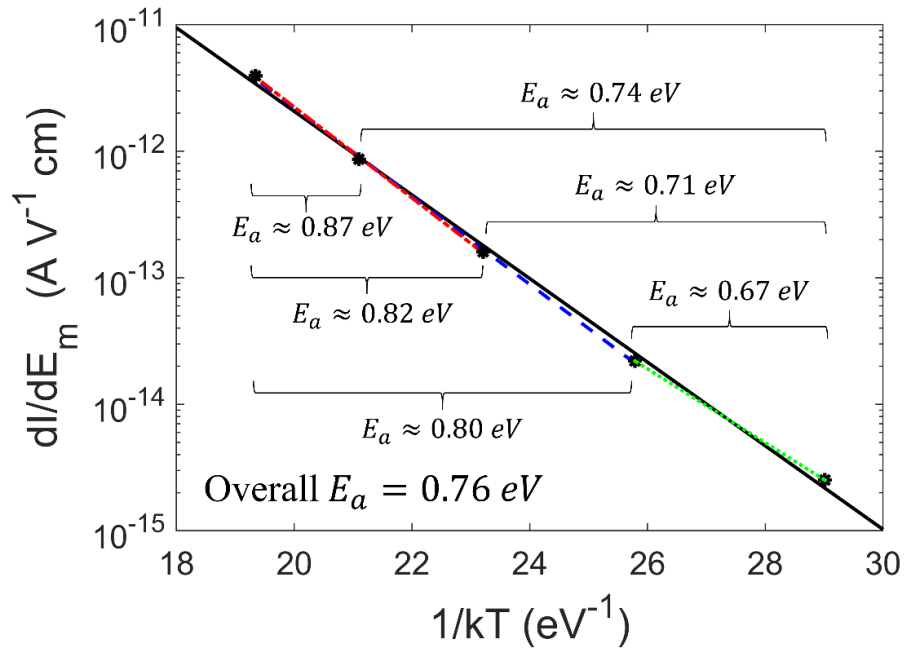


Figure 4.8 Arrhenius plots of the slopes of each I-V trace from 20 to 80 kV/cm. The solid line is the overall linear fit, whereas the dashed and dotted lines correspond to the fits over a reduced temperature range.

From the Arrhenius plot in Figure 4.8, the overall activation energy from 400-600 K is extracted to be 0.76 eV which is lower than expected for the low barrier patch. The leakage current could be derived from Poole-Frenkel emission, but an activation energy of 0.76 eV would correspond to silicon vacancies which theoretically cannot exist in as-grown 4H-SiC [84, 88]. It should also be noted that from the model described by Eqn. 4.3, the low barrier patch is not expected to be a significant contributor to the total leakage current until 500 K. Accounting for this, if 400 and 450 K are removed from the linear fitting to the Arrhenius model, then the activation energy increases to 0.82 eV which is closer to the barrier height of the patch, especially when considering an expected barrier lowering of ≈ 0.04 - 0.05 eV over the range of 20-80 kV/cm. Likewise, if 550 and 600 K are removed from the fitting, the activation energy reduces to 0.71 eV. In summary, the activation

energy of 0.76 eV appears to be overlap of at least two effects with activation energies greater than 0.8 eV and below 0.7 eV.

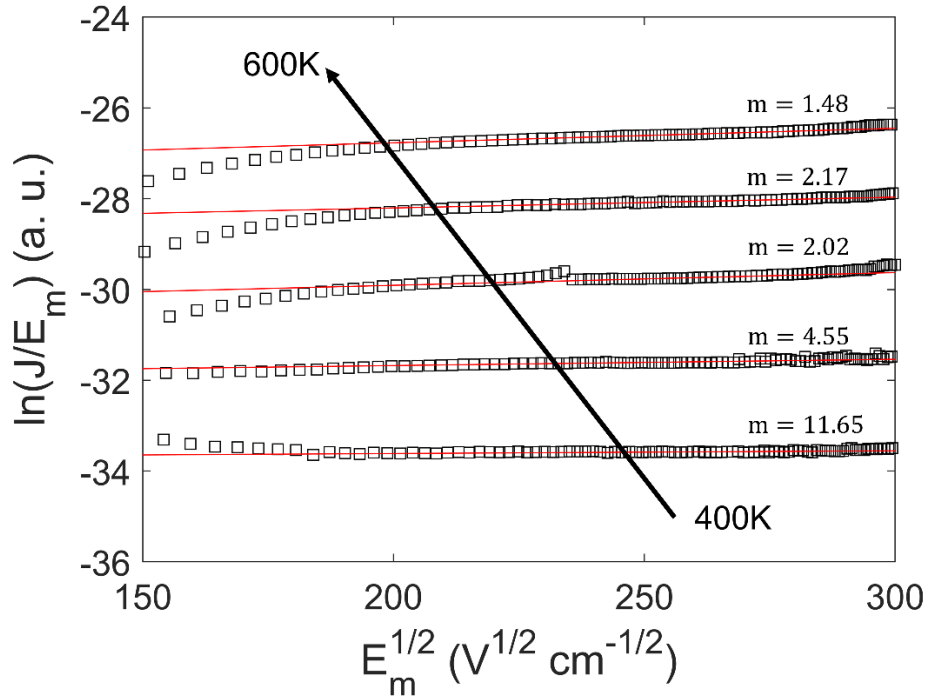


Figure 4.9 Natural logarithm of the reverse bias leakage current normalized to the interfacial electric field plotted against the square root of the interfacial electric field for the I-V-T characterized 150 μm epilayer detector.

These effects can be differentiated from their barrier lowering as described by Eqn. 2.11 in Sec. 2.3. Figure 4.9 shows the $\ln(J/E_m)$ vs. $E_m^{1/2}$ plot used to extract the barrier lowering parameter m at each temperature. At 400 and 450 K, m is 11.65 and 4.55, respectively. At 20-80 kV/cm, this suggests that the barrier lowering would be less than 0.01 eV which is equivalent to no barrier lowering at all. It should be noted that Poole-Frenkel barrier lowering is a coulombic effect and thus there will only be barrier lowering if the assisting defect level is charged [110, 111]. Given the lack of barrier lowering and that the activation energy drops below 0.7 eV as temperature decreases, it is likely that the

leakage current at these two temperatures is derived from $Z_{1/2}$ or the $(0|-1)$ transition of the carbon vacancy which would be neutrally charged in the depletion region under reverse bias.

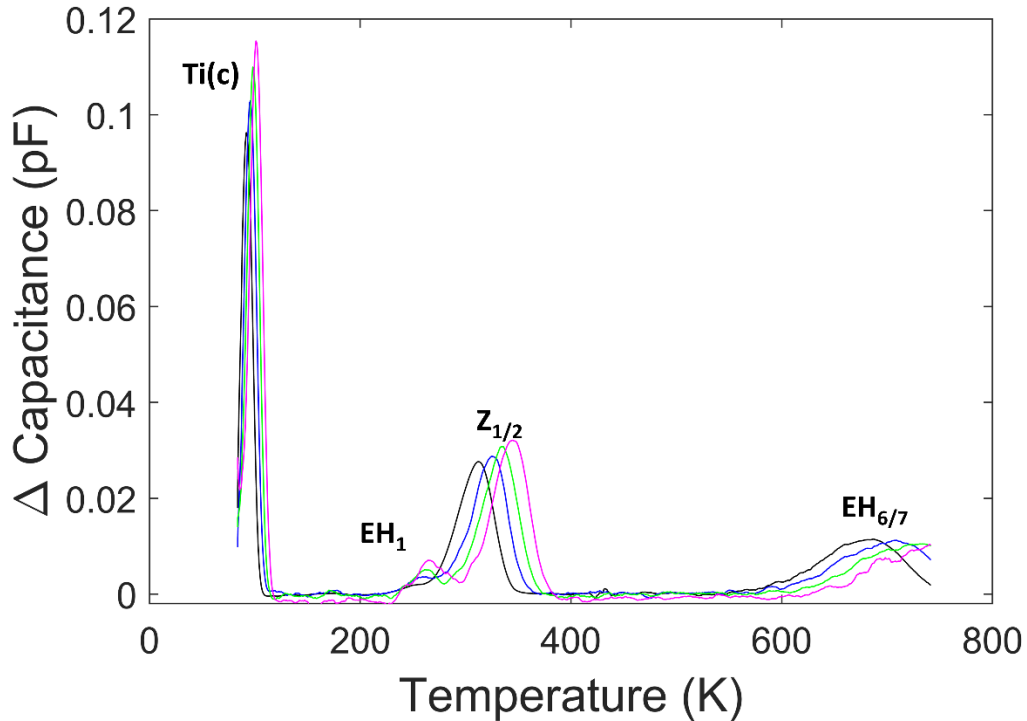


Figure 4.10 DLTS spectra of the I-V-T characterized 150 μm epilayer detector using the initial delays 0.5, 1, 2, and 5 ms.

This can be verified from the DLTS spectrum of the detector presented in Figure 4.10. For this sample, DLTS studies were conducted from 80-750 K using a -5 V steady-state bias and a 0 V, 1 μs filling pulse. The spectrum showed four peaks labeled Ti (c), EH_1 , $Z_{1/2}$, and $\text{EH}_{6/7}$. Their corresponding Arrhenius plots are given in Figure 4.11 and defect parameters are recorded in Table 4.1. The only unusual peak in the spectrum is the EH_1 reported by Castaldini *et al.* [112]. However, its trap concentration is $\sim 10^{10} \text{ cm}^{-3}$ making it mostly irrelevant compared to the other peaks. While $\text{EH}_{6/7}$ mostly corresponds

to the carbon vacancy, $Z_{1/2}$ can be a composite peak consisting of carbon vacancies and other related defects such as di-antisites or divacancies but is always greater than equal to the $EH_{6/7}$ peak [71]. For this detector, the $Z_{1/2}$ and $EH_{6/7}$ trap concentrations are identical at $2 \times 10^{11} \text{ cm}^{-3}$ implying that both near exclusively correspond to carbon vacancies. Therefore, $Z_{1/2}$ is the (0|-1) transition and could be the main transport mechanism of the leakage current at 400 and 450 K.

At 500 and 550 K, the barrier lowering term is approximately 2. Based on the activation energy $>0.8 \text{ eV}$, this likely corresponds to Schottky barrier lowering of the low barrier patch. At 600 K, the parameter is ~ 1.5 indicating that both Schottky lowering and Poole-Frenkel lowering are contributing to the net barrier lowering which could be due to $EH_{6/7}$ becoming active as the temperature increases.

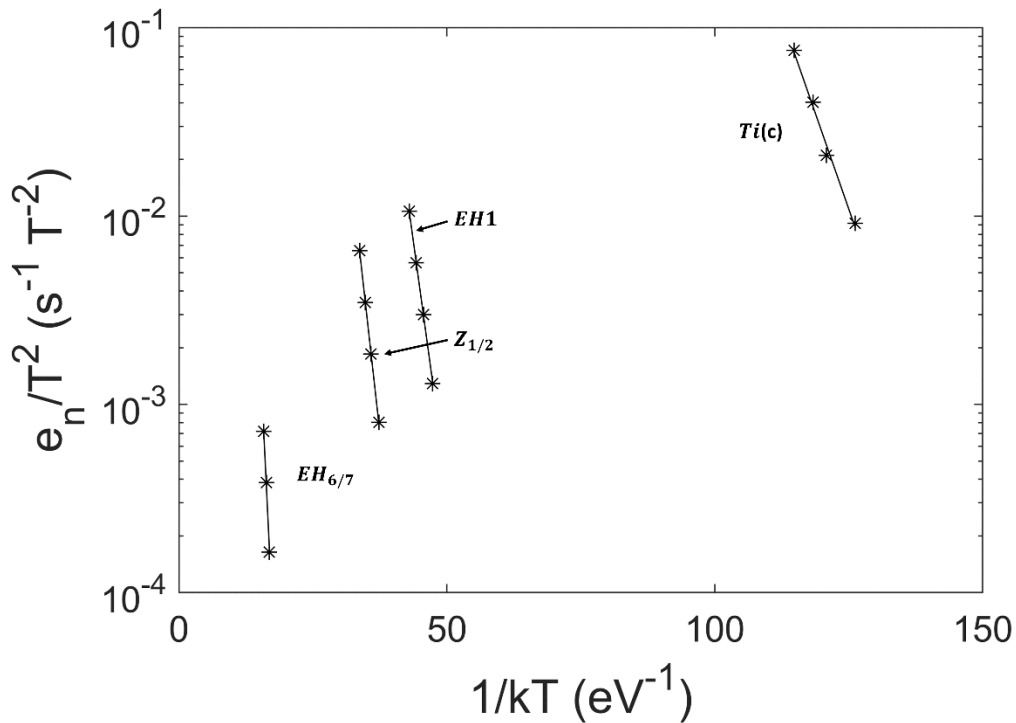


Figure 4.11 Arrhenius plot of the emission rates for the spectrum in Figure 4.10.

Table 4.1 Defect parameters obtained from DLTS spectrum of the 150 μm detector.

Defect Level	$E_c - E_T$ (eV)	σ_n (cm^2)	N_t (cm^{-3})
Ti (c)	0.19	10^{-14}	8.9×10^{11}
EH_1	0.48	$\sim 10^{-15}$	4.6×10^{10}
$Z_{1/2}$	0.59	$\sim 10^{-16}$ - 10^{-15}	2.1×10^{11}
$\text{EH}_{6/7}$	1.35	$\sim 10^{-16}$	2.0×10^{11}

4.5 CONCLUSION

A 4H-SiC SBD radiation detector was fabricated on 150 μm epitaxial layers and characterized by I-V-T measurements to determine the current flow mechanisms at elevated temperatures in preparation for harsh environment applications. From preliminary C-V-T measurements, the detector had a nearly ideal average barrier height of 2.16 eV and carrier concentration of $2 \times 10^{14} \text{ cm}^{-3}$. The forward bias I-V-T characteristics revealed the presence of two linear regions. The low voltage region had a constant ideality factor of ≈ 1.3 and corresponded to a low barrier patch—likely derived from a dislocation defect—with a barrier height of 0.93 eV. The high voltage region showed a linear correlation between barrier height and ideality factor which implied that the main Schottky barrier was inhomogeneous. From the intersection of the linear fit and $n = 1$, the average barrier height was extracted to be 2.11 eV which agrees with the C-V-T results.

The reverse bias leakage current was proven to be linear with the interfacial electric field at 400 K and above. Exponential fitting of the slopes of the individual I-V curves revealed an activation energy of 0.76 eV. When compared with the barrier lowering, it was determined that this activation energy was the result of the overlap between trap-assisted current through a neutrally charged trap with an activation energy less than 0.7 eV and the

low barrier patch revealed by the forward bias characteristics. DLTS results suggest that the neutrally charged trap is $Z_{1/2}$ which corresponds to the $(0|-1)$ transition of the carbon vacancy. At 600 K, the barrier lowering dipped below 2, implying transport becomes assisted by a charged trap such as $EH_{6/7}$ at elevated temperatures. The absence of barrier lowering at room temperature compared to the 250 μm detectors described in Sec. 2.3 could be attributed to the difference in composition of the $Z_{1/2}$ peak which can potentially encompass additional defects other than carbon vacancies especially when the concentration is higher than the $EH_{6/7}$ peak.

CHAPTER 5

NEUTRON IRRADIATED 4H-SiC EPITAXIAL LAYERS

5.1 INTRODUCTION

One of the difficulties in developing radiation detectors for harsh environments is finding materials which can sustain continuous bombardment from heavy background irradiation fields. These fields can consist of high energy nuclear particles such as protons, neutrons, or gamma rays which are small enough to completely avoid collision with the electron cloud and directly scatter across the nucleus. If the energy of the incident particle is high enough, then it can either break the atom free from its crystalline position creating a point defect, or shatter the nucleus completely creating two radioactive atoms with the crystal structure, or will embed itself in the nucleus activating it [113]. At high energies, the probability of these events is reduced the lower the atomic numbers of the constituent atoms are. This makes 4H-SiC a material of high interest for application in harsh environments such as the reactor core or lunar surface.

Irradiation studies are often employed to study the effect of high energy particle bombardment on a device or material. This usually involves correlation of device performance with irradiation dose and the introduced deep levels. Occasionally, irradiation is done deliberately to introduce defects with promising properties for optical or quantum computing applications [114, 115]. Irradiation studies on 4H-SiC have been performed with a wide variety of particles including electrons, protons, neutrons, and heavy ions [22, 89, 112, 116-118]. However, very little has been done to correlate the effect of irradiations

on detector performance especially with modern, high quality epilayers as dealt in this dissertation.

In this study, 4H-SiC samples from the same parent wafer as those described in Chapter 2 were exposed to neutron fluences up to 10^{13} cm⁻². Detectors were then fabricated using these samples and characterized for their electronic and radiation detection properties. The variation in detection performance was correlated with defect levels using a wide variety of techniques including DLTS, current transient spectroscopy (CTS), and photoinduced current transient spectroscopy (PICTS).

5.2 IRRADIATION PROCEDURE

Four 250 μ m 4H-SiC samples obtained from the same parent wafer as described in Chapter 2 were irradiated with cadmium-filtered neutrons at Kansas State University in the TRIGA Mark II nuclear reactor facility. Before irradiation, the samples were first loaded into 20 mm thick cadmium envelopes which shields the samples from thermal and epithermal neutrons with energies below 0.4 eV. The envelopes were then loaded into dry sample tubes or Intra-Reflector Irradiation System (IRIS) ports (Figure 5.1) which have thermal and fast (>1 MeV) neutron flux densities of 4.75×10^6 and 2.96×10^6 cm⁻² s⁻¹, respectively, and an estimated gamma dose rate of 1.06×10^2 rad s⁻¹ for each watt of applied reactor power. To minimize the error in fluences, the reactor power was set such that the irradiation duration was at least 100 times the loading duration. The accumulated fluence for each sample was calculated from a power normalized flux density acquired in gold activation foils within the cadmium envelope and recorded in Table 1. The estimated background gamma doses were between 400 Rad and 300 kRad and deemed minor

compared to the neutron dose. Upon return to UofSC, the samples were prepped and fabricated into radiation detectors according to the procedures described in Sec. 2.2.

Table 5.1 Accumulated neutron dose of 250 μm 4H-SiC epitaxial layer samples.

Detector ID	Total Neutron Fluence (cm^{-2})	Fast Neutron Fluence (cm^{-2})
N1	$(5.07 \pm 0.14) \times 10^{10}$	$(6.59 \pm 0.19) \times 10^9$
N2	$(4.46 \pm 0.13) \times 10^{11}$	$(5.79 \pm 0.17) \times 10^{10}$
N3	$(4.89 \pm 0.14) \times 10^{12}$	$(6.36 \pm 0.19) \times 10^{11}$
N4	$(4.75 \pm 0.14) \times 10^{13}$	$(6.17 \pm 0.19) \times 10^{12}$

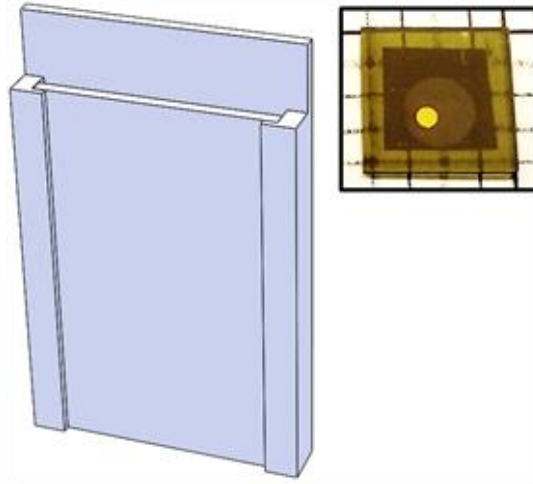


Figure 5.1 The cadmium envelope (left) and the finished detector (right).

5.3 DETECTOR CHARACTERIZATION

Figure 5.2 shows the forward and reverse characteristics of detectors fabricated on the neutron irradiated epitaxial layers. The first three detectors N1 (10^{10} cm^{-2}), N2 (10^{11} cm^{-2}), and N3 (10^{12} cm^{-2}) had typical SBD behavior with barrier heights ranging from 1.5

to 1.7, ideality factors from 1.1 to 1.5, and leakage currents from 0.3-0.5 nA with no apparent correlation between any of these three parameters and net dose. The only detector that expressed any behavior out of the ordinary was N4 (10^{13} cm^{-2}) which manifested low forward bias current that appeared linear and symmetric with the reverse bias I-V profiles. This is linked to an increase in series resistance that has been observed in most neutron irradiated epilayers [118-120] and originates from donor compensation by introduced deep levels. Taking the linear fit of the forward bias regime suggests that the resistivity of the neutral region has grown to $\sim 10^{12} \Omega\text{-cm}$.

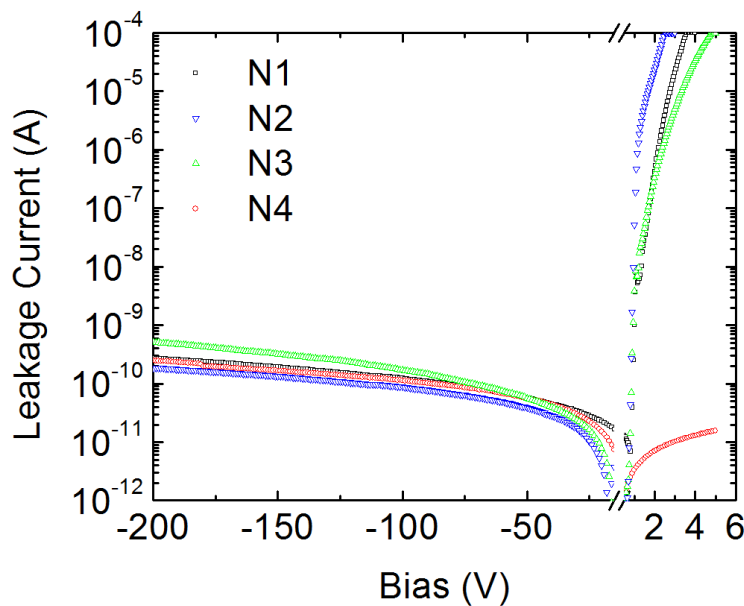


Figure 5.2 Forward and reverse bias I-V characteristics for detectors fabricated on neutron irradiated epilayers.

The Mott-Schottky plots attained from the C-V characteristics are presented in Figure 5.3. N1 and N2 exhibited typical junction capacitances for unirradiated 4H-SiC SBD radiation detectors corresponding to doping concentrations within the expected range for the parent wafer ($1-2 \times 10^{14} \text{ cm}^{-3}$). N3 had a linear region which could be used to exact

a carrier concentration of $6.6 \times 10^{13} \text{ cm}^{-3}$ —roughly half the previous two samples. However, even considering the reduction in carrier concentration, it had an abnormally low capacitance and a profile that indicated a large surface charge density. N4 had a constant capacitance of 4.86 pF suggesting that either the contact is ohmic or the carrier density has been compensated so severely that it is effectively fully depleted even at zero bias.

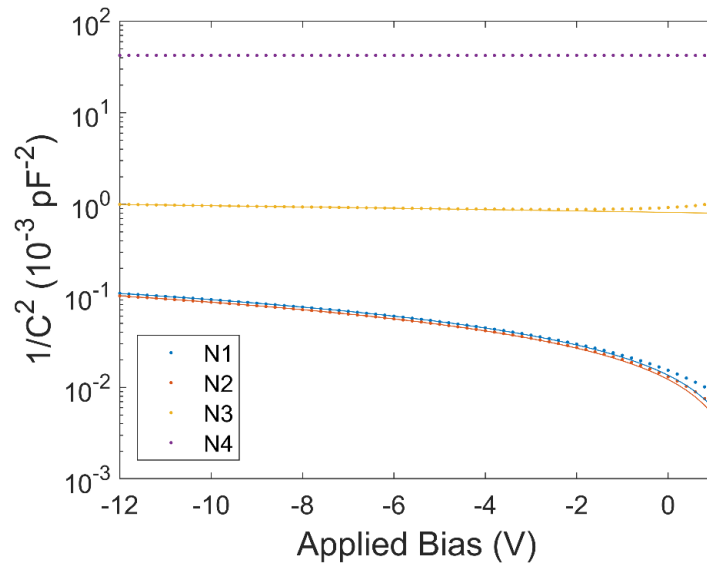


Figure 5.3 Mott-Schottky plots for the detectors fabricated on neutron irradiated 4H-SiC epitaxial layers given in semi-log scale to show the difference in capacitance profiles between the lightly and heavily irradiated samples.

Popelka *et al.* defined the donor removal rate as the differential change in net donor concentration with neutron fluence and calculated it to be 18.9 cm^{-1} for 1 MeV neutrons [118]. For neutrons greater than 1 MeV, it has been calculated to be as low as 9.7 [121]. Using the resistivity of N4 and the >1 MeV neutron fluence of $6 \times 10^{12} \text{ cm}^{-2}$, the donor removal rate for the present irradiations is estimated to be $\approx 20 \text{ cm}^{-1}$.

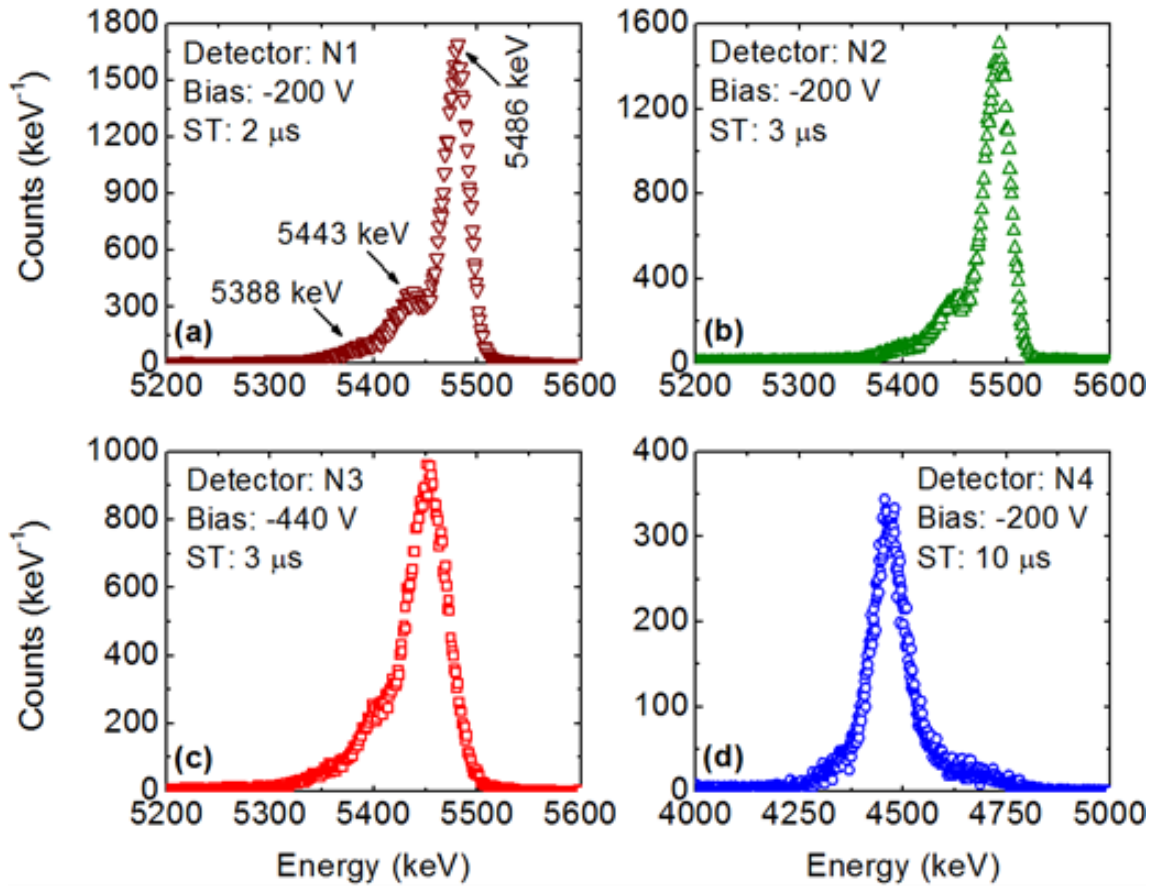


Figure 5.4 Optimal pulse height spectra obtained for the detectors (a) N1, (b) N2, (c) N3, and (d) N4, fabricated on neutron irradiated epilayers, when exposed to an ^{241}Am alpha particle source.

The optimal pulse height spectra were obtained for each of the detectors and presented in Figure 5.4. The two lightly irradiated samples N1 and N2 had resolutions of 28 and 29 keV ($\sim 0.5\%$) FWHM for 5486 keV alpha particles, respectively, and demonstrated clearly resolved 5388 and 5443 keV peaks. To achieve the optimum energy resolution, detector N2 needed a slightly longer shaping time of 3 μs compared to 2 μs for N1. When the electronic noise peak broadening is negligible compared to detector peak broadening, longer shaping times can indicate more trapping and de-trapping from shallow or lower energy deep levels with ns to μs emission times (e_n^{-1}), prolonging the rise time of the preamplifier output. Detector N3 had a similar optimal shaping time of 3 μs but required

a higher bias of -440 V, compared to -200 V for N1 and N2, to reach its optimal resolution of 42 keV (0.8%). The large operating bias suggested that hole trapping was severe even with the strong electric field of the space-charge region. The best resolution achieved for N4 was 76 keV (1.8 %) at -600 V and the maximum shaping time of 10 μ s for the ORTEC 572 shaping amplifier. It can be inferred from the significant rightward tailing of the peak that 10 μ s is not a sufficiently long enough shaping time for maximum charge collection. Both the electrical and radiation detector properties of the devices are tabulated in Table 5.2.

Table 5.2 Summary of electrical and radiation detection properties of detectors fabricated on neutron irradiated 4H-SiC epitaxial layers.

Det ID	ϕ_B (eV)	n	N_{eff} (10^{14} cm^{-3})	$I @-200\text{V}$ (pA)	Bias (-V)	Shaping Time (μ s)	Energy Resolution (keV (%))	L_d (μ m)
N1	1.60	1.44	1.32	272	200	2	28 (0.5)	10
N2	1.69	1.69	1.39	187	200	3	29 (0.5)	5.9
N3	1.58	1.58	0.66	506	440	3	42 (0.8)	2.6
N4*	-	-	-	249	600	10	76 (1.8)	-

*Not all parameters could be determined for N4 due to donor compensation.

More information on detector trapping can be interpreted from the variation in energy resolution as a function of the applied reverse bias. As shown in Figure 5.5, the energy resolution of detectors N1 and N2 improved as the bias increased until stabilizing at ~50 V which puts the depletion width just beyond the range of the alpha particles. However, on the lead up to 50 V, the resolution of N2 was lower than N1 and rose much more sharply. This could indicate that hole trapping during diffusion from the neutral

region is more severe than trapping in the space-charge region. On the other hand, the energy resolution of detector N3 does not saturate until 300 V implying that trapping has become more severe in the space-charge region. Due to the ohmic-type behavior of detector N4, the electric field will be distributed across the entire epilayer thickness. Since the range of the alpha particle is only $18.22 \mu\text{m} \ll 250 \mu\text{m}$, under reverse bias, greater than 90% of the radiation induced current will be derived from electron transport—possibly 100% if the hole properties are sufficiently diminished. Assuming the electric field distribution is approximately constant, electrons will reach saturation velocity at 500 V reverse bias. The implication is that even at saturation drift velocity and $> 90\%$ electron transport, the resolution has degraded compared to the three previous samples implying a clear decline in the electron trapping time.

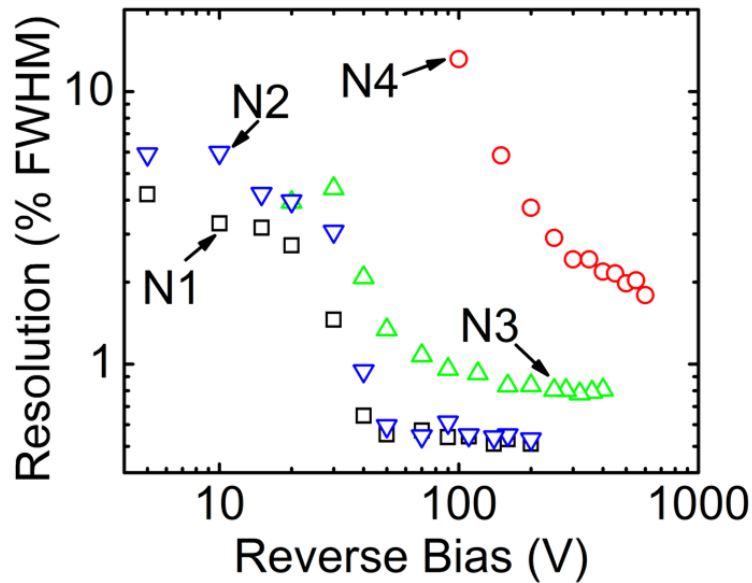


Figure 5.5 Detector resolution plotted against the applied reverse bias at the optimal shaping times on a log-log scale for better visibility.

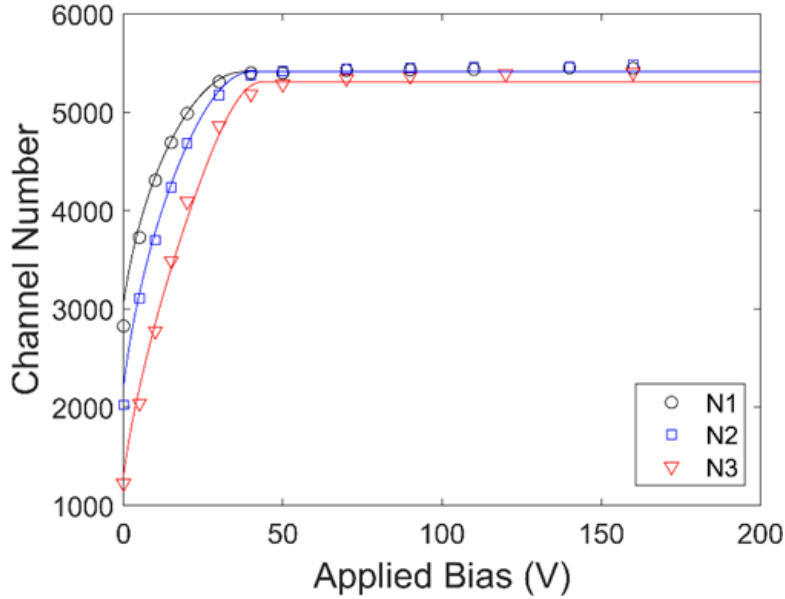


Figure 5.6 Detector N1, N2, and N3 charge collected in channel number plotted against the applied reverse bias using optimal shaping times. The solid lines are the fit to the drift-diffusion model.

Figure 5.6 shows the charge collected for the detectors plotted against the reverse bias for the three SBDs. Fitting the plot to the drift-diffusion model (Sec. 3.2) shows a clear decline in minority carrier diffusion length L_d from 10 μm in N1 to 2.6 μm in N3 indicating a clear increase in hole trapping. Detector N3 also had a slightly lower amount of charge collected than N1 and N2. As is apparent in Figure 5.7, N4 only managed to collect $\sim 80\%$ the total charge (compared $\sim 100\%$ for the three SBDs). This effect has been observed in GaAs detectors and is related to carrier trapping [122]. Exhibiting semi-insulating behavior, the drift-diffusion model cannot be applied to N4. However, because the range of the alpha particles x_r is much shorter than the thickness of the epilayer d , charge collected can be modeled by a single interaction point approximately equal to x_r . Additionally, since the contact area is much larger than the thickness of the detector, the weighting potential will be the same as for a planar detector. Thus, the charge collected can

be modeled by the single charge carrier Hecht equation which after inserting the appropriate terms is given by,

$$Q \propto \frac{\mu_n \tau_n (V - V_0)}{(d^2 - dx_r)} \left[1 - \exp\left(-\frac{(d^2 - dx_r)}{\mu_n \tau_n (V - V_0)}\right) \right]. \quad 5.1$$

Here, V_0 is an offset voltage to correct for any surface polarization from surface traps or the minor amount of charge collection expected from holes (< 10 %). After fitting the data in Figure 5.7 to Eqn. 5.1, τ_n was extracted to be 7.38 ns.

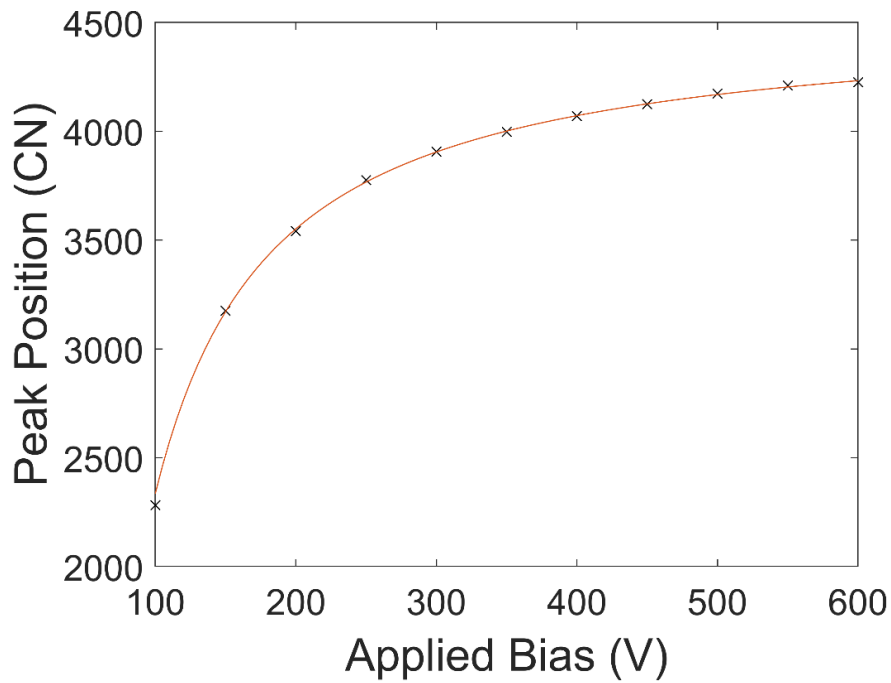


Figure 5.7 Charge collected in channel number plotted against the applied reverse bias for detector N4. The solid line is the fit to Eqn. 5.1. CN refers to the channel number.

5.4 ALTERNATIVE DEFECT CHARACTERIZATION METHODS: CTS AND PICTS

While DLTS is a powerful tool for the characterization of defect levels in rectifying devices such as SBDs and p-n junction diodes, it cannot be applied for devices with low background capacitance such as rectifying devices with low doping concentration or heavy

surface charging or insulating materials with invariant capacitance. The former can be resolved by using current transient spectroscopy (CTS) also known as I-DLTS [123]. In traditional capacitance DLTS, the capacitance transient is derived from the emission of trapped electrons back to the conduction wherein they are immediately swept up by the electric field and ejected to the neutral region producing a current. Under the high electric field, the current induced by the sweeping of these charges will be rate limited by the emission rate of traps and the net charge within the window Δx can be described by the following,

$$Q(t) = eA \int_0^{\Delta x} N_{eff} - N_T \exp(-e_n t) dx. \quad 5.2$$

Essentially, the total charge equals the charge density of the region Δx multiplied by the region's volume. The emission current is then the first derivative with respect to time,

$$i_T(t) = eA\Delta x N_T e_n \exp(-e_n t). \quad 5.3$$

Including the background DC current, this equation is nearly identical in form to the capacitance transient in Eqn. 3.16 and similarly the trap parameters can be derived from the difference spectrum. The main difference is that emission rate is outside the exponential which can slightly elongate the rightward tailing of the peaks. Furthermore, the additional current at the start of the transient does not depend on the steady-state current (unlike capacitance DLTS which depends on the steady-state capacitance) and will produce more reliable signals at lower background DC current.

Resistive and insulating materials require optical methods to characterize the trap parameters such as photoinduced current transient spectroscopy (PICTS) [124]. As demonstrated in Figure 5.8, when light or any radiation is applied to a material, electron-

hole pairs are generated at a point of interaction. Applying an electric field will cause these carriers to drift until they are captured by trapping centers. For electrons, the mean free path will be $\mu_n \tau_n |V|/d$. After a sufficiently long enough time under illumination, trapping and de-trapping will reach steady state and all traps within a volume $\mu_n \tau_n |V|A/d$ (for electrons) will be filled. Upon removal of the light source, trapped charges in the volume will be emitted back to their respective bands and swept up by the electric field generating a current of the same form as Eqn. 5.3,

$$i_T(t) = \frac{eA\mu_n\tau_nVN_T}{d} e_n \exp(-e_n t). \quad 5.4$$

Through careful selection of the optical source and sign of the applied bias, the carrier type of the emission current can be controlled.

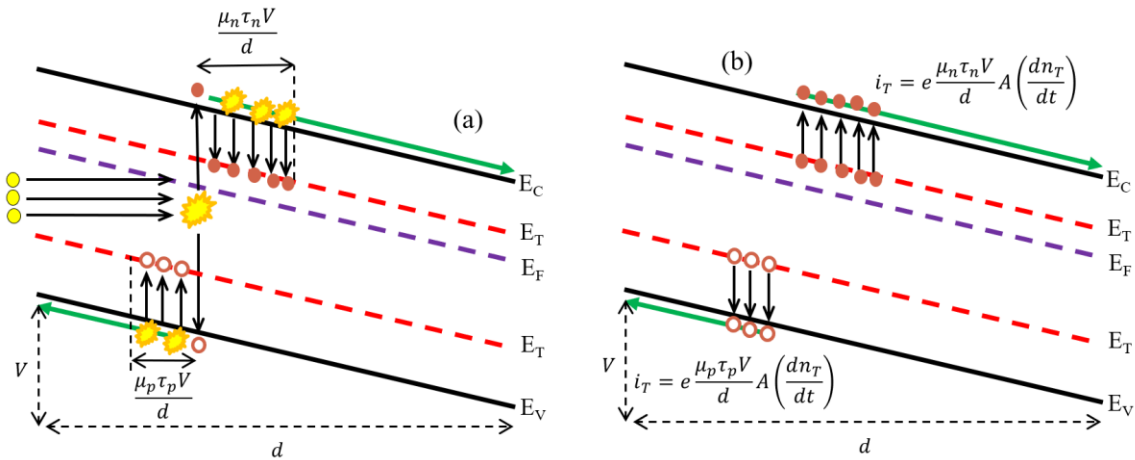


Figure 5.8 Illustration of charge carrier trapping under illumination (a) and the emission of charge carriers once the light source is removed (b).

CTS is an available function of the DDS-12 system. In current mode, the rate window is defined as 1.93 times the initial delay which will slightly alter the positions of the trap levels compared to capacitance mode. During measurements, the output of the

Janis VPF 800 cryostat is connected to a CTS configured current meter through a separate BNC connection on DDS-12's main panel.

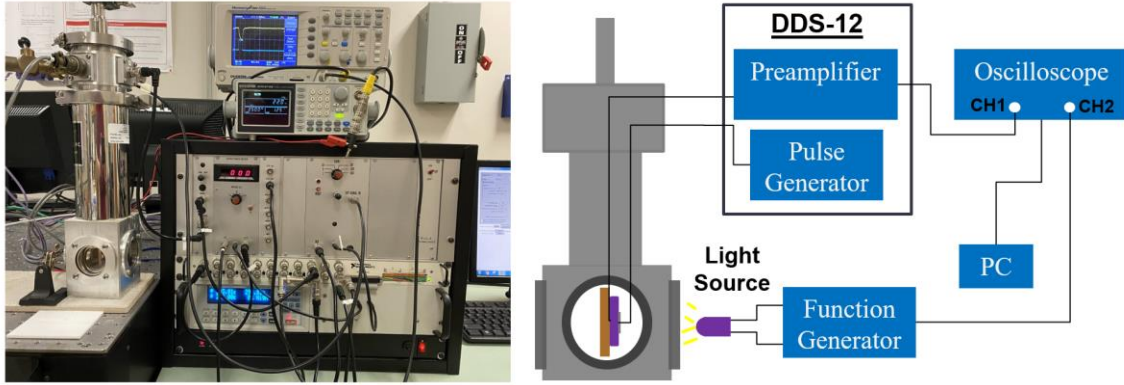


Figure 5.9 Photograph and diagram of the PICTS system designed and implemented at UofSC.

The DDS-12 does not have a built-in PICTS function. However, the preamplifier module does allow for external input and output signals for the design of homebrewed spectroscopic systems. At UofSC, a PICTS system has been developed consisting of a Janis VPF800 cryostat which uses the pulse out connection of the DDS-12 for biasing the detector. The output of the preamplifier was then fed into channel one of a GWINSTEK GDS-1062A digital oscilloscope for signal acquisition. The cryostat had four quartz windows at the base for applying optical signals to devices. Depending on the device, either a directional LED or laser diode was aimed directly at the detector surface through one of these four windows. The optical source was controlled by a GWINSTEK AFG-2105 arbitrary function generator which was connected in parallel to channel two of the oscilloscope to serve as the triggering signal. The digital waveforms from the oscilloscope were exported to a PC via USB for pulse processing and data acquisition in an in-house

developed LabVIEW waveform analysis program. A schematic diagram of the system is given in Figure 5.9. As in DLTS and CTS, the temperature was controlled through the Lakeshore LS335 temperature controller.

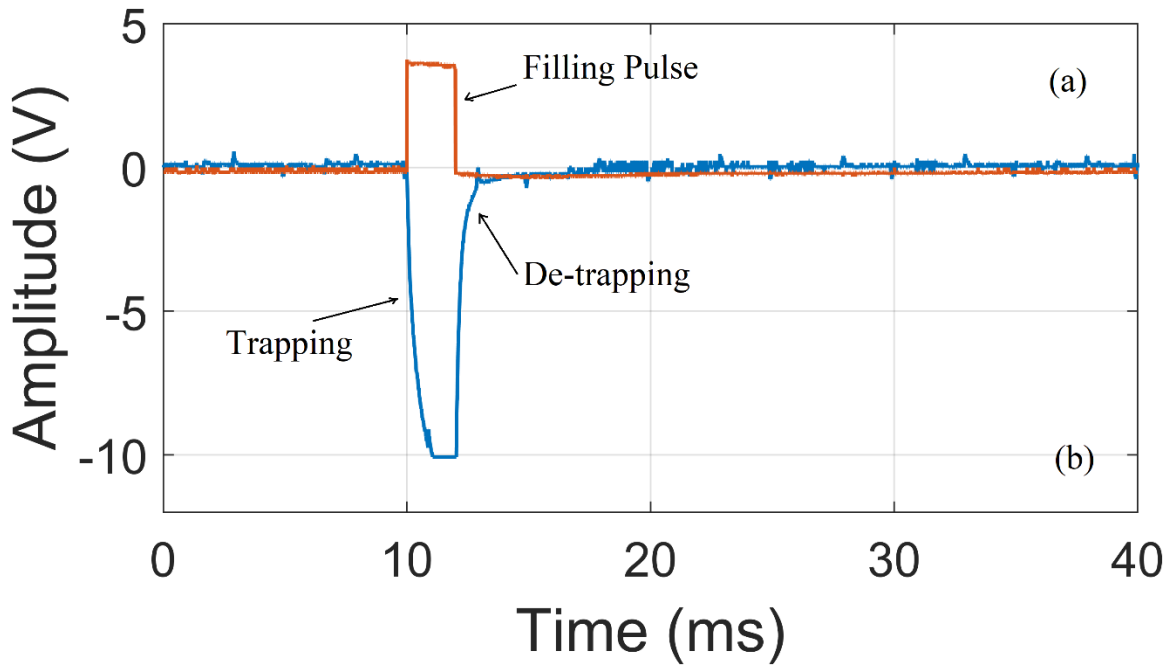


Figure 5.10 Typical function generator output (a) and preamplifier output (b) observed in the oscilloscope during the PICTS measurements.

Upon acquiring a waveform, the LabVIEW program first smooths the waveforms using a moving average filter. From the derivative of the filtered waveform, the program acquires both the initial rise and initial fall indices corresponding to the start of the photoinduced current and fall of the trap emission current. Using up to 37 different t_1 - t_2 pairs, the program calculates the difference spectra and normalizes them to the steady-state photoinduced current to remove the e_n term from the outside of the exponentials in the PICTS signal. For a single set temperature, the program allows for the collection of up to

a user set number of waveform which will have their individual PICTS signals averaged together for the final recorded value.

Figure 5.10 shows a typical PICTS waveform captured on the GDS-1062A oscilloscope. The slow rise in amplitude of the photoinduced current is due to trapping of charge carriers before reaching steady state. Once the optical source is turned off, the amplitude drops off rapidly as the photoinduced current vanishes leaving behind only the emission current from traps.

5.5 DEEP LEVELS IN NEUTRON IRRADIATED EPILAYERS

The defects in the four detectors were characterized by DLTS, CTS, and PICTS depending on their device properties. N1 and N2, which showed normal C-V characteristics for 4H-SiC SBDs, were characterized by traditional capacitance DLTS from 80-790 K using a -2 V steady-state bias and a 0 V filling pulse applied every second for 1 ms. Detector N3 had an abnormally low capacitance, but still showed rectifying characteristics and low leakage current and, therefore, was chosen to be characterized by CTS over the same temperature range. Per Eqn. 5.3, the emission current is directly proportional to the width of the window Δx defined as the difference between the depletion width at the steady-state bias and the depletion width during the filling pulse. Thus, the signal strength will be maximized at the highest possible steady-state reverse bias for the DDS-12 of -12 V and filling pulse equal to the built-in voltage V_{bi} . However, applying a forward bias is considered risky—especially at elevated temperature—because the high forward bias current could damage the sensitive electronic components of the DDS-12

system. Thus, a 0 V, 1 ms filling pulse was selected in conjunction with the -12 V steady-state bias corresponding to $\Delta x \approx 10 \mu\text{m}$.

N4, which behaved as a semi-insulator, was characterized by PICTS using a 365 nm wavelength ultraviolet directional LED pulsed for 2 ms at a 22 Hz frequency over the temperature range 80-700 K wherein the photoinduced current was generated with a -12 V applied bias. The attenuation length of 365 nm UV photons is $>50 \mu\text{m}$ in 4H-SiC [125] ensuring that charge carrier generation occurs within the epitaxial layer. A limitation of the PICTS technique is that it cannot differentiate between electron and hole traps unless charge pairs are generated close to the surface of the detector limiting the volume that the opposite polarity charge carrier can occupy. Using 7.83 ns as the lifetime, the width of the volume containing the trapped electrons would be $36 \mu\text{m}$ allowing both electron and hole volumes to be fully filled. However, in 4H-SiC, μ_n is an order of magnitude greater than μ_p which makes any measured peak more likely to be an electron trap than a hole trap.

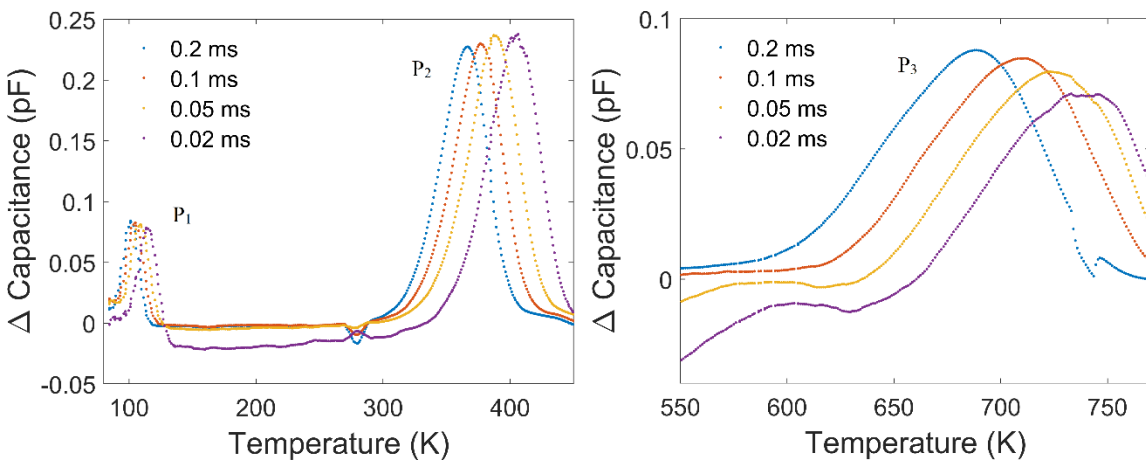


Figure 5.11 DLTS spectrum of neutron irradiated detector N1 fabricated on epilayers irradiated at fluences $\sim 10^{10} \text{ cm}^{-2}$.

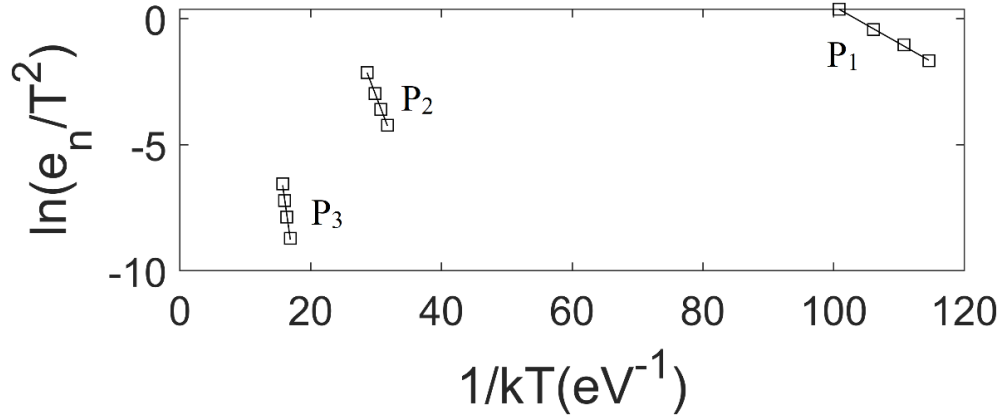


Figure 5.12 Arrhenius plots for the DLTS spectrum of neutron irradiated detector N1 fabricated on epilayers irradiated at neutron fluences $\sim 10^{10} \text{ cm}^{-2}$.

Table 5.3 Trap parameters obtained from the DLTS measurements of detector N1.

Peak	$E_c - E_T$ (eV)	σ_n (cm^2)	N_t (cm^{-3})	Possible Trap Identity
P ₁	0.15	1.2×10^{-15}	4.6×10^{11}	Ti (c)
P ₂	0.68	9.2×10^{-15}	1.2×10^{12}	$Z_{1/2}$
P ₃	1.84	1.5×10^{-12}	3.6×10^{11}	Unidentified

Figure 5.11 shows the DLTS spectrum of detector N1 which had 3 clearly resolvable peaks with parameters recorded in Table 5.3. The first two peaks are the titanium and $Z_{1/2}$ peaks that appear in all as-grown epitaxial layers (Sec. 3.4). The $Z_{1/2}$ center had a relatively typical trap concentration and capture cross-section of $1.2 \times 10^{12} \text{ cm}^{-3}$ and 10^{-15} - 10^{-14} cm^2 , respectively, which explains why the detector resolution is unperturbed at a low neutron dose of 10^{10} cm^{-2} . At first glance, the last peak appears to be $\text{EH}_{6/7}$; however, the extracted energy level from the Arrhenius plot in Figure 5.12 was 1.84 eV below the conduction band edge. The energy is close to the EP2 level observed in electron beam irradiation p-type 4H-SiC [89] and was suspected of being an interstitial defect—particular a carbon interstitial—for its instability under low temperature annealing. However, its

capture cross-section (10^{-12} cm^2) is two orders of magnitude larger than EP2. The large cross-section of 10^{-12} cm^2 implies that the originating point defect has a high positive charge.

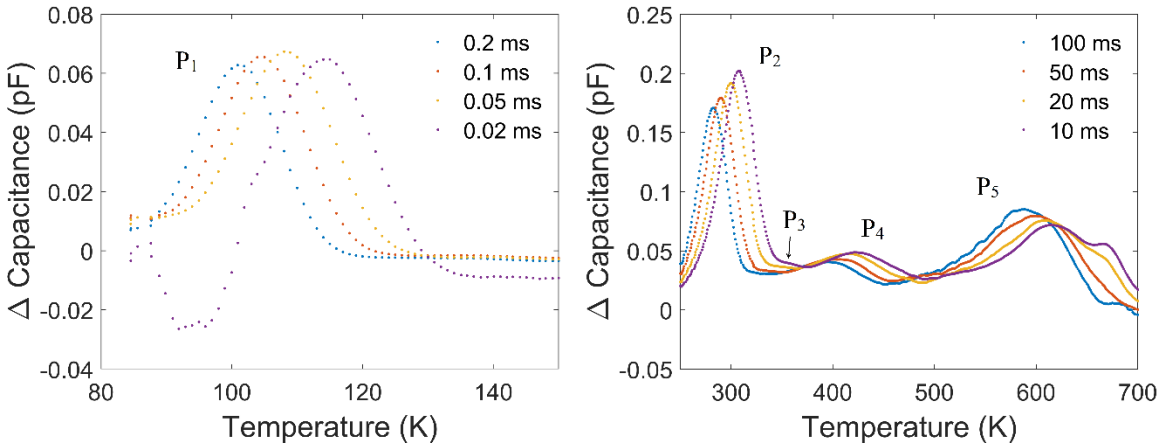


Figure 5.13 DLTS spectrum of neutron irradiated detector N2 fabricated on epilayers irradiated at fluences $\sim 10^{11} \text{ cm}^{-2}$.

N2 manifested two additional peaks in its DLTS spectra (Figure 5.13) compared to N1. The Arrhenius plots and the trap parameters are shown in Figure 5.14 and listed in Table 5.4, respectively. Ti (c) and $Z_{1/2}$ showed no significant changes between the two detectors and appear unaffected by neutron fluence. The first of the new peaks at 0.76 eV is most likely the S_2 center corresponding to the $(-1|-2)$ transition of the silicon vacancy [126]. The second new peak at 1.23 eV is normally labeled as EH_5 and is thought to correlate with carbon antisite-vacancy (CAV) complexes resulting from neighboring carbon atom migrating and occupying silicon vacancies [127, 128]. However, DFT calculations suggest that under n-type conditions, the silicon vacancy is the more metastable state between the two [128]. Proton irradiation studies imply that it could form more readily—especially at elevated temperatures—as introduced acceptors push down the

fermi level [129]. The unidentified deep level had a slightly larger capture cross-section and trap concentration than was seen in N1. If the unidentified peak was exclusively derived from the new peak formed by irradiation, its concentration would be expected to have increased by a full order of magnitude from 10^{10} cm^{-2} to 10^{11} cm^{-2} . Since the peak is relatively broad, it is likely that it corresponds to the overlap of multiple peaks including the normally observed $\text{EH}_{6/7}$.

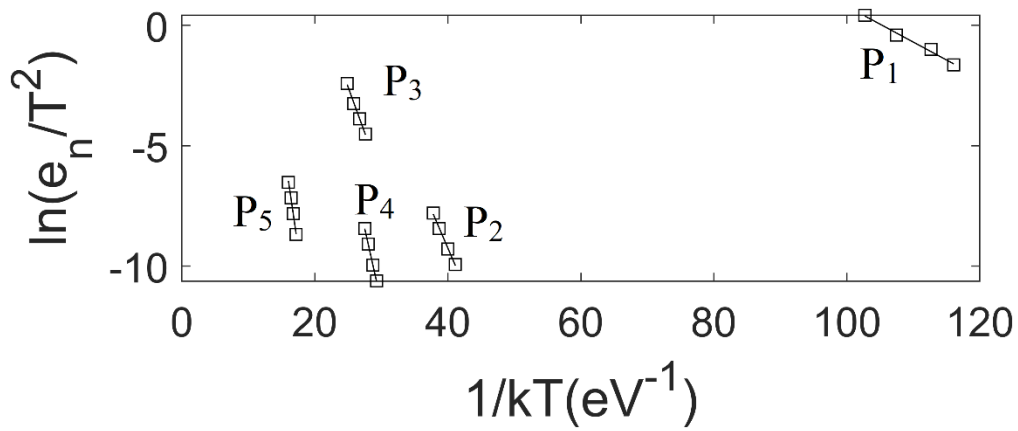


Figure 5.14 Arrhenius plots for the DLTS spectrum of neutron irradiated detector N2 fabricated on epilayers irradiated at neutron fluences $\sim 10^{11} \text{ cm}^{-2}$.

Table 5.4 Trap parameters obtained from the DLTS measurements of detector N2.

Peak	$E_c - E_T$ (eV)	σ_n (cm^2)	N_t (cm^{-3})	Possible Trap Identity
P ₁	0.15	1.9×10^{-15}	4.2×10^{11}	Ti (c)
P ₂	0.68	3.9×10^{-15}	1.1×10^{12}	Z _{1/2}
P ₃	0.76	3.8×10^{-15}	1.9×10^{11}	S ₂
P ₄	1.23	3.4×10^{-11}	2.4×10^{11}	EH ₅ , Ci1
P ₅	1.90	7.7×10^{-12}	5.7×10^{11}	Unidentified

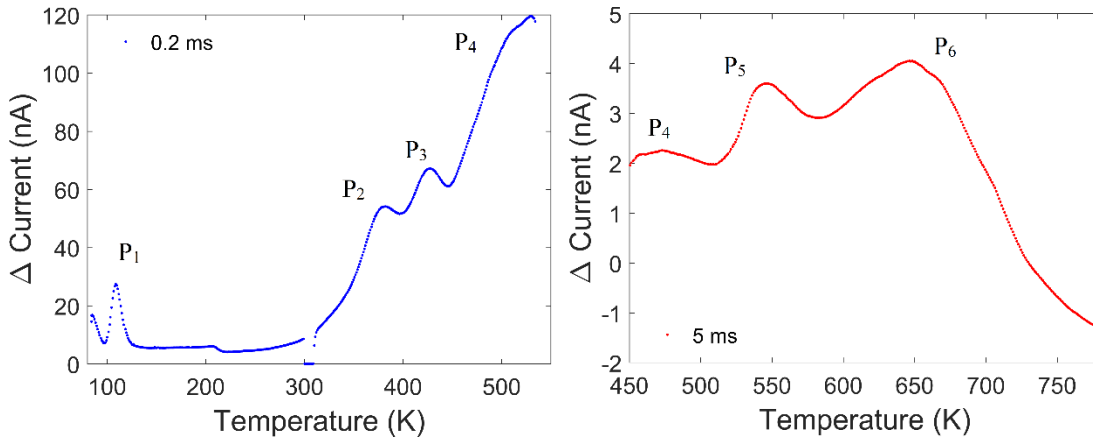


Figure 5.15 CTS spectrum of neutron irradiated detector N3 fabricated on epilayers irradiated at fluences $\sim 10^{12} \text{ cm}^{-2}$.

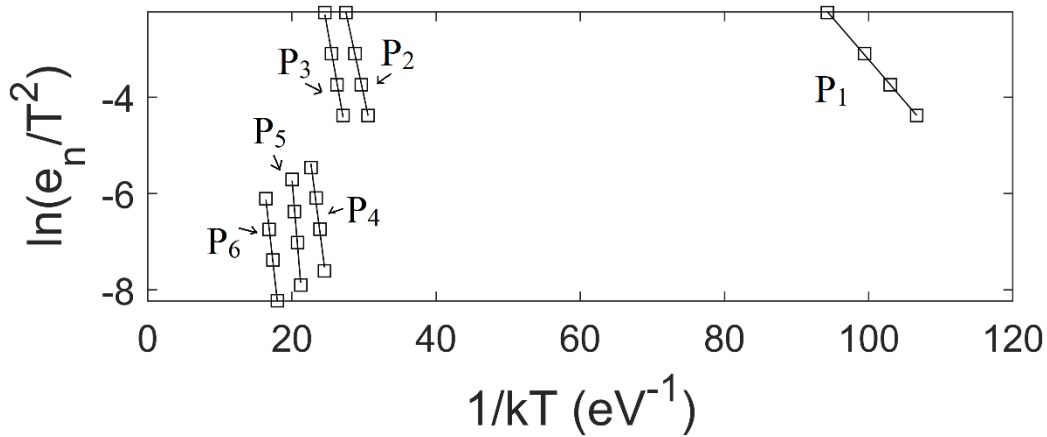


Figure 5.16 Arrhenius plots for the CTS spectra of neutron irradiated detector N3 fabricated on epilayers irradiated at neutron fluences $\sim 10^{12} \text{ cm}^{-2}$.

The CTS spectra and Arrhenius plots for detector N3 are presented in Figures 5.15 and 5.16, respectively, while the trap parameters are given in Table 5.5. The spectrum has all the same peaks as N2 except for the inclusion of an additional peak at 1.33 eV below the conduction band edge. Based on its capture cross-section and temperature position, this could be the EH_6 component peak of $\text{EH}_{6/7}$ or the Ci1 peak potentially derived from chlorine impurities introduced during CVD growth as byproduct of using dichlorosilylene

as the silicon precursor [130]. The trap concentrations of the S₂ center, EH₅, and unidentified center all grew by approximately one order of magnitude compared to N2.

Table 5.5 Trap parameters obtained from the CTS measurements of detector N3.

Peak	$E_c - E_T$ (eV)	σ_n (cm ²)	N_t (cm ⁻³)	Possible Trap Identity
P ₁	0.17	4.1×10^{-16}	6.5×10^{11}	Ti (c)
P ₂	0.69	6.7×10^{-15}	1.1×10^{12}	Z _{1/2}
P ₃	0.84	3.0×10^{-14}	1.5×10^{12}	S ₂
P ₄	1.14	2.2×10^{-13}	1.3×10^{12}	EH ₅
P ₅	1.79	3.6×10^{-9}	2.1×10^{12}	Unidentified
P ₆	1.33	2.0×10^{-15}	2.5×10^{12}	EH ₆

Only two peaks (parameters recorded in Table 5.6) could be fully resolved from the spectrum of N4 shown in Figure 5.17. At first glance, both peaks appear to be the same trapping center; however, the Arrhenius plot in Figure 5.18 revealed the presence of two linear regions indicating two different trap levels being resolved at the same temperature range albeit with different correlators. The first linear region corresponded to Z_{1/2} and had a concentration of 1.5×10^{12} cm⁻³ whereas the second corresponded to the S₂ center and had a concentration of 1.3×10^{13} cm⁻³. Brodar *et al.* defined the defect introduction rate as the differential change in trap concentration with neutron flux [117]. For the present irradiations, this was calculated to be 0.27 cm⁻¹ which is 3 times lower than reported in the previous study. However, based on just the fast neutron fluence, it was 2.08 cm⁻¹. To the left of the Z_{1/2} was a continuum of lower energy peaks that could not be resolved. Based on the proton irradiation studies by Karsthof *et al.*, these could be a continuum of CAV complexes which should produce four distinct energy levels ranging from 0.3-0.5 eV [129].

At room temperature, these shallow levels would have emission times in the range of μs to ms which would correlate with the rightward tailing of detector N4's ^{241}Am pulse height spectrum.

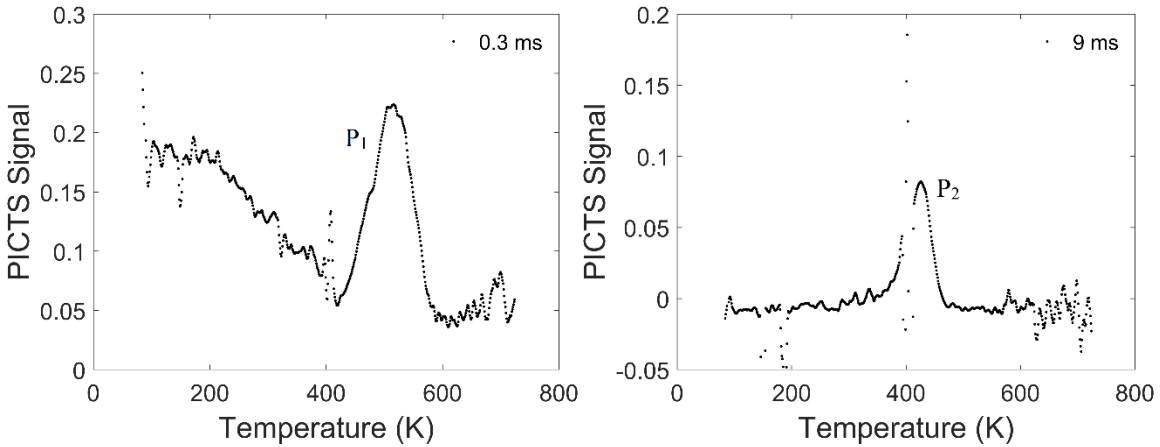


Figure 5.17 PICTS spectrum of neutron irradiated detector N4 fabricated on epilayers irradiated at fluences $\sim 10^{13} \text{ cm}^{-2}$ using 0.3 and 9 ms initial delays.

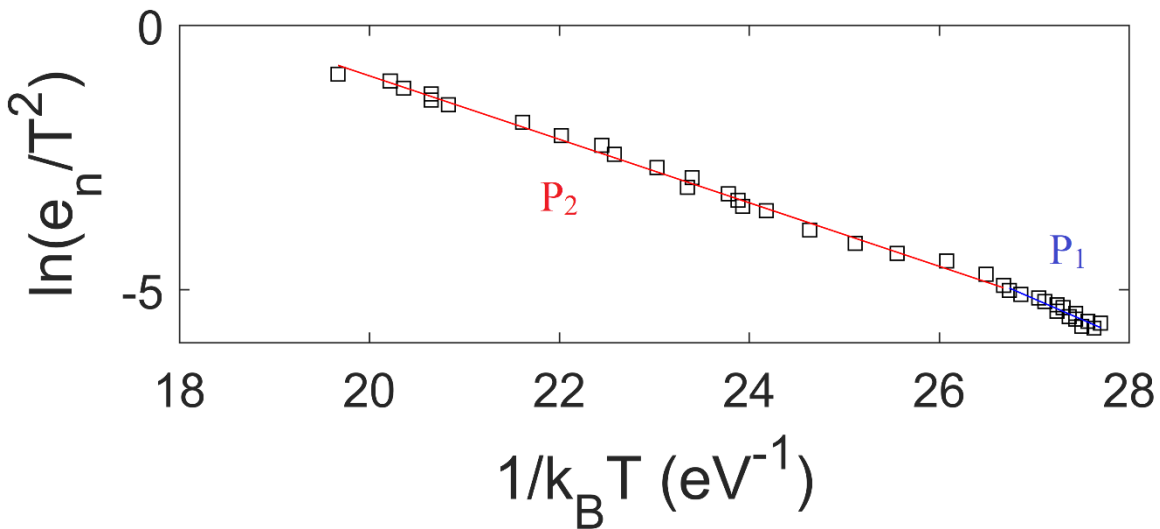


Figure 5.18 Arrhenius plot for the PICTS spectrum of neutron irradiated detector N4 fabricated on epilayers irradiated at neutron fluences $\sim 10^{13} \text{ cm}^{-2}$.

Table 5.6 Trap parameters obtained from the PICTS measurements of detector N4.

Peak	$E_c - E_T$ (eV)	σ_n (cm ²)	N_t (cm ⁻³)	Possible Trap Identity
P ₁	0.60	1.9×10^{-17}	1.5×10^{12}	Z _{1/2}
P ₂	0.78	2.2×10^{-15}	1.3×10^{13}	S ₂

Fast neutrons have energies greater 1 MeV which is sufficiently high enough to dislodge an atom upon collision regardless of its displacement energy, and therefore, the individual neutron cross-sections of the component atoms will determine which types of defects are more likely to form. Particles can scatter elastically (no energy loss), inelastically (partial energy loss), or non-elastically (complete energy loss). Since no energy is lost during elastic scattering, the types of cross-sections that are most likely to cause displacements are inelastic and non-elastic scattering. According to the Evaluated Nuclear Data File (ENDF/B-VIII) available at Brookhaven National Laboratory (BNL) [131], silicon has in-elastic and non-elastic cross-sections of ~ 0.1 barn (10^{-25} cm²) at around 1-3 MeV whereas carbon is $\sim 10^{-5}$ barn in the same range. Therefore, silicon displacement-related defects are significantly more likely to form than carbon displacement-related defects.

Silicon displacement defects fall into three general categories of point defects. The most obvious two are the silicon interstitial and the silicon vacancy which correspond to the dislodged atom and the empty space it left behind, respectively. The third is the CAV center which forms when a neighboring carbon atom diffuses into a silicon vacancy. There are four of such defects corresponding to movement from the carbon hexagonal (h) or cubic (k) site into the silicon hexagonal (h) or cubic (k) site. Figure 5.19 shows the formation

energy phase diagram for these three types of defects calculated using hybrid density functionals and the FNV correction. More details on the computational methods can be found in Sec. 3.2. Silicon vacancies are well known to produce defect levels around 0-7-0.8 eV (S_2) centers and is the most likely identity of the similar defect observed in UofSC's neutron irradiated epilayers [88, 129]. As reported elsewhere [128], under n-type doping conditions the formation energy of silicon vacancies is much lower than CAV complexes implying that the adjacent carbon atom prefers to remain in the silicon vacancy configuration than to migrate into unoccupied silicon site. Additionally, the computed energy levels of CAV centers are deeper than the typically reported values of EH₅.

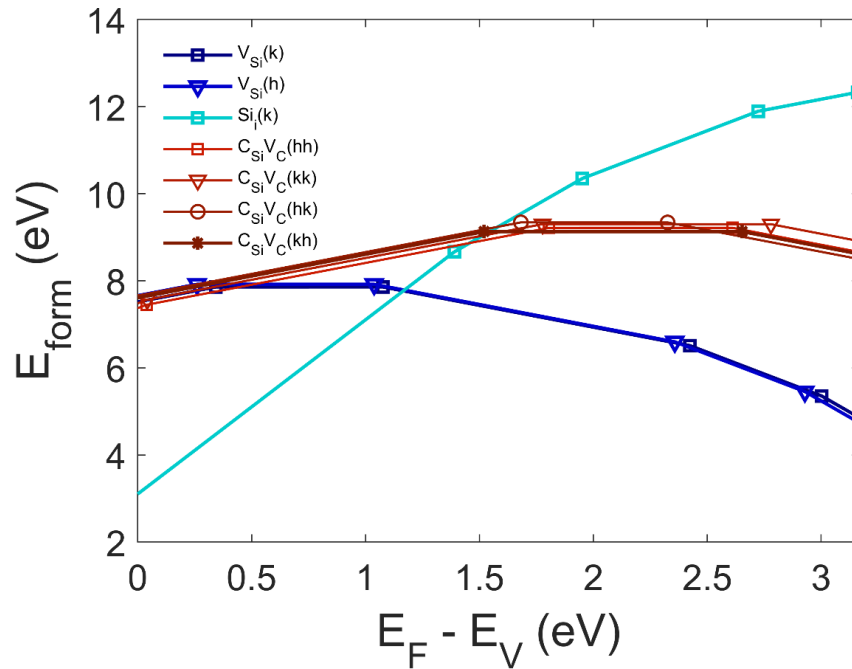


Figure 5.19 Formation energies of silicon displacement-related defects in 4H-SiC using HSE06 hybrid pseudopotentials in C-rich conditions.

Regardless, for any silicon vacancy or CAV center, there should be equal number of silicon interstitials. These defects will remain until they are annealed and reoccupy the

silicon sites effectively eliminating both sets of defects. From our calculations, the interstitial occupying the cubic site ($\text{Si}_i(\text{k})$) produces three deep levels and one shallow level with acceptor like characteristics. The first level at $E_V + 1.40$ eV agrees with the reported value for the unidentified deep level and corresponds to a charge transition state of $(+4|+3)$ which would explain the large capture cross-section of the level at $E_C - 1.8$ eV. The $(+3|+2)$ transition overlaps with the reported value of EH_5 in the present studies. Like the unidentified level, EH_5 had a large capture cross-section of 10^{-13} cm^2 which could be explained by the $+3$ charge state. The overall charge profile of the silicon interstitial suggests that it acts as an electron acceptor and could be one of the sources of donor compensation reported in neutron irradiated epilayers.

Table 5.7 Transition levels of silicon displacement-related defects in 4H-SiC measured from the valence band maximum.

Defect	(+4 +3)	(+3 +2)	(+2 +1)	(+1 0)	(0 -1)	(-1 -2)	(-2 -3)
$\text{V}_{\text{Si}}(\text{k})$				0.34	1.07	2.42	3.00
$\text{V}_{\text{Si}}(\text{h})$				0.25	1.04	2.36	2.93
$\text{C}_{\text{Si}}\text{V}_{\text{C}}(\text{hh})$				1.52	2.65		
$\text{C}_{\text{Si}}\text{V}_{\text{C}}(\text{kk})$			0.04	1.77	2.78		
$\text{C}_{\text{Si}}\text{V}_{\text{C}}(\text{hk})$				1.68	2.33		
$\text{C}_{\text{Si}}\text{V}_{\text{C}}(\text{kh})$			0.04	1.80	2.61		
$\text{Si}_i(\text{k})$	1.40	1.95	2.72	3.16			

5.6 CONCLUSION

Four 4H-SiC SBD radiation detectors have been fabricated on 4H-SiC epitaxial layers irradiated up to $\sim 10^{13}$ cm^{-2} . Radiation detection measurements showed consistent

energy resolutions of 28-29 keV (0.5%) for 5486 keV alpha particles for the detectors irradiated with the lowest dose (10^{10} and 10^{11} cm⁻²). The energy resolution marginally degraded to 42 keV for the detector irradiated at fluences of 10^{12} cm⁻². Modeling the charge collected with the drift-diffusion model revealed a significant decline in the minority carrier diffusion length from 10 to 2.6 μ m implying an increase in hole trapping centers. The most heavily irradiated detector (10^{13} cm⁻²) exhibited semi-insulating behavior which was correlated with donor compensation introduced by deep levels. Despite this, the detector was still able to achieve a resolution of 1.76%. Defects studies on the four detectors revealed the presence of three deep levels that do not appear in as-grown epitaxial layers. The levels showed increasing concentration with neutron dose which correlated well with the decline in the detector resolution. The first level at 0.7-0.8 eV was labeled as S₂ corresponding to silicon vacancies formed from the displacement of a silicon atom from its crystalline lattice site. The second level was the EH₅ peak at 1.1-1.2 eV and the third was an unidentified midgap level located 1.8 eV below the conduction band edge. EH₅ is normally associated with CAV centers; however, comparison with ab initio calculations suggests that both EH₅ and the unidentified defect may be two different charge states of the silicon interstitial which is guaranteed to form alongside silicon vacancies in a displacement event. Silicon interstitials also displayed acceptor like characteristics and could be the source of the donor compensation observed in the heavily irradiated detector.

CHAPTER 6

CONCLUSION, DISSEMINATION OF WORK, AND FUTURE WORK

6.1 FINAL CONCLUSIONS

Versatile radiation detectors which can detect a wide variety of both charged and neutral radioactive particles in environments with high or rapidly fluctuating temperatures and high background radiation fields are needed for NASA space missions, high energy physics experiments, nuclear waste safeguarding, and reactor core monitoring. Conventional radiation detectors such as HPGe, Si, or CZT are inoperable within these harsh environments due to their insufficient bandgaps and high atomic numbers. As a result, 4H-SiC Schottky barrier diodes (SBD) radiation detectors have become the top contender for harsh environment detection of charged radiation. However, 4H-SiC's low atomic numbers—the very properties that make it resilient to radiation fields—also makes it nearly transparent to uncharged radiations such as gamma rays, a limitation which lessens the thicker the active volume of the device is. Developments in 4H-SiC epilayer technology in recent years has allowed for thicker epilayers up to 250 μm with low concentrations of intrinsic defects paving the way for the development of dynamic 4H-SiC detectors.

In this dissertation, Ni/4H-SiC SBD radiation detectors were fabricated on epilayers up to 250 μm thick—the thickest reported to date—and characterized for their room temperature electronic properties and radiation detection performance. The first set

of evaluated detectors had barrier heights > 1.3 eV, ideality factors < 1.1 , and demonstrated consistently low leakage current density < 300 pA cm⁻² even at 800 V reverse bias. Despite this, the current over the barrier was determined to be more than expected, and fitting $\ln J/E_m$ against the $\sqrt{E_m}$ revealed the leakage current was mostly trap-assisted through Poole-Frenkel emission which could be significant at the full depletion biases of 5-10 kV. Radiation detection measurements were performed using a ²⁴¹Am calibrated alpha source. Pulse height spectrometry measurements with ²⁴¹Am represent the first step in the characterization of any radiation detector and serves as the main qualifier for detector performance. All three detectors demonstrated consistently high 5486 keV resolutions $< 0.5\%$ FWHM and had clearly resolvable peaks for 5338 keV and 5442 keV. Although, the resolution was determined from noise measurements with a precision pulser to be limited by the detectors themselves.

When performance is limited by the detector, this mostly refers to trapping of charge carriers by point defects and can be quantified by how quickly these trapping centers can capture charges. In 4H-SiC, the most significant electron trapping center at room temperature is the $Z_{1/2}$ defect with an energy level of 0.6-0.7 eV below the conduction band which mostly correlates with the (0|-1) charge state transition of the carbon vacancy. To demonstrate the effect of trapping on radiation detection performance, three new detectors were fabricated on epilayers of thickness 50, 150, and 250 μm which had optimal resolutions of 2.0 %, 0.8 %, and 0.63 %, respectively. Fitting the charge collected to a drift-diffusion model revealed minority carrier diffusion lengths of 16, 10, and 9.2 μm , respectively, suggesting that the optimal resolution was not limited by minority carrier trapping. Rather, deep level transient spectroscopy (DLTS) measurements revealed that

detector energy resolution had a strong correlation with the trapping rate of $Z_{1/2}$ which is proportional to the product of the trap concentration and trap cross-section. In summary, the detectors with lower $Z_{1/2}$ trapping rates had better resolutions.

To investigate how detector performance might change under harsh environment conditions, temperature dependent current-voltage (I-V-T) measurements were conducted on a detector fabricated on 150 μm epilayers. This detector had promising electronic properties such as a high average barrier height of 2.16 eV and low room temperature leakage currents $\sim\text{pA}$ at 200 V reverse making it ideal for characterizing its current transport mechanisms. At 400 K, it was determined that the leakage current was predominantly trap-assisted by $Z_{1/2}$. As a neutral trap, $Z_{1/2}$ incurs no barrier lowering allowing for mild, linear current growth with the applied electric field. At 450 and 500 K, the current started to grow exponentially at high bias which was determined to be due to Schottky barrier lowering of a low barrier patch in the M-S interface. Low barrier patches are most likely derived from dislocation defects propagated from the substrate. At 600 K, the current transport mechanism approached Poole-Frenkel lowering potentially from the activation of positively charged $\text{EH}_{6/7}$. Overall, this study showed how both deep levels and nonidealities in the surface barrier can result in excess detector leakage currents which will degrade detector signal-to-ratio at elevated temperatures.

Finally, the radiation tolerance of high quality 250 μm 4H-SiC SBD radiation detectors was investigated through irradiation studies with fast neutrons. Detectors showed steady resolutions of 0.5% up to neutron fluences of 10^{11} cm^{-2} before degrading to 0.8% and 1.76% at 10^{12} and 10^{13} , respectively. Combined DLTS and density functional theory studies revealed that this degradation originates from silicon displacement-related

defects—silicon vacancies and silicon interstitials—which form deep levels 0.7-0.8, 1.2, and 1.8 eV below the conduction band edge.

6.2 DISSEMINATION OF WORK

1. J. W. Kleppinger, S. K. Chaudhuri, O. Karadavut, R. Nag, D. L. P. Watson, D. S. McGregor, and K. C. Mandal, “Deep-level transient spectroscopy and radiation detection performance studies on neutron irradiated 250- μm thick 4H-SiC epitaxial layers,” IEEE Transactions on Nuclear Science, 2022 (Minor Revisions, Resubmitted 03/12/2022).
2. O. Karadavut, S. K. Chaudhuri, J. W. Kleppinger, R. Nag, and K. C. Mandal, “Effect of oxide layer growth conditions on radiation detection performance of Ni/SiO₂/epi-4H-SiC MOS capacitors,” Journal of Crystal Growth, vol. 584, pp. 126566-1-7, 2022.
3. J. W. Kleppinger, S. K. Chaudhuri, O. Karadavut, R. Nag, and K. C. Mandal, “Influence of carrier trapping on radiation detection properties in CVD grown 4H-SiC epitaxial layers with varying thickness up to 250 μm ,” Journal of Crystal Growth, vol. 583, pp. 126532-1-6, 2022.
4. S. K. Chaudhuri, J. W. Kleppinger, O. Karadavut, R. Nag, R. Panta, F. Agostinelli, A. Sheth, U. N. Roy, R. B. James, and K. C. Mandal, “Synthesis of CdZnTeSe single crystals for room temperature radiation detector fabrication: mitigation of hole trapping effects using a convolutional neural network,” Journal of Materials Science: Materials in Electronics, vol. 33, pp. 1452-1463, 2022.

5. R. Nag, S. K. Chaudhuri, J. W. Kleppinger, O. Karadavut, and K. C. Mandal, "Characterization of vertical Bridgman grown $\text{Cd}_{0.9}\text{Zn}_{0.1}\text{Te}_{0.97}\text{Se}_{0.03}$ single crystal for room-temperature radiation detection," *Journal of Materials Science: Materials in Electronics*, vol. 32, pp. 26740-26749, 2021.
6. S. K. Chaudhuri, O. Karadavut, J. W. Kleppinger, and K. C. Mandal, "High-resolution radiation detection using $\text{Ni}/\text{SiO}_2/\text{n-4H-SiC}$ vertical metal-oxide-semiconductor capacitor," *Journal of Applied Physics*, vol. 130, pp. 074501-1-9, 2021.
7. J. W. Kleppinger, S. K. Chaudhuri, O. Karadavut, and K. C. Mandal, "Role of deep levels and barrier height lowering in current-flow mechanism in 150 μm thick epitaxial n-type 4H-SiC Schottky barrier radiation detectors," *Applied Physics Letters*, vol. 119, pp. 063502-1-6, 2021.
8. S. K. Chaudhuri, J. W. Kleppinger, O. Karadavut, R. Nag, K. C. Mandal, "Quaternary Semiconductor $\text{Cd}_{1-x}\text{Zn}_x\text{Te}_{1-y}\text{Se}_y$ for High-Resolution, Room-Temperature Gamma-Ray Detection", *Crystals*, vol. 11, pp. 827-1-22, 2021.
9. Sandeep K. Chaudhuri, Joshua W. Kleppinger, Ritwik Nag, Kaushik Roy, Rojina Panta, Forest Agostinelli, Amit Sheth, Utpal N. Roy, Ralph B. James, and Krishna C. Mandal "A CdZnTeSe gamma spectrometer trained by deep convolutional neural network for radioisotope identification", *Proc. SPIE*, vol. 11838, pp. 1183806-1-10, 2021.
10. Joshua W. Kleppinger, Omerfaruk Karadavut, Ritwik Nag, Sandeep K. Chaudhuri, and Krishna C. Mandal "High-resolution 4H-SiC Schottky barrier radiation

- detectors on 250 μm epitaxial layers for harsh environment applications", Proc. SPIE, vol. 11838, pp. 1183816-1-11, 2021.
11. OmerFaruk Karadavut, Joshua W. Kleppinger, Ritwik Nag, Sandeep K. Chaudhuri, and Krishna C. Mandal "Observation of minority carrier traps using C-DLTS in Au/SiO₂/n-4H-SiC vertical MOS capacitor", Proc. SPIE, vol. 11838, pp. 1183815-1-8, 2021.
 12. J. W. Kleppinger, S. K. Chaudhuri, O. Karadavut, and K. C. Mandal, "Defect characterization and charge transport measurements in high-resolution Ni/n-4H-SiC Schottky barrier radiation detectors fabricated on 250 μm epitaxial layers," J. Appl. Phys., vol. 129, pp. 244501-1-10, 2021.
 13. J. W. Kleppinger, S. K. Chaudhuri, U. N. Roy, R. B. James and K. C. Mandal, "Growth of Cd_{0.9}Zn_{0.1}Te_{1-y}Se_y single crystals for room-temperature gamma ray detection," in IEEE Transactions on Nuclear Science, vol. 68, pp. 2429-2434, 2021.
 14. S. K. Chaudhuri, J. W. Kleppinger, O. Karadavut and K. C. Mandal, "Behavioral contrast of electron and hole transport in high-resolution diamond detectors: a biparametric correlation study," IEEE Electron Device Letters, vol. 42, pp. 200-203, 2021.
 15. J. W. Kleppinger, S. K. Chaudhuri, O. Karadavut and K. C. Mandal, "First principle defect analysis in 150 μm 4H-SiC epitaxial layer Schottky barrier detectors," 2020 IEEE Nuclear Science Symposium and Medical Imaging Conference (NSS/MIC), pp. 1-6, 2020.
 16. S. K. Chaudhuri, M. Sajjad, J. W. Kleppinger and K. C. Mandal, "Real-time pulse height spectroscopy using Cd_{0.9}Zn_{0.1}Te coplanar grid digital spectrometer," 2020

- IEEE Nuclear Science Symposium and Medical Imaging Conference (NSS/MIC), pp. 1-5, 2020.
17. S. K. Chaudhuri, J. W. Kleppinger, and K. C. Mandal, "Radiation detection using fully depleted 50 μm thick Ni/n-4H-SiC epitaxial layer Schottky diodes with ultra-low concentration of $Z_{1/2}$ and $\text{EH}_{6/7}$ deep defects", Journal of Applied Physics, vol. 128, pp. 114501-1-9, 2020.
 18. J. W. Kleppinger, S. K. Chaudhuri, and K. C. Mandal, "Thick 4H-SiC epitaxial detectors for high-resolution radiation detection in harsh environment", Proc. SPIE, vol. 11494, pp. 132-144, 2020.
 19. M. Sajjad, S. K. Chaudhuri, J. W. Kleppinger, O. Karadavut, and K. C. Mandal "Investigation on $\text{Cd}_{0.9}\text{Zn}_{0.1}\text{Te}_{1-y}\text{Se}_y$ single crystals grown by vertical Bridgman technique for high-energy gamma radiation detectors", Proc. SPIE, vol. 11494, pp. 114941F-1-12, Aug. 2020.
 20. S. K. Chaudhuri, M. Sajjad, J. W. Kleppinger and K. C. Mandal, "Correlation of space charge limited current and γ -ray response of $\text{Cd}_x\text{Zn}_{1-x}\text{Te}_{1-y}\text{Se}_y$ room-temperature radiation detectors," IEEE Electron Device Letters, vol. 41, pp. 1336-1339, 2020.
 21. M. Sajjad, S. K. Chaudhuri, J. W. Kleppinger and K. C. Mandal, "Growth of large-area $\text{Cd}_{0.9}\text{Zn}_{0.1}\text{Te}$ single crystals and fabrication of pixelated guard-ring detector for room-temperature γ -ray detection," IEEE Transactions on Nuclear Science, vol. 67, pp. 1946-1951, 2020.

22. S. K. Chaudhuri, M. Sajjad, J. W. Kleppinger and K. C. Mandal, "Charge transport properties in CdZnTeSe semiconductor room-temperature γ -ray detectors," *Journal of Applied Physics*, vol. 127, pp. 245706-1-8, 2020.
23. K. C. Mandal, J. W. Kleppinger, S. K. Chaudhuri, "Advances in high-resolution radiation detection using 4H-SiC epitaxial layer devices". *Micromachines*, vol. 11, 254, 27 pages, 2020.
24. J. W. Kleppinger, Y. Pershin, Z. Rak, and K. C. Mandal "Investigation on origin of Ru-induced deep-level defects in 4H-SiC epilayer based Schottky diodes by DLTS and theoretical calculations", *Proc. SPIE*, vol. 11114, pp. 111140T-1-11, 2019.
25. K. C. Mandal, J. W. Kleppinger, and M. Sajjad "4H-SiC epitaxial Schottky detectors: deep-level transient spectroscopy (DLTS) and pulse height spectroscopy (PHS) measurements", *Proc. SPIE*, vol. 11114, pp. 111140N-1-9, 2019.
26. M. Sajjad, J. W. Kleppinger, and K. C. Mandal "Crystal growth, characterization, and fabrication of large-area Cd_{0.9}Zn_{0.1}Te pixelated detectors for high-energy gamma-ray detectors", *Proc. SPIE*, vol. 11114, pp. 111141T-1-12, 2019.

6.3 FUTURE WORK

- The intent for using 250 μm epilayers is to be able to collect uncharged radiation such as gamma rays or x-rays. However, maximizing the gamma ray detection probability requires the detectors to be fully depleted requiring extremely high biases well exceeding 1000 Volts inducing large leakage currents which can degrade the SNR of the detector. A potential future study is to investigate how different passivation techniques or device structure may affect the leakage current

- often observed in 4H-SiC detectors. Once the leakage current is effectively controlled, the next stage would be studying the device properties under full depletion followed by x-ray and low energy gamma spectroscopic measurements.
- While the leakage current variation with temperature has been studied, spectroscopic measurements conducted at both high and low temperatures are also required.
 - The defects introduced by fast neutron irradiation are suspected to be related to silicon vacancies and silicon interstitials. Interstitial defects are almost always unstable and anneal out at relatively low temperatures. These silicon atoms ideally will diffuse back into their formally occupied sites effectively eliminating both defects. The annealing mechanism of these defect needs to be investigated through a combined isochronal annealing and DLTS study.

REFERENCES

- [1] NASA. "“NASA’s Lunar Exploration Program Overview,” Sept. 2020. [Online]:https://www.nasa.gov/sites/default/files/atoms/files/artemis_plan-20200921.pdf."
- [2] J. A. Simpson, "Elemental and isotopic composition of the galactic cosmic rays," *Annu. Rev. Nucl. Part. Sci*, vol. 33, no. 1, pp. 323-382, 1983.
- [3] G. W. McKinney, D. J. Lawrence, T. H. Prettyman, R. C. Elphic, W. C. Feldman, and J. J. Hagerty, "MCNPX benchmark for cosmic ray interactions with the Moon," *J. Geophys. Res: Planets*, vol. 111, no. E6, 2006.
- [4] S. Zhang, F. Wimmer-Schweingruber Robert, J. Yu, C. Wang, Q. Fu, Y. Zou, Y. Sun, C. Wang, D. Hou, I. Böttcher Stephan, S. Burmeister, L. Seimetz, B. Schuster, V. Knierim, G. Shen, B. Yuan, H. Lohf, J. Guo, Z. Xu, L. Freiherr von Forstner Johan, R. Kulkarni Shrinivasrao, H. Xu, C. Xue, J. Li, Z. Zhang, H. Zhang, T. Berger, D. Matthiä, E. Hellweg Christine, X. Hou, J. Cao, Z. Chang, B. Zhang, Y. Chen, H. Geng, and Z. Quan, "First measurements of the radiation dose on the lunar surface," *Sci. Adv.*, vol. 6, no. 39, pp. eaaz1334, 2020.
- [5] J. P. Williams, D. A. Paige, B. T. Greenhagen, and E. Sefton-Nash, "The global surface temperatures of the Moon as measured by the Diviner Lunar Radiometer Experiment," *Icarus*, vol. 283, pp. 300-325, 2017.
- [6] E. Easton, "Dry cask storage of nuclear spent fuel," *Lecture for US Nuclear Regulatory Commission*, 2011.
- [7] P. K. Shukla, B. Dasgupta, S. Chocron, W. Li, and S. Green, *Thermal modeling of a storage cask system capability development*, Contract NRC-02-02-012, 2007.
- [8] F. Nava, G. Bertuccio, A. Cavallini, and E. Vittone, "Silicon carbide and its use as a radiation detector material," *Meas. Sci. Technol.*, vol. 19, no. 10, pp. 102001, 2008.
- [9] G. F. Knoll, *Radiation Detection and Measurement*, 4th ed.: John Wiley & Sons, 2020.
- [10] M. E. Levinshtein, S. L. Rumyantsev, and M. Shur, *Properties of advanced semiconductor materials : GaN, AlN, InN, BN, SiC, SiGe*, New York: Wiley, 2001.

- [11] T. Kimoto, and J. A. Cooper, *Fundamentals of silicon carbide technology: growth, characterization, devices and applications*: John Wiley & Sons, 2014.
- [12] C. J. H. Wort, and R. S. Balmer, "Diamond as an electronic material," *Materials Today*, vol. 11, no. 1, pp. 22-28, 2008.
- [13] I. Capan, "4H-SiC Schottky Barrier Diodes as Radiation Detectors: A Review," *Electronics*, vol. 11, 2022.
- [14] S. K. Chaudhuri, J. W. Kleppinger, O. Karadavut, R. Nag, and K. C. Mandal, "Quaternary Semiconductor $Cd_{1-x}Zn_xTe_{1-y}Se_y$ for High-Resolution, Room-Temperature Gamma-Ray Detection," *Crystals*, vol. 11, no. 7, 2021.
- [15] M. Jackson, B. Bennett, D. Giltneane, S. Babalola, M. F. Ohmes, and A. C. Stowe, "Thermal conductivity studies of CdZnTe with varying Te excess," *Proc. SPIE*, 9968, 2016.
- [16] J. Wang, P. Mulligan, L. Brillson, and L. R. Cao, "Review of using gallium nitride for ionizing radiation detection," *Appl. Phys. Rev.*, vol. 2, no. 3, pp. 031102, 2015.
- [17] M. Gabrysch, E. Marklund, J. Hajdu, D. J. Twitchen, J. Rudati, A. M. Lindenberg, C. Coleman, R. W. Falcone, T. Tschentscher, K. Moffat, P. H. Bucksbaum, J. Als-Nielsen, A. J. Nelson, D. P. Siddons, P. J. Emma, P. Krejcik, H. Schlarb, J. Arthur, S. Brennan, J. Hastings, and J. Isberg, "Formation of secondary electron cascades in single-crystalline plasma-deposited diamond upon exposure to femtosecond x-ray pulses," *J. Appl. Phys.*, vol. 103, no. 6, pp. 064909, 2008.
- [18] P. G. Neudeck, D. J. Spry, M. J. Krasowski, N. F. Prokop, and L. Chen, "Demonstration of 4H-SiC JFET digital ICs across 1000 °C temperature range without change to input voltages," *Mater. Sci. Forum*, vol. 963, pp. 813-817, 2019.
- [19] G. Lucas, and L. Pizzagalli, "Comparison of threshold displacement energies in β -SiC determined by classical potentials and ab initio calculations," *Nucl. Instrum. Method Phys. Res. B*, vol. 229, no. 3, pp. 359-366, 2005.
- [20] K. C. Mandal, J. W. Kleppinger, and S. K. Chaudhuri, "Advances in high-resolution radiation detection using 4H-SiC epitaxial layer devices," *Micromachines*, vol. 11, no. 3, pp. 254, 2020.
- [21] F. H. Ruddy, A. R. Dulloo, J. G. Seidel, F. W. Hantz, and L. R. Grobmyer, "Nuclear Reactor Power Monitoring Using Silicon Carbide Semiconductor Radiation Detectors," *Nucl. Technol.*, vol. 140, no. 2, pp. 198-208, 2002.

- [22] V. V. Kozlovski, A. A. Lebedev, M. E. Levinshtein, S. L. Rumyantsev, and J. W. Palmour, "Electrical and noise properties of proton irradiated 4H-SiC Schottky diodes," *J. Appl. Phys.*, vol. 123, no. 2, pp. 024502, 2018.
- [23] G. Bertuccio, D. Puglisi, L. Torrisi, and C. Lanzieri, "Silicon carbide detector for laser-generated plasma radiation," *5th Workshop on Plasma Production by Laser Ablation (PPLA2011)*, vol. 272, pp. 128-131, 2013.
- [24] N. R. Taylor, Y. Yu, M. Ji, T. Aytug, S. Mahurin, R. Mayes, S. Cetiner, M. P. Paranthaman, D. Ezell, L. R. Cao, and P. C. Joshi, "Thermal and radiation response of 4H-SiC Schottky diodes with direct-write electrical contacts," *Appl. Phys. Lett.*, vol. 116, no. 25, pp. 252108, 2020.
- [25] B. Zat'ko, F. Dubecký, A. Šagátová, K. Sedlačová, and L. Ryc, "High resolution alpha particle detectors based on 4H-SiC epitaxial layer," *J. Instrum.*, vol. 10, no. 04, pp. C04009-C04009, 2015.
- [26] S. K. Chaudhuri, K. J. Zavalla, and K. C. Mandal, "High resolution alpha particle detection using 4H-SiC epitaxial layers: fabrication, characterization, and noise analysis," *Nucl. Instrum. Method Phys. Res. A*, vol. 728, pp. 97-101, 2013.
- [27] B. Povh, K. Rith, C. Scholz, F. Zetsche, and W. Rodejohann, "Particles and Nuclei," *Particles and Nuclei. Series: Graduate Texts in Physics*, 2015.
- [28] M. J. Berger, J. H. Hubbell, S. M. Seltzer, J. Chang, J. S. Coursey, D. S. Zucker, and K. Olsen, "XCOM: Photon Cross Section Database (version 1.5)," [Online] Available: <http://physics.nist.gov/xcom>, [2010].
- [29] J. R. Jenny, S. G. Müller, A. Powell, V. F. Tsvetkov, H. M. Hobgood, R. C. Glass, and C. H. Carter, "High-purity semi-insulating 4H-SiC grown by the seeded-sublimation method," *J. Electron. Mater.*, vol. 31, no. 5, pp. 366-369, 2002.
- [30] W. Cunningham, A. Gouldwell, G. Lamb, J. Scott, K. Mathieson, P. Roy, R. Bates, P. Thornton, K. M. Smith, R. Cusco, M. Glaser, and M. Rahman, "Performance of bulk SiC radiation detectors," *3rd International Workshop on Radiation Imaging Detectors*, vol. 487, no. 1, pp. 33-39, 2002.
- [31] G. Bertuccio, D. Puglisi, A. Pullia, and C. Lanzieri, "X-gamma Ray Spectroscopy With Semi-Insulating 4H-Silicon Carbide," *IEEE Trans. Nucl. Sci.*, vol. 60, no. 2, pp. 1436-1441, 2013.
- [32] P. G. Muzykov, R. M. Krishna, and K. C. Mandal, "Characterization of deep levels in n-type and semi-insulating 4H-SiC epitaxial layers by thermally stimulated current spectroscopy," *J. Appl. Phys.*, vol. 111, no. 1, pp. 014910, 2012.

- [33] G. Bertuccio, R. Casiraghi, and F. Nava, "X-ray detection with epitaxial silicon carbide," *IEEE Trans. Nucl. Sci.*, vol. 48, pp. 232-233, 2001.
- [34] G. Lioliou, N. R. Gemmell, M. Mazzillo, A. Sciuto, and A. M. Barnett, "4H-SiC Schottky diodes with Ni₂Si contacts for X-ray detection," *Nucl. Instrum. Method Phys. Res. A*, vol. 940, pp. 328-336, 2019.
- [35] K. C. Mandal, P. G. Muzykov, S. K. Chaudhuri, and J. R. Terry, "Low energy x-ray and γ -ray detectors fabricated on n-type 4H-SiC epitaxial layer," *IEEE Trans. Nucl. Sci.*, vol. 60, no. 4, pp. 2888-2893, 2013.
- [36] G. Lioliou, H. K. Chan, T. Gohil, K. V. Vassilevski, N. G. Wright, A. B. Horsfall, and A. M. Barnett, "4H-SiC Schottky diode arrays for X-ray detection," *Nucl. Instrum. Method Phys. Res. A*, vol. 840, pp. 145-152, 2016.
- [37] B. G. Streetman, and S. Banerjee, *Solid state electronic devices / Ben G. Streetman and Sanjay Banerjee*, 5th ed., Upper Saddle River, N.J: Prentice Hall, 2000.
- [38] E. H. Rhoderick, "Metal-semiconductor contacts," *IEE Proceedings I - Solid-State and Electron Devices*, vol. 129, no. 1, pp. 1, 1982.
- [39] S. M. Sze, and K. K. Ng, *Physics of semiconductor devices*, New York: John Wiley & Sons, 2007.
- [40] S. Ha, P. Mieszkowski, M. Skowronski, and L. B. Rowland, "Dislocation conversion in 4H silicon carbide epitaxy," *J. Crystal Growth*, vol. 244, no. 3, pp. 257-266, 2002.
- [41] T. Ohno, H. Yamaguchi, S. Kuroda, K. Kojima, T. Suzuki, and K. Arai, "Influence of growth conditions on basal plane dislocation in 4H-SiC epitaxial layer," *J. Crystal Growth*, vol. 271, no. 1, pp. 1-7, 2004.
- [42] H. Song, and T. S. Sudarshan, "Basal plane dislocation conversion near the epilayer/substrate interface in epitaxial growth of 4° off-axis 4H-SiC," *J. Crystal Growth*, vol. 371, pp. 94-101, 2013.
- [43] H. Fujiwara, K. Danno, T. Kimoto, T. Tojo, and H. Matsunami, "Effects of C/Si ratio in fast epitaxial growth of 4H-SiC(0001) by vertical hot-wall chemical vapor deposition," *J. Crystal Growth*, vol. 281, no. 2, pp. 370-376, 2005.
- [44] Q. Wahab, A. Ellison, A. Henry, E. Janzén, C. Hallin, J. Di Persio, and R. Martinez, "Influence of epitaxial growth and substrate-induced defects on the breakdown of 4H-SiC Schottky diodes," *Appl. Phys. Lett.*, vol. 76, no. 19, pp. 2725-2727, 2000.

- [45] R. Yakimova, N. Vouroutzis, M. Syväjärvi, and J. Stoemenos, “Morphological features related to micropipe closing in 4H-SiC,” *J. Appl. Phys.*, vol. 98, no. 3, pp. 034905, 2005.
- [46] P. G. Neudeck, “Electrical impact of SiC structural crystal defects on high electric field devices,” *Mater. Sci. Forum*, vol. 338-342, pp. 1161-1166, 1999.
- [47] W. Kern, “The Evolution of Silicon Wafer Cleaning Technology,” *J. Electrochem. Soc.*, vol. 137, no. 6, pp. 1887-1892, 1990.
- [48] J. W. Kleppinger, S. K. Chaudhuri, O. Karadavut, and K. C. Mandal, “Defect characterization and charge transport measurements in high-resolution Ni/n-4H-SiC Schottky barrier radiation detectors fabricated on 250 μm epitaxial layers,” *J. Appl. Phys.*, vol. 129, no. 24, pp. 244501, 2021.
- [49] R. T. Tung, “Electron transport at metal-semiconductor interfaces: General theory,” *Phys. Rev. B*, vol. 45, no. 23, pp. 13509-13523, 1992.
- [50] K. V. Nguyen, M. A. Mannan, and K. C. Mandal, “Improved n-type 4H-SiC epitaxial radiation detectors by edge termination,” *IEEE Trans. Nucl. Sci.*, vol. 62, no. 6, pp. 3199 - 3206, 2015.
- [51] M. Jun, M. Jang, Y. Kim, C. Choi, T. Kim, S. Oh, and S. Lee, “Analysis of temperature-dependent barrier heights in erbium-silicided Schottky diodes,” *J. Vac. Sci. Technol. B*, vol. 26, no. 1, pp. 137-140, 2008.
- [52] R. T. Tung, “The physics and chemistry of the Schottky barrier height,” *Appl. Phys. Rev.*, vol. 1, pp. 011304, 2014.
- [53] H. Schroeder, “Poole-Frenkel-effect as dominating current mechanism in thin oxide films—An illusion?!” *J. Appl. Phys.*, vol. 117, no. 21, pp. 215103, 2015.
- [54] S. K. Chaudhuri, J. W. Kleppinger, and K. C. Mandal, “Radiation detection using fully depleted 50 μm thick Ni/n-4H-SiC epitaxial layer Schottky diodes with ultra-low concentration of Z 1 / 2 and E H 6 / 7 deep defects,” *J. Appl. Phys.*, vol. 128, no. 11, pp. 114501, 2020.
- [55] S. K. Chaudhuri, K. J. Zavalla, and K. C. Mandal, “Experimental determination of electron-hole pair creation energy in 4H-SiC epitaxial layer: An absolute calibration approach,” *Appl. Phys. Lett.*, vol. 102, no. 3, pp. 031109, 2013.
- [56] J. F. Ziegler, M. D. Ziegler, and J. P. Biersack, “SRIM - The stopping and range of ions in matter (2010),” vol. 268, pp. 1818-1823, 2010.
- [57] Z. He, “Review of the Shockley–Ramo theorem and its application in semiconductor gamma-ray detectors,” *Nucl. Instrum. Method Phys. Res. A*, vol. 463, no. 1-2, pp. 250-267, 2001.

- [58] G. Cavalleri, E. Gatti, G. Fabri, and V. Svelto, "Extension of Ramo's theorem as applied to induced charge in semiconductor detectors," *Nucl. Instrum. Methods*, vol. 92, no. 1, pp. 137-140, 1971.
- [59] W. Shockley, "Currents to conductors induced by a moving point charge," *J. Appl. Phys.*, vol. 9, no. 10, pp. 635-636, 1938.
- [60] S. Ramo, "Currents induced by electron motion," *Proc. IRE*, vol. 27, no. 9, pp. 584-585, 1939.
- [61] J. Erlekampf, M. Rommel, K. Rosshirt-Lilla, B. Kallinger, P. Berwian, J. Friedrich, and T. Erlbacher, "Lifetime limiting defects in 4H-SiC epitaxial layers: The influence of substrate originated defects," *J. Crystal Growth*, vol. 560-561, pp. 126033, 2021.
- [62] K. Hecht, "Zum Mechanismus des lichtelektrischen Primärstromes in isolierenden Kristallen," vol. 77, no. 3, pp. 235-245, 1932.
- [63] W. Shockley, and W. T. Read, "Statistics of the recombinations of holes and electrons," *Phys. Rev.*, vol. 87, no. 5, pp. 835-842, 1952.
- [64] R. N. Hall, "Electron-Hole Recombination in Germanium," *Phys. Rev.*, vol. 387, pp. 228, 1952.
- [65] P. A. M. Dirac, and R. H. Fowler, "On the theory of quantum mechanics," *Proc. Math. Phys. Eng.*, vol. 112, no. 762, pp. 661-677, 1926.
- [66] I. Capan, T. Brodar, Ž. Pastuović, R. Siegele, T. Ohshima, S.-i. Sato, T. Makino, L. Snoj, V. Radulović, J. Coutinho, V. J. B. Torres, and K. Demmouche, "Double negatively charged carbon vacancy at the h- and k-sites in 4H-SiC: Combined Laplace-DLTS and DFT study," *J. Appl. Phys.*, vol. 123, no. 16, pp. 161597, 2018.
- [67] N. T. Son, X. T. Trinh, L. S. Løvlie, B. G. Svensson, K. Kawahara, J. Suda, T. Kimoto, U. T., J. Isoya, T. Makino, T. Ohshima, and E. Janzén, "Negative-U system of carbon vacancy in 4H-SiC.," *Phys. Rev. Lett.*, vol. 109, no. 18, pp. 187603, 2012.
- [68] L. Storasta, H. Tsuchida, T. Miyazawa, and T. Ohshima, "Enhanced annealing of the Z1/2 defect in 4H-SiC epilayers.," *J. Appl. Phys.*, vol. 103, pp. 013705, 2008.
- [69] T. Kimoto, K. Danno, and J. Suda, "Lifetime-killing defects in 4H-SiC epilayers and lifetime control by low-energy electron irradiation," *phys. status solidi b*, vol. 245, no. 7, pp. 1327-1336, 2008.
- [70] G. Alfieri, and T. Kimoto, "Resolving the EH6/7 level in 4H-SiC by laplace-transform deep level transient spectroscopy," *Appl. Phys. Lett.*, vol. 102, pp. 152108, 2013.

- [71] J. Zhang, L. Storasta, P. J. Bergman, P. J. Son, and E. Janzén, “Electrically active defects in n-type 4H–silicon carbide grown in a vertical hot-wall reactor.,” *J. Appl. Phys.*, vol. 4708-4714, pp. 93, 2003.
- [72] S. B. Zhang, S. H. Wei, A. Zunger, and H. Katayama-Yoshida, “Defect physics of the CuInSe₂ chalcopyrite semiconductor,” *Phys. Rev. B*, vol. 57, no. 16, pp. 9642-9656, 1998.
- [73] D. Sholl, and J. A. Steckel, *Density functional theory: a practical introduction*: John Wiley & Sons, 2011.
- [74] W. Kohn, and L. J. Sham, “Self-Consistent Equations Including Exchange and Correlation Effects,” *Phys. Rev.*, vol. 140, no. 4A, pp. A1133-A1138, 1965.
- [75] P. E. Blöchl, “Projector augmented-wave method,” *Phys. Rev. B*, vol. 50, no. 24, pp. 17953-17979, 1994.
- [76] C. Freysoldt, J. Neugebauer, and C. G. Van de Walle, “Fully ab initio finite-size corrections for charged-defect supercell calculations,” *Phys. Rev. Lett.*, vol. 102, no. 1, pp. 016402, 2009.
- [77] M. J. Puska, S. Pöykkö, M. Pesola, and R. M. Nieminen, “Convergence of supercell calculations for point defects in semiconductors: Vacancy in silicon,” *Phys. Rev. B*, vol. 58, no. 3, pp. 1318-1325, 1998.
- [78] J. Heyd, G. E. Scuseria, and M. Ernzerhof, “Hybrid functionals based on a screened Coulomb potential,” *J. Chem. Phys.*, vol. 118, pp. 8207-8215, 2003
- [79] J. Heyd, G. E. Scuseria, and M. Ernzerhof, “Erratum: “Hybrid functionals based on a screened Coulomb potential” [J. Chem. Phys. 118, 8207 (2003)],” *J. Chem. Phys.*, vol. 124, no. 21, pp. 219906, 2006.
- [80] J. P. Perdew, M. Ernzerhof, and K. Burke, “Rationale for mixing exact exchange with density functional approximations,” *J. Chem. Phys.*, vol. 105, no. 22, pp. 9982-9985, 1996.
- [81] J. Paier, M. Marsman, K. Hummer, G. Kresse, I. C. Gerber, and J. G. Angyan, “Erratum: Screened hybrid density functionals applied to solids [J. Chem. Phys. 124, 154709 (2006)],” *J. Chem. Phys.*, vol. 125, pp. 249901-249902, 2006.
- [82] P. Deák, B. Aradi, T. Frauenheim, E. Janzén, and A. Gali, “Accurate defect levels obtained from the HSE06 range-separated hybrid functional,” *Phys. Rev. B*, vol. 81, no. 15, pp. 153203, 2010.
- [83] G. Alfieri, and T. Kimoto, “First-principles study of Cl diffusion in cubic SiC,” *J. Appl. Phys.*, vol. 113, no. 13, pp. 133706, 2013.

- [84] T. Kobayashi, K. Harada, Y. Kumagai, F. Oba, and Y.-i. Matsushita, "Native point defects and carbon clusters in 4H-SiC: A hybrid functional study," *J. Appl. Phys.*, vol. 125, no. 12, pp. 125701, 2019.
- [85] X. Wang, J. Zhao, Z. Xu, F. Djurabekova, M. Rommel, Y. Song, and F. Fang, "Density functional theory calculation of the properties of carbon vacancy defects in silicon carbide," *Nanotechnology and Precision Eng.*, vol. 3, pp. pp. 211-217, 2020.
- [86] Y. Kumagai, and F. Oba, "Electrostatics-based finite-size corrections for first-principles point defect calculations," *Phys. Rev. B*, vol. 89, no. 19, pp. 195205, 2014.
- [87] G. Alfieri, and T. Kimoto, "Theoretical study of Cl-related defect complexes in cubic SiC," *J. Appl. Phys.*, vol. 111, no. 10, pp. 103705, 2012.
- [88] L. Gordon, A. Janotti, and C. G. Van de Walle, "Defects as qubits in 3C- and 4H-SiC," *Phys. Rev. B*, vol. 92, pp. 045208, 2015.
- [89] K. Danno, and T. Kimoto, "Deep level transient spectroscopy on as-grown and electron-irradiated p-type 4H-SiC epilayers," *J. Appl. Phys.*, vol. 101, no. 10, pp. 103704, 2007.
- [90] K. Danno, and T. Kimoto, "High-Temperature Deep Level Transient Spectroscopy on As-Grown P-Type 4H-SiC Epilayers," *Jpn. J. Appl. Phys.*, vol. 45, no. No. 10, pp. L285-L287, 2006.
- [91] M. A. Mannan, S. K. Chaudhuri, K. V. Nguyen, and K. C. Mandal, "Effect of Z1/2, EH5, and Ci1 deep defects on the performance of n-type 4H-SiC epitaxial layers Schottky detectors: Alpha spectroscopy and deep level transient spectroscopy studies," *J. Appl. Phys.*, vol. 115, no. 22, pp. 224504, 2014.
- [92] K. C. Mandal, S. K. Chaudhuri, K. V. Nguyen, and M. A. Mannan, "Correlation of Deep Levels With Detector Performance in 4H-SiC Epitaxial Schottky Barrier Alpha Detectors," *IEEE Trans. Nucl. Sci.*, vol. 61, no. 4, pp. 2338-2344, 2014.
- [93] P. B. Klein, R. Myers-Ward, K. K. Lew, B. L. VanMil, C. R. Eddy, D. K. Gaskill, A. Shrivastava, and T. S. Sudarshan, "Recombination processes controlling the carrier lifetime in n-4H-SiC epilayers with low Z1/2 concentrations," *J. Appl. Phys.*, vol. 108, no. 3, pp. 033713, 2010.
- [94] B. J. Skromme, E. Luckowski, K. Moore, M. Bhatnagar, C. E. Weitzel, T. Gehoski, and D. Ganser, "Electrical characteristics of schottky barriers on 4H-SiC: The effects of barrier height nonuniformity," *J. Electron. Mater.*, vol. 29, no. 3, pp. 376-383, 2000.
- [95] J. W. Kleppinger, S. K. Chaudhuri, O. Karadavut, and K. C. Mandal, "Role of deep levels and barrier height lowering in current-flow mechanism in 150 μm

- thick epitaxial n-type 4H-SiC Schottky barrier radiation detectors,” *Appl. Phys. Lett.*, vol. 119, no. 6, pp. 063502, 2021.
- [96] F. Triendl, G. Pfusterschmied, G. Pobegen, J. P. Konrath, and U. Schmid, “Theoretical and experimental investigations of barrier height inhomogeneities in poly-Si/4H-SiC heterojunction diodes,” *Semicond. Sci. Technol.*, vol. 35, no. 11, pp. 115011, 2020.
- [97] M. B. H. Breese, “A theory of ion beam induced charge collection,” *J. Appl. Phys.*, vol. 74, no. 6, pp. 3789-3799, 1993.
- [98] D. V. Lang, “Deep-level transient spectroscopy: A new method to characterize traps in semiconductors,” *J. Appl. Phys.*, vol. 45, no. 7, pp. 3023-3032, 1974.
- [99] T. Dalibor, G. Pensl, N. Nordell, and A. Schöner, “Electrical properties of the titanium acceptor in silicon carbide,” *Phys. Rev. B*, vol. 55, no. 20, pp. 13618-13624, 1997.
- [100] E. Dobročka, and J. Osvald, “Influence of barrier height distribution on the parameters of Schottky diodes,” *Appl. Phys. Lett.*, vol. 65, no. 5, pp. 575-577, 1994.
- [101] S. I. Maximenko, J. A. Freitas, R. L. Myers-Ward, K. K. Lew, B. L. VanMil, C. R. Eddy, D. K. Gaskill, P. G. Muzykov, and T. S. Sudarshan, “Effect of threading screw and edge dislocations on transport properties of 4H-SiC homoepitaxial layers,” *J. Appl. Phys.*, vol. 108, no. 1, pp. 013708, 2010.
- [102] Y. Wang, G. N. Ali, M. K. Mikhov, V. Vaidyanathan, B. J. Skromme, B. Raghothamachar, and M. Dudley, “Correlation between morphological defects, electron beam-induced current imaging, and the electrical properties of 4H-SiC Schottky diodes,” *J. Appl. Phys.*, vol. 97, no. 1, pp. 013540, 2004.
- [103] R. F. Schmitsdorf, T. U. Kampen, and W. Mönch, “Explanation of the linear correlation between barrier heights and ideality factors of real metal-semiconductor contacts by laterally nonuniform Schottky barriers,” *J. Vac. Sci. Technol. B*, vol. 15, no. 4, pp. 1221-1226, 1997.
- [104] Q. Feng, Z. Feng, Z. Hu, X. Xing, G. Yan, J. Zhang, Y. Xu, X. Lian, and Y. Hao, “Temperature dependent electrical properties of pulse laser deposited Au/Ni/ β -(AlGa) $_2$ O $_3$ Schottky diode,” *Appl. Phys. Lett.*, vol. 112, no. 7, pp. 072103, 2018.
- [105] W. Li, K. Nomoto, D. Jena, and H. G. Xing, “Thermionic emission or tunneling? The universal transition electric field for ideal Schottky reverse leakage current: A case study in β -Ga $_2$ O $_3$,” *Appl. Phys. Lett.*, vol. 117, no. 22, pp. 222104, 2020.
- [106] R. T. Tung, “Formation of an electric dipole at metal-semiconductor interfaces,” *Phys. Rev. B*, vol. 64, no. 20, pp. 205310, 2001.

- [107] V. N. Brudnyi, and A. V. Kosobutsky, “Electronic properties of SiC polytypes: Charge neutrality level and interfacial barrier heights,” *Superlattices Microstruct.*, vol. 111, pp. 499-505, 2017.
- [108] D. Defives, O. Noblanc, C. Dua, C. Brylinski, M. Barthula, V. Aubry-Fortuna, and F. Meyer, “Barrier inhomogeneities and electrical characteristics of Ti/4H-SiC Schottky rectifiers,” *IEEE Trans. Electron Devices* vol. 46, no. 3, pp. 449-455, 1999.
- [109] G. Brezeanu, G. Pristavu, F. Draghici, M. Badila, and R. Pascu, “Characterization technique for inhomogeneous 4H-SiC Schottky contacts: A practical model for high temperature behavior,” *J. Appl. Phys.*, vol. 122, no. 8, pp. 084501, 2017.
- [110] J. R. Yeargan, and H. L. Taylor, “The Poole-Frenkel Effect with Compensation Present,” *J. Appl. Phys.*, vol. 39, no. 12, pp. 5600-5604, 1968.
- [111] P. G. Muzykov, R. M. Krishna, and K. C. Mandal, “Temperature dependence of current conduction in semi-insulating 4H-SiC epitaxial layer,” *Appl. Phys. Lett.*, vol. 100, no. 3, pp. 032101, 2012.
- [112] A. Castaldini, A. Cavallini, L. Rigutti, F. Nava, S. Ferrero, and F. Giorgis, “Deep levels by proton and electron irradiation in 4H-SiC,” *J. Appl. Phys.*, vol. 98, no. 5, pp. 053706, 2005.
- [113] A. Furrer, J. F. Mesot, and T. Strässle, *Neutron scattering in condensed matter physics*: World Scientific Publishing Company, 2009.
- [114] M. Rühl, C. Ott, S. Götzinger, M. Krieger, and H. B. Weber, “Controlled generation of intrinsic near-infrared color centers in 4H-SiC via proton irradiation and annealing,” *Appl. Phys. Lett.*, vol. 113, no. 12, pp. 122102, 2018.
- [115] G. Alfieri, L. Knoll, L. Kranz, and V. Sundaramoorthy, “The effects of illumination on deep levels observed in as-grown and low-energy electron irradiated high-purity semi-insulating 4H-SiC,” *J. Appl. Phys.*, vol. 123, no. 17, pp. 175304, 2018.
- [116] H. Li, C. Liu, Y. Zhang, C. Qi, Y. Wei, J. Zhou, T. Wang, G. Ma, Z. Wang, S. Dong, and M. Huo, “Irradiation effect of primary knock-on atoms on conductivity compensation in N-type 4H-SiC Schottky diode under various irradiations,” *Semicond. Sci. Technol.*, vol. 34, no. 9, pp. 095010, 2019.
- [117] T. Brodar, I. Capan, V. Radulović, L. Snoj, Ž. Pastuović, J. Coutinho, and T. Ohshima, “Laplace DLTS study of deep defects created in neutron-irradiated n-type 4H-SiC,” *Nucl. Instrum. Method Phys. Res. B*, vol. 437, pp. 27-31, 2018.
- [118] S. Popelka, P. Hazdra, R. Sharma, V. Záhlava, and J. Vobecký, “Effect of neutron irradiation on high voltage 4H-SiC vertical JFET characteristics: characterization and modeling,” *IEEE Trans. Nucl. Sci.*, vol. 61, no. 6, pp. 3030-3036, 2014.

- [119] I. Capan, T. Brodar, Y. Yamazaki, Y. Oki, T. Ohshima, Y. Chiba, Y. Hijikata, L. Snoj, and V. Radulović, “Influence of neutron radiation on majority and minority carrier traps in n-type 4H-SiC,” *Nucl. Instrum. Method Phys. Res. B*, vol. 478, pp. 224-228, 2020.
- [120] P. Hazdra, V. Záhlava, and J. Vobecký, “Point defects in 4H-SiC epilayers introduced by neutron irradiation,” *Nucl. Instrum. Method Phys. Res. B*, vol. 327, pp. 124-127, 2014.
- [121] S. Seshadri, A. R. Dulloo, F. H. Ruddy, J. G. Seidel, and L. B. Rowland, “Demonstration of an SiC neutron detector for high-radiation environments,” *IEEE Trans. Electron Devices*, vol. 46, no. 3, pp. 567-571, 1999.
- [122] H. K. Gersch, D. S. McGregor, and P. A. Simpson, “The effect of incremental gamma-ray doses and incremental neutron fluences upon the performance of self-biased 10B-coated high-purity epitaxial GaAs thermal neutron detectors,” *Nucl. Instrum. Method Phys. Res. A*, vol. 489, no. 1, pp. 85-98, 2002.
- [123] J. A. Borsuk, and R. M. Swanson, “Current transient spectroscopy: A high-sensitivity DLTS system,” *IEEE Transactions on Electron Devices*, vol. 27, no. 12, pp. 2217-2225, 1980.
- [124] M. Tapiero, N. Benjelloun, J. P. Zielinger, S. El Hamd, and C. Noguét, “Photoinduced current transient spectroscopy in high-resistivity bulk materials: Instrumentation and methodology,” *J. Appl. Phys.*, vol. 64, no. 8, pp. 4006-4012, 1988.
- [125] S. G. Sridhara, R. P. Devaty, and W. J. Choyke, “Absorption coefficient of 4H silicon carbide from 3900 to 3250 Å,” *J. Appl. Phys.*, vol. 84, no. 5, pp. 2963-2964, 1998.
- [126] M. E. Bathen, A. Galeckas, J. Müting, H. M. Ayedh, U. Grossner, J. Coutinho, Y. K. Frodason, and L. Vines, “Electrical charge state identification and control for the silicon vacancy in 4H-SiC,” *Npj Quantum Inf.*, vol. 5, no. 1, pp. 111, 2019.
- [127] F. Nava, A. Castaldini, A. Cavallini, P. Errani, and V. Cindro, “Radiation Detection Properties of 4H-SiC Schottky Diodes Irradiated Up to 10^{16} n/cm² by 1 MeV Neutrons,” *IEEE Trans. Nucl. Sci.*, vol. 53, no. 5, pp. 2977-2982, 2006.
- [128] K. Szász, V. Ivády, I. A. Abrikosov, E. Janzén, M. Bockstedte, and A. Gali, “Spin and photophysics of carbon-antisite vacancy defect in 4H silicon carbide: A potential quantum bit,” *Phys. Rev. B*, vol. 91, no. 12, pp. 121201, 2015.
- [129] R. Karsthof, M. E. Bathen, A. Galeckas, and L. Vines, “Conversion pathways of primary defects by annealing in proton-irradiated n-type 4H-SiC,” *Phys. Rev. B*, vol. 102, no. 18, pp. 184111, 2020.

- [130] G. Alfieri, and T. Kimoto, “Capacitance spectroscopy study of deep levels in Cl-implanted 4H-SiC,” *J. Appl. Phys.*, vol. 112, no. 6, pp. 063717, 2012.
- [131] D. A. Brown, M. B. Chadwick, R. Capote, A. C. Kahler, A. Trkov, M. W. Herman, A. A. Sonzogni, Y. Danon, A. D. Carlson, M. Dunn, D. L. Smith, G. M. Hale, G. Arbanas, R. Arcilla, C. R. Bates, B. Beck, B. Becker, F. Brown, R. J. Casperson, J. Conlin, D. E. Cullen, M. A. Descalle, R. Firestone, T. Gaines, K. H. Guber, A. I. Hawari, J. Holmes, T. D. Johnson, T. Kawano, B. C. Kiedrowski, A. J. Koning, S. Kopecky, L. Leal, J. P. Lestone, C. Lubitz, J. I. Márquez Damián, C. M. Mattoon, E. A. McCutchan, S. Mughabghab, P. Navratil, D. Neudecker, G. P. A. Nobre, G. Noguere, M. Paris, M. T. Pigni, A. J. Plompen, B. Pritychenko, V. G. Pronyaev, D. Roubtsov, D. Rochman, P. Romano, P. Schillebeeckx, S. Simakov, M. Sin, I. Sirakov, B. Sleaford, V. Sobes, E. S. Soukhovitskii, I. Stetcu, P. Talou, I. Thompson, S. van der Marck, L. Welsch-Sherrill, D. Wiarda, M. White, J. L. Wormald, R. Q. Wright, M. Zerkle, G. Žerovnik, and Y. Zhu, “ENDF/B-VIII.0: The 8th Major Release of the Nuclear Reaction Data Library with CIELO-project Cross Sections, New Standards and Thermal Scattering Data,” *Nucl. Data Sheets*, vol. 148, pp. 1-142, 2018.